Dielectric Spectroscopy Characteristics of New and Aged High Voltage Insulating Polymeric Materials

by

Anton V. Vykhodtsev

A thesis submitted to the Faculty of Graduate Studies of
The University of Manitoba
in partial fulfillment of the requirements for the degree of

MASTER OF SCIENCE

Department of Electrical and Computer Engineering
University of Manitoba
Winnipeg, Manitoba, Canada

December 2017

Abstract

Increased use of solid polymeric materials in the insulating structures of high voltage equipment for electric power systems over the past years has occurred despite a lack of understanding about how these materials age while in service. Therefore, studies of ageing are crucial for power system reliability and are important for both key participants of the electric power industry: utilities and consumers. The development of an accelerated ageing procedure that mimics the presence of the thermal gradient across the insulating structure is reported. A test module that applies a constant thermal gradient across a sample of insulation material has been designed, built, and tested. An additional study was conducted into evaluation protocols for ageing of polymeric materials used for outdoor applications based on the dielectric spectroscopy measurements [1]: certain refinements to this method are proposed. A comprehensive sensitivity analysis has been developed to estimate uncertainties of the measured dielectric parameters.

Acknowledgements

Foremost, I would like to express my deepest gratitude and appreciation to my supervisors, Drs. Derek Oliver and Behzad Kordi, for their tireless support, guidance throughout my research, and reviews of my writing. Without their persistent help and inspiration this dissertation would not have materialized. I wish to acknowledge financial assistance in the form of a Manitoba Graduate Scholarship (MGS) from the Minister of Education and Advanced Learning of Manitoba and the Faculty of Graduate Studies of the University of Manitoba. The research was supported by Manitoba Hydro funding (Project G294) and the Natural Sciences and Engineering Research Council (NSERC). Lastly, and most importantly, I would like to express my sincere appreciation to my parents and my brother for their love, support, and encouragement.

Table of Contents

List of Figures

List of Tables

Chapter 1

Introduction

1.1 Problem Description

Playing a key role in the reliability of high voltage (HV) equipment for power systems, conventional insulating materials such as ceramics and glass used for the manufacture of the overhead power line insulators or paper/oil used as an insulating layer in power cables are being gradually replaced by solid polymeric materials. The reason for this is unique physical and chemical properties of polymers. However, the physical properties and, by extension, the insulating and dielectric character of solid polymeric materials are more susceptible to ageing due to electrical, thermal, mechanical, and environmental stresses during their operational lifetime [2]. This irreversible process leads to the deterioration of dielectric/insulating properties and results in degraded performance, and even a fatal electrical breakdown driven by the thermal or partial discharge mechanisms. Therefore, the studies of ageing are equally important for power utilities and consumers since this knowledge will allow to prevent the power outage and a damage of expensive power system equipment by replacing critically aged components in a timely manner.

The operational integrity of the power system component will be lost if a sample is

directly extracted from its insulating structure [3]. Thus, the development of new testing methodologies to predict long-term performance [4, 5] based on the results of accelerated ageing of samples [6, 7] or samples obtained from the insulating structures that have been withdrawn from service [8] have attracted increasing interest. One technique to monitor the degradation within the insulation is based on the frequency response of the complex dielectric permittivity ($\varepsilon = \varepsilon' - j\varepsilon''$) [9,10]. Dielectric spectroscopy, the frequency response of ε, serves to bind measured electrical response and associated polarization processes with the structure and the morphology of the material under investigation [11,12]. Hence, differences between the dielectric spectra of unaged and aged materials may indicate the commencement and subsequent development of degradation [13, 14].

Until now an accepted procedure/standard to assess physical properties and the operational lifetime of insulating polymeric materials based on the dielectric spectroscopy measurements did not exist. The development of such routine protocol has commenced recently under the auspices of *CIGRÉ* [15]. The outcome of this work will be the creation of the standardized protocol that will be used to facilitate the development of new materials or to evaluate ageing characteristics of existing polymeric materials for outdoor applications. The present work is a part of the international collaboration to develop a testing method for the dielectric response characterization of polymeric insulating materials for outdoor applications. Together with other participants in the *CIGRÉ Working Group D1.59*, we have contributed to the development and performed evaluation of the testing protocol by the completion two cycles of round-robin tests on samples of polymer materials (unaged and after the complex water immersion procedure) and the conduction of sensitivity analysis.

Another important problem associated with the ageing of polymeric insulating materials is the development of an accelerated ageing procedure that mimics mechanisms that occur naturally when the insulating structure is aged in service rather than employing additional stress factors such as elevated temperatures or voltages. The latter can result in degradation

processes that are not expected during normal operating conditions [16]. Thermal accelerated ageing protocols are traditionally used to assess a long-term performance of polymeric insulating materials that face the thermal stresses in their service [6]. This standard defines the duration of an accelerated ageing and corresponding elevated temperature depending on the class of the polymeric material. The ageing takes place in an oven at the selected constant temperature. Thus, a uniform temperature distribution is generated across the sample. At the same time, many HV insulating structures experience the the presence of thermal gradients that exist, for example, across a transformer bushing surrounding by cold ambient temperatures or radially across the insulation of underground cables buried in the vicinity of the frost line. Therefore, the thermal ageing in the presence of thermal gradient requires the careful consideration and there is a need for the development of the testing procedure that takes into account this specific and identifiable factor.

1.2 Objectives

There are two main objectives in this thesis. First, it is to facilitate the development of the testing methodology to evaluate physical and long-term properties of solid polymeric materials utilizing the dielectric spectroscopy measurements and to solve arising problems. This will include the design of the test set-up at the University of Manitoba, the conduction of the required experiments, data analysis based on the dielectric spectroscopy theory and an evaluation of a test methodology proposed by [15]. A comprehensive sensitivity analysis has been developed to accurately calculate uncertainties of measured parameters.

The second direction of this thesis is to design, build, and test a module that generates a constant thermal gradient across a sample of insulation material. The comparison of ageing in this environment with the ageing of the same type of material in a uniform temperature environment will be performed and analyzed.

1.3 Contributions

The contributions of this thesis are presented as follows:

- Design of the experimental set-up to conduct measurements of the complex dielectric permittivity.
- Dielectric spectroscopy characterization (with the analysis) of six types of HV insulating polymeric materials.
- Development of a methodology to precisely compensate the edge effect on the measured capacitance utilizing finite element method.
- Completion of a sensitivity analysis to examine uncertainties associated with the measured complex dielectric permittivity.
- Design and implementation of the thermal gradient ageing module to study thermal ageing in the presence of temperature gradient within the insulating material.

1.4 Thesis Outline

This thesis is divided into six chapters as described below:

Chapter 1: Introduction of the thesis, giving the problem description, objectives, and contributions.

Chapter 2: Discussion on types of solid polymeric materials, natural and accelerating ageing, dielectric spectroscopy to analyse ageing, followed by a background on the complex dielectric permittivity and a literature review on the measuring apparatuses.

Chapter 3: The theory of contact-free method to measure the complex dielectric permittivity, two realizations of the electrical measurements and problems encountered during testing are presented. The method and its realization to compensate for the edge effect is discussed at the end of the chapter.

Chapter 4: Discussion on the material under the investigation. Details on all experimental protocols are provided.

Chapter 5: Discussion on results of various case studies implemented in this thesis. Chapter five is subdivided into: the influence of the sample arrangement within the testing cell, water immersion ageing, thermal gradient ageing, and sensitivity analysis.

Chapter 6: Conclusion of this thesis, with a discussion on future work.

Chapter 2

Background theory

2.1 HV Insulation Materials

The development of electric power systems was accompanied by the evolution of their most essential component, electrical insulation. Till the beginning of the twentieth century, insulation materials such as asphalt, rubber, mica, porcelain, glass, and cotton thread/fabric were made from natural materials [17]. Demand for higher resistivity and better electric withstand capability materials stimulated the search for new materials that resulted in the development of synthetic insulating materials [18]. Nowadays, most natural substances have been replaced by a vast number of their synthetic equivalents for use in high voltage insulation applications.

A variety of electrical insulating materials are used in the electrical power engineering. According to their area of application, materials for HV insulation may be divided in four broad groups (Table 2.1): moulding, jacketing, filling, and providing insulating mechanical support. Possessing high mechanical strength, moulding materials form mechanically rigid frame of insulation. They are usually used in combination with jacketing (housing) materials which protect them from the environmental stress. Among the insulating materials with a

Table 2.1. *Areas of application for solid HV insulating material [19].*

Type of material	Application	Examples of HV apparatus	Material
Moulding	Mechanically rigid forms of insulation	Insulators, bushings	Ceramics, glass, fiberglass, reinforced plastics, and epoxy resins
Jacketing	Provide extruded insulating jackets to conductors and insulators	Power cables, capacitors, transformers, electrical machines	Polyethylene, polyvinylchloride, natural and synthetic rubber, paper
Filling	Impregnate paper	Power cables, transformers, capacitors	Wax
Insulating mechanical support	Provide insulating supports	Transformers	Ebonite, bakelite, acrylic resin plates

natural origin, paper is still widely used in the manufacture of power cables, transformers, and capacitors. It is generally impregnated with filling materials such as oil or wax to improve its dielectric character. Materials which provide both insulation and mechanical support are required in transformers and switchgears.

Solid insulating materials are classified based on their chemical composition into four main categories: inorganic, organic and hybrid polymers, and composites (Table 2.2).

Ceramics, porcelain and glassy materials are inorganic materials that have, historically, been widely used as insulators [19]. However, they have recently fallen from favour due to their relatively poor resistance to surface pollution and high density (*i.e.* larger mass) compared to other materials such as composite polymer materials [5].

Solid polymers are long, chain structured molecules where repeated segments are linked by covalent bonds [19]. The process to produce polymeric material from small molecules (monomers) is called polymerization and can be carried out in a variety of ways [20]. The longest chain, backbone, of organic polymers consists of carbon atoms sometimes substituted by oxygen or nitrogen. Polymeric materials can be categorized by their response to heat

Table 2.2. *Classification of solid HV insulating material based on their composition [19].*

Type	Advantages	Disadvantages	Material
Inorganic	1. Ability to withstand high temperatures 2. Highly chemical resistant 3. High mechanical strength	1. Difficult to machine or process. 2. High density 3. Brittleness 4. Under polluted conditions, the hydrophilic surface of porcelain does not perform well.	Ceramics, glass, mica, asbestos
Polymeric organic/inorganic	1. Low density 2. Hydrophobic 3. Compactness	1. Some polymeric materials do not have long-term proven service-life. 2.Under the certain condition, aging can be a serious problem.	Paper, wood, wax, leather, natural and synthetic resins
Composite	Combined enhanced physical properties of a filler and a matrix.	Long-term service life is unproven.	Quartz, fiber and mica with synthetic resins, impregnated paper

(thermoplastic or thermoset) or to external deformation (elastomer). For example, rubber is an elastomer type polymer that has the ability to revert to its original shape after being deformed. Polymeric materials have low densities, the typical weight of an insulator made from a polymeric material is about 10% of the equivalent insulator made from porcelain or glass [5]. Hence, the use of polymers in HV engineering apparatuses reduces transportation and installation costs, and expenditures on supporting structures (*e.g.* towers). The higher dielectric withstand capability of polymeric materials permits more compact designs of power system equipment. The hydrophobic (water-repellent) properties of polymers prevent the development of continuous conductive contamination. However, the huge drawback of polymeric materials is the absence of the proven long-term service life associated with glass

and porcelain.

The application of interfaces at the micro/nanoscale in the polymer matrix is used to design new insulating materials with enhanced thermal, mechanical and electrical properties [21]. Typical composites of organic (polymer matrix) and inorganic materials (filler) are fiberglass reinforced plastics and quartz with epoxy resins. A long-term performance of composite materials is affected by the presence of interfaces and not fully quantified [16] as in the case of pure polymeric materials.

2.2 Natural and Accelerated Ageing

Leading to a gradual deterioration of dielectric properties, destructive processes inside the solid polymeric insulation or on its surface are caused by by electrical, thermal, mechanical stresses and environmental impact. The process of degradation is called ageing of the insulation [2]. These changes are usually irreversible and end with breakdown and failure of the insulating structure.

The operational life of any insulating structure can be described using the idealized timeline (Figure 2.1) and is divided into three major stages: ageing, degradation, and breakdown [4]. There is no clear demarcation between these stages and they overlap each other. Nonetheless, certain transformations associated with each stage may be identified. Breakdown, for instance, is an instant and catastrophic event leading to the loss of the main duty of insulation to withstand a certain level of voltage. A sample of solid insulating material cannot recover after a breakdown, this is the end of its operating life. The footprint of breakdown that bridges a HV electrode to the grounding electrode is comparable with the dimensions of the insulating structure and can be easily detected by an unaided eye. Degradation, on the other hand, is a longer process that facilitates the development of the conditions for the electrical breakdown by means of partial discharges, electrical trees, and water trees. These phenomena manifest in the “weak” parts of insulation and usually

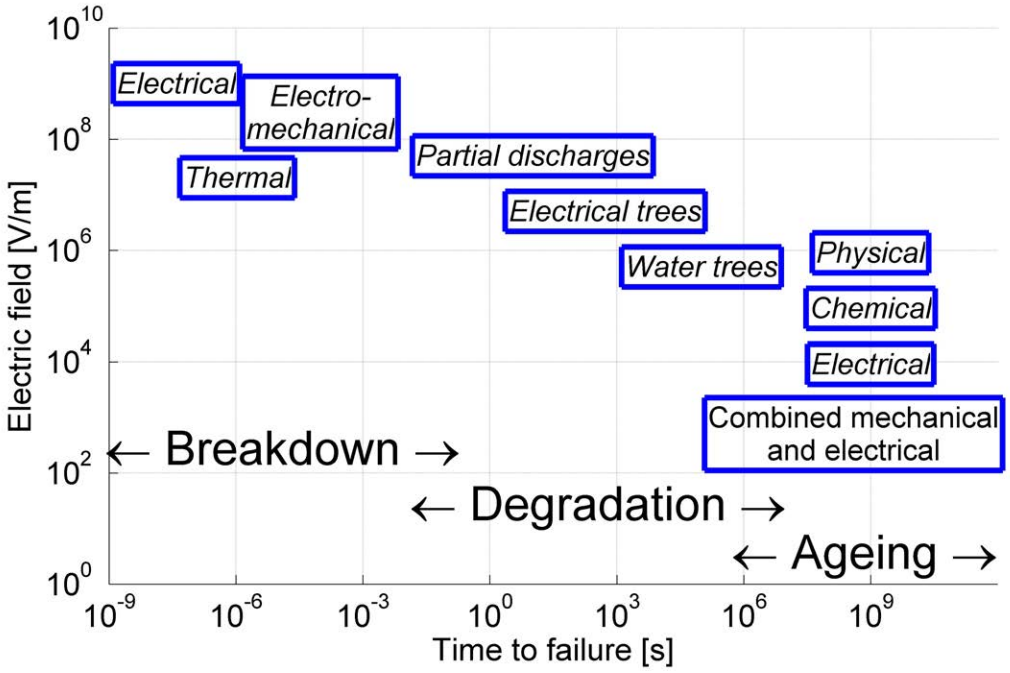

Figure 2.1. *Indicative times and electric fields over which various electrical breakdown and degradation mechanisms are active [4].*

form large fractal structures (electrical and water trees) which can be tracked by a microscopic technique. The trigger for degradation mechanism is an ageing that accompanies a polymeric insulating material during all its service life and occurs at molecular scale.

Mechanisms of ageing in polymeric insulating media can be divided into physical ageing, chemical ageing, electrical ageing, and combined mechanical and electrical degradation [2]. Physical ageing does not imply a change in chemical structure [22] and is linked with the concept of slow and gradual transformations to the equilibrium (structural relaxation) since the amorphous materials (all polymeric materials) are not in the thermodynamic equilibrium at temperatures below their glass transition [23]. Chemical ageing involves a change in the chemical structure of the polymer, generally via the formation of polymer free

radicals triggered by an initiating disturbance [2]. Free radicals are very reactive and lead to depolymerization or cross-linking network formations. The initiating disturbance for the chemical ageing is , for example, a thermal stress in the power cables [2] or the environmental factors such as moisture, ultraviolet light, acid rains, and ozone from the corona discharge in case of a polymeric cover of an insulator [24]. Caused by applied electric field, electrical ageing of an insulation is an intrinsic phenomenon of all power system components in service. It is considered that physical and chemical ageing processes are intensified by the electrical ageing [4]. Electrical ageing is revealed by the appearance of the partial discharges that take place in the gaseous media of nanoscopic/microscopic voids after the electric field reaches a threshold value. Combined mechanical and electrical degradation arises when an insulating structure under service conditions experiences the deformations leading to the formation of nanocracks, e.g. due to the force between two current carrying conductors. To generalize all ageing mechanisms occurring within the considered insulation under the operational conditions, the term 'natural ageing' is applied. An assessment of natural ageing based on the long-term observations are rarely performed since this method is hardly employed on a timescale that is compatible with economical and technological requirements.

An accelerated ageing is performed in such conditions in order to make the change of the properties faster than in natural ageing so that the long-term performance can be obtained within acceptable timescale. The purpose of accelerated ageing test is to establish the life cycle of an insulating structure exposed to high stress and then to extrapolate the results to typical operating conditions. Here, an accelerating ageing is a simplified model of natural ageing which imitates its main features and is capable of predicting behavior in real operating conditions. When designing an accelerating ageing test, a compromise between being the real representation of natural conditions and the duration of the test, must be carefully reached.

In this work, two mechanisms of accelerated ageing are studied: one associated with the

uptake of water via a range of diffusion mechanisms attributed to the outdoor HV insulators and the second focused on the ageing of a power cable insulation in the presence of thermal gradient.

2.3 Monitoring of Ageing

A wide variety of diagnostic techniques have been developed to detect various footprints of ageing in HV components. All the methods can be categorized into two major groups: destructive and non-destructive [25]. In a destructive technique, the sample or insulating structure will lose its main function to separate electrical conductors as a result of a test. For instance, AC and impulse breakdown tests are destructive methods which are used to quantify ability of a sample or insulating structure to operate without failures during rated electrical conditions (withstand tests) [26, 27]. In contrast, non-destructive diagnostic testing should not introduce additional degradation of the insulation and, after the test, the sample can be returned to operational use. These tests are desirable for monitoring and assessing the remaining working life of the material. Among non-destructive techniques, measurement of the partial discharge characteristics is widely applied [28]: high partial discharge activity is associated with the presence of microvoids and cracks in the insulating structure. Some methods have non-destructive nature but they require a sample to be extracted from the insulation structure diminishing its operational integrity. An example of this is the study of water and electrical treeing employing optical microscopy, which has been used to correlate the length of water trees and the voltage level of breakdown [29]. Ageing is also associated with formation of trap sites inside of insulating material which can be diagnosed by space charge measurement technique [30]. Environmental ageing mostly occurs on the surface of the insulating component, resulting in a loss of the hydrophobicity at the insulating surface. This is due to the structural and chemical modification of the surface indicated by the appearance of cracking and erosion sites. The degree of surface

degradation is usually examined by means of scanning electron microscopy [31].

Changes to the dielectric properties of the insulation (dielectric response) can be described using dielectric permittivity/loss tangent measurements. Historically, these were only carried out at the power frequency for which the HV system is designed. In his review of dielectric spectroscopy, Zaengl [11] highlighted that ageing effects manifest in quite different and specific frequency ranges and one-frequency measurements are sometimes ineffective to track even strong changes in the dielectric properties of complex system. In contrast, the measurement of dielectric response performed over a large frequency range enables the extraction of various ageing markers. In particular, this technique finds wide application in the monitoring of insulation of power cables. Liu *et al.* [13] obtained the difference in the dielectric response of a new and aged cable insulation as a function of temperature before and after ageing that provided insight into the commencement and development of degradation.

2.4 Electric Field and Material Interaction

Any kind of matter consists, on the atomic level, of positive and negative charges balancing each other microscopically or macroscopically. When the real HV insulating materials (as a particular example of dielectric) are exposed to an electric field **E**, three main processes are observed: polarization, electrical conductivity, and dielectric losses. Polarization is a distinctive feature of dielectrics and is associated with the slight shift of the unlike charges (induced electric dipole) or with the rotation of polar molecules (permanent electric dipole) in the presence of external electric field [32]. On the other hand, a small number of charged particles in real dielectrics can move the long distances in the electric field and discharge upon reaching the electrodes. This phenomenon is known as a direct current (DC) electrical conductivity. Dielectric losses represent the energy spent in the dielectric either on the charge separation or on the alignment of dipole with the electric field.

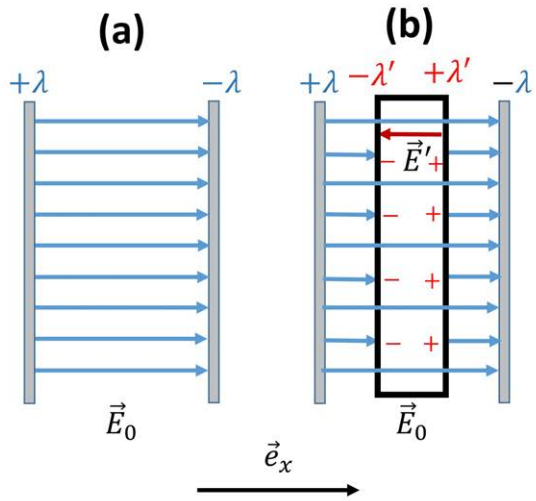

Figure 2.2. *Electric field in a parallel plate capacitor with the vacuum between the plates (a) or the dielectric between the plates (b).*

Polarization is usually studied at a macroscopic level. Here, individual dipoles are considered as a group. The macroscopic polarization **P** is defined as the number of polarized species per unit volume of the material. Being the response of a dielectric medium to the applied electric field, **P** does not have the universal relation with **E** for all materials. However, the polarization **P** of most dielectric materials (at least those used in HV engineering) is a linear function of the electric field in dielectric:

$$\mathbf{P} = \varepsilon_0 \chi \mathbf{E}, \tag{2.1}$$

where ε_0 is the permittivity of free space and has a value $8.85 \cdot 10^{-12}$ F/m and χ is the electric susceptibility of the dielectric material. The latter is a dimensionless quantity that defines the degree of polarization of a dielectric in response to an applied electric field.

To study the effect of an applied electric field on a dielectric material, consider an ideal air-filled parallel plate capacitor carries a fixed amount of equal but opposite charge (free charge) on its plates (Figure 2.2 a). The surface charge density on the plates is λ. According

to Gauss' law, an electric field between plates is uniform and equal to $\mathbf{E_0} = (\lambda/\varepsilon_0)\mathbf{e_x}$. When a dielectric slab is placed inside the capacitor (Figure 2.2 b), the bound charge with surface density λ' is induced on the surface of dielectric generating electric field $\mathbf{E'} = (\lambda'/\varepsilon_0)\mathbf{e_x}$. This field has an opposite direction compared to the electric field $\mathbf{E_0}$ and is defined by:

$$\mathbf{E} = \mathbf{E_0} - \mathbf{E'} = \mathbf{E_0} - \frac{\lambda'}{\varepsilon_0}\mathbf{e_x}. \tag{2.2}$$

Using definition of the polarization $\mathbf{P}$, it can be shown that $\mathbf{P} = \lambda'\mathbf{e_x}$. Thus, we can modify (2.2) and derive the expression for the resultant electric field inside of the dielectric employing the substitution from (2.1):

$$\mathbf{E} = \frac{\mathbf{E_0}}{1+\chi} = \frac{\mathbf{E_0}}{\varepsilon}, \tag{2.3}$$

where $\varepsilon = 1 + \chi$ is the dielectric permittivity of dielectric material. This quantity characterizes the ability of dielectric to polarize in an electric field and indicates how much it attenuates in dielectric. While the dielectric permittivity ε can be a tensor or a function of the position within the dielectric, usually it is assumed to take a constant value and be independent from the position in a HV insulation material. To avoid the need in bound charges in the description of the electric field in a dielectric, the electric displacement field $\mathbf{D}$ is used to define electric field in a dielectric in terms of free charges only and defined as

$$\mathbf{D} = \varepsilon_0\varepsilon\mathbf{E} = \varepsilon_0\mathbf{E} + \mathbf{P} = \varepsilon_0(1+\chi)\mathbf{E}. \tag{2.4}$$

2.5 Theory of Dielectric Spectroscopy in Time and Frequency Domains

Polarization processes cannot occur instantly in a dielectric material ($\chi > 0$). The linear dependence of $\mathbf{P}$ and $\mathbf{E}$ (2.1) does not illustrate the delayed response of $\mathbf{P}$ to changes in $\mathbf{E}$. Thus, dielectric properties are dynamic quantities that can be studied in the time as well as in the frequency domain [11]. This dynamic responses of dielectric media are illustrated by introducing a time-varying electric field $\mathbf{E}(t)$ (produced by $V(t)$ applied to the plates in Figure 2.2 a. Here, the electric displacement field $\mathbf{D}(t) = \varepsilon_0\mathbf{E}(t)$ will follow $\mathbf{E}(t)$ without delay.

Replacing the vacuum with an isotropic dielectric, the electric displacement field increases (2.4), but it lags the applied electrical field $E(t)$ as further polarization mechanisms are characterized by their response rate to the appearance of $\mathbf{E}$. The delay may be taken into account by the presence of a time dependence in the electric susceptibility $\chi = \chi(t)$ in (2.1). For simplicity, the exciting electric field $\mathbf{E}(t)$ is described using a step function $H(t)$ that is $\mathbf{E}(t) = \mathbf{E}_0 H(t - t_0)$. The polarization, together with the time-varying electric susceptibility and applied electric field, are depicted in Figure 2.3. The susceptibility and polarization, $\chi(t)$ and $\mathbf{P}(t)$, are interpreted as the step response functions of the dielectric medium. The initial part of $\chi(t)$ and $P(t)$ close to t_0 is shown as an ideal step to introduce an instantaneous polarization $\mathbf{P}_\infty = P(t = t_0)$. If sufficient time is allowed, then the observed polarization will reach a finite value and become static, $\mathbf{P}_s = \mathbf{P}(t \to \infty)$. If we introduce some monotonically increasing from 0 to 1 function $g(t)$, then the polarization at given time, t, is defined by

$$\mathbf{P}(t) = \mathbf{P}_\infty + (\mathbf{P}_s - \mathbf{P}_\infty)g(t - t_0). \tag{2.5}$$

The macroscopic polarization $\mathbf{P}(t)$ (2.5) can also be related to the applied electric field

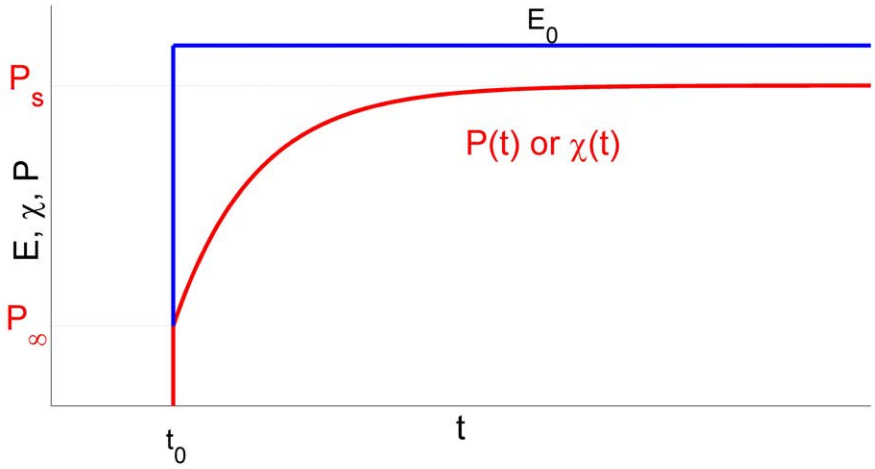

Figure 2.3. *Polarization of the dielectric medium excited by a step-like electric field.*

using the dielectric susceptibility:

$$\mathbf{P}(t) = \varepsilon_0[\chi_\infty + (\chi_s - \chi_\infty)g(t - t_0)]\mathbf{E}_0. \tag{2.6}$$

The substitution of dielectric permittivity $\varepsilon = 1 + \chi$ into (2.6) yields

$$\mathbf{P}(t) = \varepsilon_0[\varepsilon_\infty - 1 + (\varepsilon_s - \varepsilon_\infty)g(t - t_0)]\mathbf{E}_0. \tag{2.7}$$

In such formulation, $g(t)$ may be treated as a step response function in such formulation. Thus, for any arbitrary external electric field $E(t)$, the time-dependent polarization can be calculated using a convolution in the time domain:

$$\mathbf{P}(t) = \varepsilon_0\chi_\infty\mathbf{E}(t) + \varepsilon_0\int_{-\infty}^{t} f(t - \tau)\mathbf{E}(\tau)d\tau, \tag{2.8}$$

where $f(t)$ is dielectric response function given by:

$$f(t) = (\chi_s - \chi_\infty)\frac{dg(t)}{dt} = (\varepsilon_s - \varepsilon_\infty)\frac{dg(t)}{dt} \tag{2.9}$$

The dielectric response function may be used to characterize the response of a dielectric sample to a given electric excitation. Unfortunately, it cannot be measured directly. From Maxwell's equations, total current through the real dielectric exposed to a time-depended electric field $\mathbf{E}(t)$ consists of the conductivity current (σ_0 is the pure DC conductivity of the material) and two types of the displacement current (polarization and vacuum):

$$\begin{aligned}
\mathbf{J}(t) &= \sigma_0\mathbf{E}(t) + \frac{\partial \mathbf{D}(t)}{\partial t} \\
&= \sigma_0\mathbf{E}(t) + \varepsilon_0\frac{\partial \mathbf{E}(t)}{\partial t} + \frac{\partial \mathbf{P}(t)}{\partial t} \\
&= \sigma_0\mathbf{E}(t) + \varepsilon_0(1+\chi_\infty)\frac{\partial \mathbf{E}(t)}{\partial t} + \varepsilon_0\frac{d}{dt}\int_{-\infty}^{t} f(t-\tau)\mathbf{E}(\tau)d\tau \\
&= \sigma_0\mathbf{E}(t) + \varepsilon_0(1+\chi_\infty)\frac{\partial \mathbf{E}(t)}{\partial t} + \varepsilon_0 f(0)\mathbf{E}(t) + \varepsilon_0\int_{-\infty}^{t}\frac{df(t-\tau)}{dt}\mathbf{E}(\tau)d\tau.
\end{aligned} \tag{2.10}$$

The basic concept of dielectric characterization in the time domain (2.10) is an attribute of the polarization $P(t)$, and a dielectric response function may be obtained by measuring the polarization or depolarization (the time-domain measuring technique). Dynamic events may be also studied in frequency domain. The polymeric insulating materials investigated in this study are analyzed in the frequency domain. The concept of dielectric response in the frequency domain is directly derived from the corresponding equations of the the time domain where the description of a dielectric response is more evident.

The mathematical apparatus to determine a dielectric response in the frequency domain uses the Fourier Transformation of (2.10) [33]. Assuming a harmonic form of the applied electric field ($\mathbf{E}(t) = \mathrm{Re}(\dot{\mathbf{E}}e^{(-j\omega t)})$) and the absence of contributions from "high frequencies" ($\chi_\infty = 0$ and $f(0) = 0$), the current density in the frequency domain is determined by:

$$\dot{\mathbf{J}} = \dot{\mathbf{E}}[\sigma_0 + j\omega\varepsilon_0(1 + \dot{F})] \tag{2.11}$$

where $\dot{\mathbf{J}}$, $\dot{\mathbf{E}}$, and $\dot{F}$ are the Fourier transforms of the time-dependent current density through the dielectric sample, driving electric field and a dielectric response function. Comparing (2.4) and (2.11) the frequency-dependent susceptibility is

$$\chi(j\omega) = F(j\omega) = \chi'(\omega) - j\chi''(\omega) = \int_0^\infty f(t)e^{(-j\omega t)}d\tau. \tag{2.12}$$

Substituting (2.12) into (2.11), we obtain:

$$\dot{\mathbf{J}} = \dot{\mathbf{E}}[\sigma_0 + \varepsilon_0\omega\chi''(\omega) + j\omega\varepsilon_0(1 + \chi'(\omega)] \tag{2.13}$$

The sense of the real and imaginary parts of the complex electric susceptibility is interpreted using (2.13). The real part of the complex susceptibility contributes to the component of the total current which is in quadrature with the applied alternating electric field: no electrical power is consumed. On the other hand, the imaginary part gives an increase of the component of the total current which is in phase with the applied field: the contribution to the power loss. Moreover, (2.13) points out the experimental procedure to determine complex electric susceptibility by means of the measuring $\dot{\mathbf{J}}$ and $\dot{\mathbf{E}}$, *i.e.* measuring a current-voltage response as utilized in this work.

Similarly, the complex dielectric permittivity [1] may be defined by the Fourier Transform of the time-dependent electric displacement field as

$$\varepsilon(j\omega) = \varepsilon'(\omega) - j\varepsilon''(\omega) = 1 + \chi'(\omega) - j\chi''(\omega). \tag{2.14}$$

[1] In this work the complex dielectric permittivity corresponds to the ratio of the absolute permittivity of the medium and the permittivity of free space. The term relative in the complex dielectric permittivity is omitted for brevity.

The frequency domain response of dielectric media may be characterized using the dielectric dissipation factor (loss tangent):

$$\tan\delta = \frac{\varepsilon''}{\varepsilon'}. \tag{2.15}$$

Usually, it is impossible to distinguish the contribution to the power loss from the dielectric losses and the pure DC conductivity. For this purpose, another definition of the loss tangent is sometimes employed [11]:

$$\tan\delta = \frac{\varepsilon'' + \frac{\sigma_0}{\varepsilon_0\omega}}{\varepsilon'}. \tag{2.16}$$

The quantities, $\varepsilon(\omega)$, $\tan\delta$, and $\chi(\omega)$, will be used to examine changes resulting from accelerated ageing. The dispersion behavior of these quantities depends on the mechanism of polarization on the microscopic or macroscopic levels.

2.6 Mechanisms of Polarization

Dielectric polarization may be divided into elastic (resonance) and relaxation (thermal) polarizations. This division is based on the type of the interaction between charged particles contributing to the polarization: elastically (strongly) bound and weakly-bound. Each polarization mechanism is associated with its characteristic frequency or characteristic time of the process in the frequency and time domain.

Elastically bound particles thermally oscillate about an equilibrium position. When exposed to an electric field, these particles are slightly shifted from this position. There are three main types of elastic polarization processes [32]:

- "Electronic polarization" is inherent to all dielectric matter. The applied electric field displaces the cloud of electrons around the atomic nuclei in opposition to the electric

field direction. This is a fast response and it is associated with the formation of polarization at optical frequencies ($\sim 10^{14}$-10^{15} Hz).

- "Atomic polarization" occurs in molecules when component atoms shift in response to the driving field. Chemical bonds between atoms in molecules of non-metallic solids maybe covalent and ionic that correspond to partial and complete charge transfer between atoms respectively. In both cases, some atoms in a molecule appear to be more positively charged whilst others are more negatively charged relatively to their states as an isolated atom. When this molecule is placed in an electric field its atoms will move from each other inducing an electric dipole moment. In contrast with light electrons, heavy nucleus can contribute to the polarization to infra-red ($\sim 10^{11}$-10^{14} Hz).

- "Ionic polarization" is a particular case of atomic polarization. It refers to the relocation of the positive and negative ions (ionic bonds) from the equilibrium state in the molecule in the presence of a driving electric field. It typically persists at frequencies till $\sim 10^{9}$-10^{13} Hz

In contrast, weakly-bound particles in the absence of an electric field have several equilibrium positions which they can occupy with a certain probability. A transition from one equilibrium position to another is thermally assisted. Relaxation polarization is linked with the appearance of new equilibrium positions in the presence of an electric field. Similar to the elastic polarization, relaxation polarization divides into several groups:

- "Dipolar (orientational) polarization" pertains to dielectrics where relaxing particles are polar molecules. Having permanent electric dipole, they are partially aligned under the influence of external electric field. Dipolar polarization is effective up to MHz and GHz ranges.

- "Interfacial (Maxwell-Wagner) polarization" is related to the formation of dipoles due to the appearance of negative and positive charges at an interface between two materials (macro-interface) or between two regions (micro-interface) within a material. Interfacial polarization is manifested at frequencies below 10 Hz.

- "Space charge polarization" refers to the accumulation of charges within the dielectric. Moving/hopping in the presence of an electric field mobile charge carriers can be trapped by the localized site of defects (nanoscopic/microscopic voids and impurities). In this case, positive space charge settles down near the cathode region whilst negative space charge is distributed in the vicinity of the anode. Macroscopically shifted charges form polarization that has large characteristic time. This phenomenon is active below 10 Hz.

In general, the response of a particular dielectric sample will include several polarization mechanisms coexisting and not significantly interacting between themselves, thus, the permittivity can be expressed as the sum of the contributions of the individual mechanisms [34]:

$$\varepsilon(\omega) = \varepsilon'(\omega) - j\varepsilon''(\omega) = 1 + \sum_i \chi_i'(\omega) - j \sum_i \chi_i''(\omega), \tag{2.17}$$

where the pair, χ_i' and χ_i'', corresponds to the separate polarization mechanism.

Figure 2.4 shows both the real and imaginary parts of a complex permittivity spectrum of dielectric containing different polarization mechanism. The low-frequency part of the spectrum corresponds to the static dielectric permittivity. At higher frequencies (X-ray) there is no polarizing effect in the material and dielectric permittivity is the same as in vacuum.

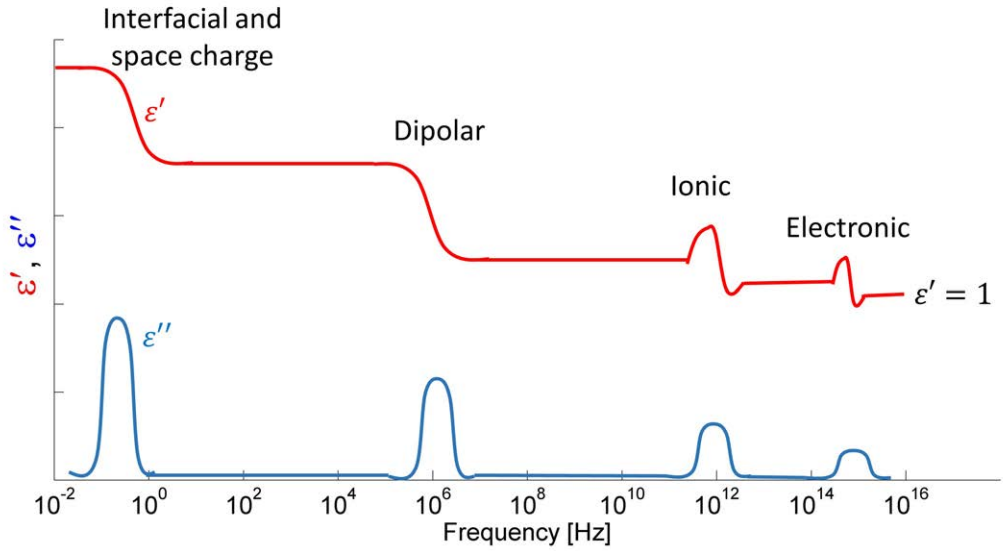

Figure 2.4. *A schematic of the real and imaginary part of complex dielectric permittivity as a function of the driving field's frequency for a material having different mechanisms of polarization [32].*

2.7 Dielectric Response in the Low-Frequency Range

An insight into the development of material's ageing may be obtained by the analysis of low-frequency dielectric spectra. Ageing leads to structural changes in the material such as the formation of cracks and voids. The appearance of any discontinuities in the uniform dielectric is associated with the interfacial or space charge polarizations. In this Section, the main patterns of dielectric relaxation are studied.

The dielectric relaxation considers the dielectric relaxation response of an ideal, noninteracting population of dipoles exposed to the alternating external electric field is generally named after Debye [20]. Neglecting interactions between individual dipoles permits the use of superposition to estimate the total response of the material. Debye's model proposes that an equilibrium is reached exponentially through an analogue of the mechanical relaxation: a motion of charged particle in the viscous media under the influence of an electric field. If

the frictional force is proportional to the velocity of the particle, then exponential term will contribute to the steady (equilibrium) velocity. The orientational polarization of dielectric consisted of polar molecules exposed to the step-like electric field follows almost the same behaviour as theoretically derived by Debye. The Debye dispersion equation defines the relation between complex dielectric permittivity of dielectric media and the field's frequency ω:

$$\varepsilon(j\omega) = \varepsilon_\infty + \frac{\varepsilon_s - \varepsilon_\infty}{1 + j\omega\tau}, \tag{2.18}$$

where ε_∞ is the permittivity at the high frequency edge of the spectra (at a frequency higher than the dipole relaxation frequency but lower than the atomic resonance frequency), ε_s is a static permittivity (at a frequency lower than the dipole relaxation frequency) and, τ is a dielectric relaxation time.

Equation (2.18) may be split into two equations of the real and imaginary components of complex dielectric permittivity to represent the dielectric character of material:

$$\begin{aligned} \varepsilon'(\omega) &= \varepsilon_\infty + \frac{\varepsilon_s - \varepsilon_\infty}{1 + (\omega\tau)^2}, \\ \varepsilon''(\omega) &= \frac{(\varepsilon_s - \varepsilon_\infty)\omega\tau}{1 + (\omega\tau)^2}. \end{aligned} \tag{2.19}$$

The curves of ε' and ε'' as functions of frequency are depicted in Figure 2.5 (only dispersion region of the spectra).

The Debye theory does not consider the contribution to the measured $\varepsilon(\omega)$ due to the DC conductivity. Conducting dielectric materials are treated as a non-conducting dielectric connected in parallel with a resistance. Thus, the complex permittivity of a conducting, polar material in Debye formulation can be presented as [35]:

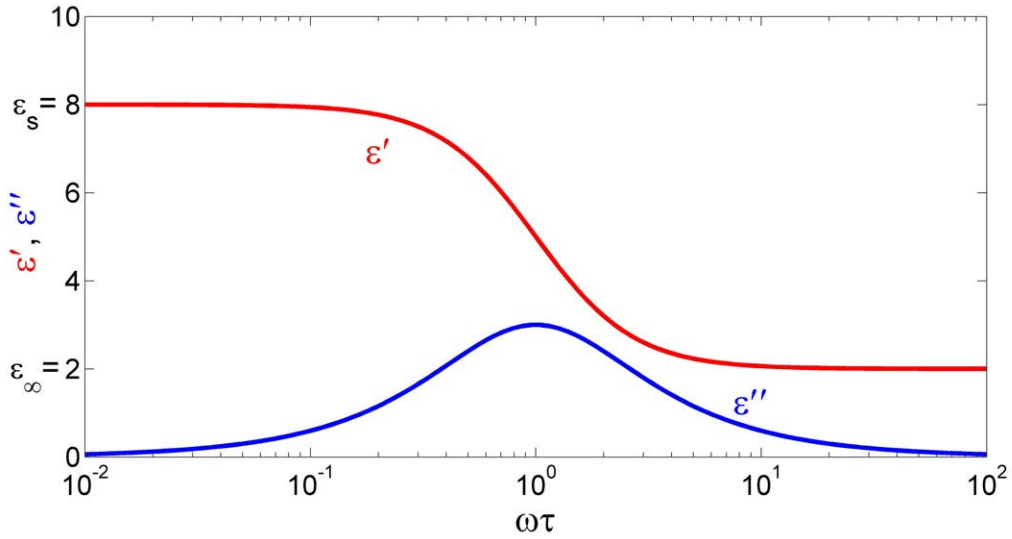

Figure 2.5. *The ideal Debye relaxation response curves of a dielectric media built from polar molecules.*

$$\varepsilon(\omega) = \varepsilon_\infty + \frac{\varepsilon_s - \varepsilon_\infty}{1 + j\omega\tau} - j\frac{\sigma}{\varepsilon_0\omega}. \tag{2.20}$$

The influence of the last term in (2.20) can be seen in Figure 2.6 where the log-log representation of $\varepsilon''(\omega)$ in case of various values of the DC conductivity is plotted [35]. Larger conductivities lead to the significant variations from the ideal Debye curve. The presence of the DC conductivity in the dielectric response measurements hides a true dielectric response whose physical interpretation is crucial for the analysis of ageing. Specific measuring techniques will be utilized in this work to avoid masking of the dielectric response caused by the DC conductivity. If the DC conductivity plays the dominant role in the low-frequency range then $\varepsilon'' \sim 1/\omega$ and $\varepsilon' \to$ const as $\omega \to 0$. This directly follows from the asymptotic analysis of (2.20).

Being part of the relaxation polarization, the interfacial polarization appears when the dielectric material contains interfaces. A widely-used theory of interfacial polarization

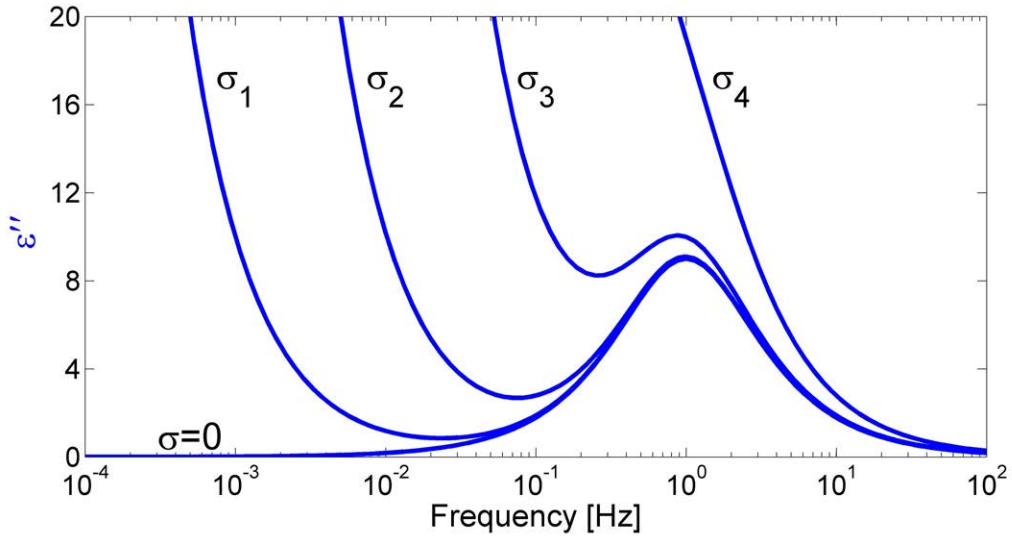

Figure 2.6. *The influence of the DC conductivity, σ, on Debye's model of relaxation polarization ($\sigma_1 < \sigma_2 < \sigma_3 < \sigma_4$).*

was developed by Maxwell and refined by Wagner [20]. Maxwell considered double-layer capacitor where each layer is modelled by the conductivity, σ_1 and σ_2, and the dielectric permittivity, ε_1 and ε_2, respectively. The complex permittivity of this connected dielectric structure mimics the Debye model including conductivity (2.20) and the time constant of the interfacial polarization process [35] is expressed as

$$\tau_{MW} = \varepsilon_0 \frac{d_1\varepsilon_2 + d_2\varepsilon_1}{d_1\sigma_2 + d_2\sigma_1} \tag{2.21}$$

where d_1 and d_2 are the thicknesses of the layers.

Dipolar polarization whose behaviour is precisely described by Debye's model is a fast phenomenon and effective up to MHz and GHz ranges. In contrast, interfacial polarization, that also obeys the Debye relaxation theory, arises in the low-frequency range (< 10 Hz). This can be verified using (2.21). Assume that $d_1 = d_2$ and the layers have following properties: one of the layers is a vacuum ($\sigma_1 = 0$ and $\varepsilon_1 = 1$) and the other is a typical

polymeric material with $\sigma_2 = 10^{-15}$ and $\varepsilon_2 = 3$. Under these assumptions τ_{MW} and its reciprocal value, characteristic frequency of this relaxation process, is $\sim 10^{-5}$ Hz.

Maxwell-Wagner polarization can be diagnosed in the dielectric response of the material if in the log-log representation of ε' and ε'' versus frequency the slopes of $\lg(\varepsilon' - \varepsilon_\infty)$ and $\lg \varepsilon''$ are -2 and -1 respectively. These approximations reflect the condition of $\omega\tau \gg 1$ in the Debye relation (2.19).

Another example of the dielectric response presented at the low-frequency range that occurs due to the hopping /trapping charged particles is a space-charge polarization. A simplified theory of this phenomenon can be derived from the transformation of a given distribution of charged particles inside the dielectric to another one after the change in the direction of the driven electric field. Assuming that the process is diffusive, it can be shown that the dielectric response matches the Debye relation [35].

However, measured dielectric response in the low-frequency range (< 10 Hz) of the majority of polymeric materials does not follow the Debye relation [34]. The main distinctions are the absence of a loss peak in the imaginary part and the strong rise of the real part of the complex dielectric permittivity (Figure 2.7). This is an attribute of what Jonsher [36] refers to as a "low-frequency dispersion" (LFD) and Dissado and Hill refer to as "quasi-DC" [37]. The Dissado-Hill theory of LFD considers the interaction/correlation effect between the relaxing species (charges or dipoles) on the net dielectric response in contrast to the Debye theory of the noninteracting population of dipoles. The dielectric medium is split into the clusters where each cluster contains dynamically connected relaxing species, and the total dielectric response is constructed as the combination of contributions from the individual clusters (intra-cluster motion) and from the cluster/cluster interactions. The output of this theory is an asymptotic frequency dependency of dielectric spectra in the low-frequency range of solid dielectrics:

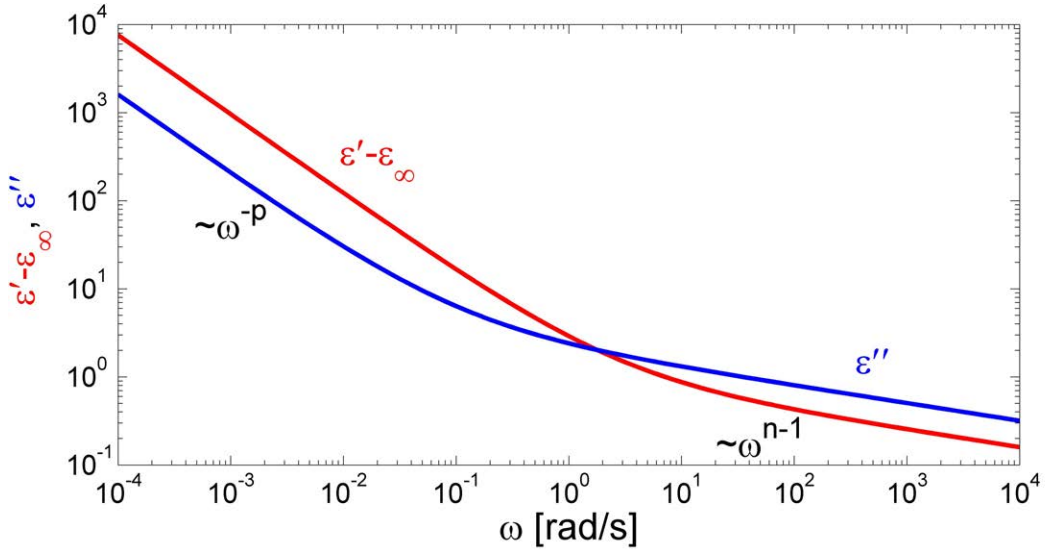

Figure 2.7. *The dielectric behaviour of a material that does not follow the the Debye relation.*

$$\begin{aligned} \varepsilon''(\omega) \sim (\varepsilon' - \varepsilon_\infty) \sim \omega^{n-1}, \text{where} \quad \omega \gg \omega_c \\ \varepsilon''(\omega) \sim (\varepsilon' - \varepsilon_\infty) \sim \omega^{-p}, \text{where} \quad \omega \ll \omega_c \end{aligned} \tag{2.22}$$

where $0 \leq n \leq 1$ is linked with the structural regularities of the dielectric material and large values of index n are associated with a highly ordered cluster, $0 \leq p \leq 1$ is the measure of the coherence of the hopping charge events and inter-cluster transfer events, ω_c is the characteristic frequency which divides low-frequency range into two regions: one where the motion of charged species is limited to the cluster and another one where hopping mechanism takes place. The LFD may be distinguished from the DC conductivity contribution to the dielectric response by the presence of the dispersion in the real part of dielectric permittivity. Although LFD bears a close resemblance to the Maxwell-Wagner model for the polarization, the difference between is the ratio of $\varepsilon''(\omega)/(\varepsilon'(\omega) - \varepsilon_\infty)$ that should be a frequency independent constant in case of LFD.

Polarization mechanisms operated at the low-frequency range and methods to distinguish them are summarized in Table 2.3. Here $\varepsilon' - \varepsilon_\infty$ and ε'' are replaced correspondingly by their equivalent χ' and χ'' for the consistency. These markers will be used to analyze the dielectric response of the material under investigation.

Table 2.3. *Polarization mechanisms of the low-frequency range and their markers.*

Mechanism	Slope of lg χ'	Slope of lg χ''
DC conductivity	0	-1
Maxwell-Wagner polarization	-2	-1
LFD	Slope of lg χ'= Slope of lg χ''	

2.8 Apparatus for the Frequency Domain Measurements

The choice of the apparatus to measure the complex dielectric permittivity depends on the nature of the sample and the frequency range under the investigation. In general, when employing dielectric spectroscopy, the material under test is investigated within one of two vast configurations: distributed-circuit and lumped-circuit methods [20]. In case of high-frequency studies (> 1 MHz), distributed-circuit methods are preferred. These include housing the material within a transmission line structure [38,39], near an open-ended coaxial probe [40] or within a resonant cavity [41].

At lower frequency ranges the sample holder (testing cell) may take the form of a parallel plate [8, 42] or a cylindrical [43] capacitor. In both cases, the space between electrodes includes the material under test that forms part or all of the dielectric between the plates of the capacitor.

When a testing cell is constructed, its equivalent capacitance can be determined using various measurement techniques. The bridge and resonance methods [20] are the most

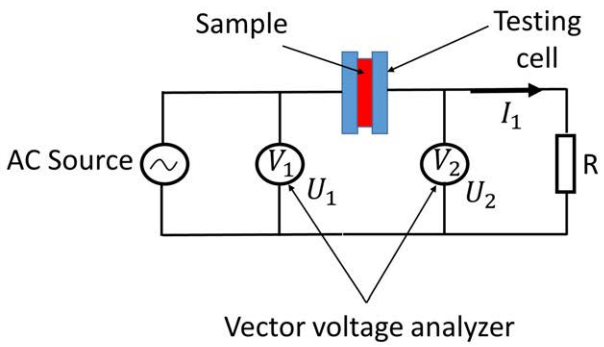

Figure 2.8. *Simplified electrical circuit of the frequency response analyzer [45].*

traditional in the frequency range from 10 Hz to 100 MHz. Among various alternative current bridges, the Schering bridge finds wide application because of the independence of its balance equation from a particular frequency. It consists of four arms (one arm is the unknown capacitor, the other three known, calibrated resistors and capacitors), an AC source, and a balance (null) detector. The capacitance measurement can also be performed using a resonant circuit where the whole or the part of the capacitance is the testing cell [44].

The principal drawback of these measurement techniques is the necessity to combine several separate instruments to carry out measurements. Current instrumentation, e.g. a frequency response analyzer (dielectric spectrometer), includes a "plug and play" feature and can cover many decades in frequency while obtaining the impedance frequency response. The basic concept of this apparatus is shown in Figure 2.8. A generator is used to provide the applied AC voltage $U_s = U_1$ of frequency ω. The resistor R is used to quantify the sample current I_s in terms of measured voltage U_2. The complex sample impedance $Z_s(\omega)$ can be calculated from the recorded data using

$$Z_s(\omega) = R(\frac{U_1}{U_2} - 1). \tag{2.23}$$

The complex dielectric permittivity can be then evaluated from $Z_s(\omega)$ knowing the

geometry of a testing cell.

2.9 Sample Arrangement

The sample placed in a testing cell introduces the disturbance to the measurement process. For example, a void, that will contribute strongly to the measurement, may be formed due to any imperfection in the contact between a capacitor plate and the sample when a sample occupies the whole space between the electrodes ("close-contact parallel plate method"). Creating complete contact with non-rigid samples such as polymeric insulators can result in the deformation of the sample and, at minimum, inaccurate determination of the plate separation. Moreover, as we have seen in Figure 2.6, the DC conductivity is not a desired "participant" in the dielectric response since it masks the dielectric character of a material.

One proposed solution to this challenge is referred to as "the contact-free parallel plate method" [1, 46], where the sample of material under the investigation is placed on the lower of two parallel plates, leaving an air gap between the sample and the second plate (Figure 2.8). An additional measurement of the capacitance with only air as the dielectric (no sample present) is used to enhance the measurement reliability. The presence of the sample is treated as a perturbation to the reference data. The test setup (Figure 2.9) includes parasitic capacitive contributions between each plate and the grounded chamber that contains the apparatus. More details on this will be given in the next Chapter where the apparatus is discussed.

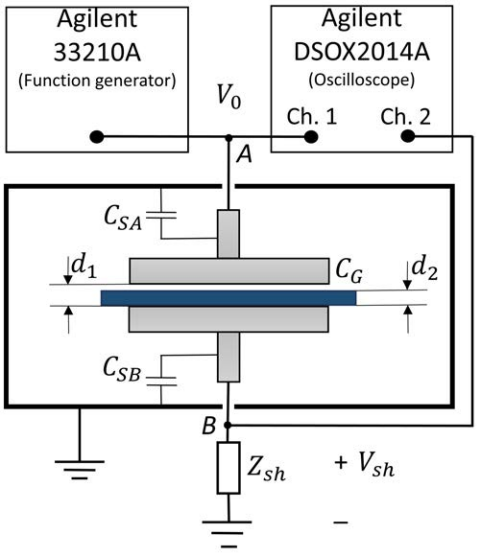

Figure 2.9. *Parallel plate measurement apparatus incorporating the principal lumped-element capacitance (C_G) and parasitic contributions (C_{SA}, C_{SB}). The two measured distances are d_1 (between the plates of the capacitor), and the thickness of a sample placed in contact with the lower plate (d_2). The setup is housed within a grounded chamber.*

Chapter 3

Apparatus

In this chapter, the theory of the contact-free parallel plate method reported in Section 2.9 to determine the complex dielectric permittivity used for the evaluation of ageing of the HV polymeric insulating materials (Chapter 2) is presented. Two realizations of the experimental setup to implement this method are discussed.

3.1 Theory of Contact-Free Parallel Plate Method

For measurements obtained via the contact-free parallel plate method, the complex dielectric permittivity is extracted directly from the capacitance formula of the lumped-element capacitor (C_G) [1, 46] that is determined from the electrical measurements utilizing apparatus associated with Figure 2.9. Employing Kirchoff's current law at node B and taking into the consideration the parasitic capacitances between each electrode and the grounded enclosure (C_{SA} and C_{SB}), the voltage and the current through the test cell can be related by:

$$j\omega C_G \left(V_A - V_B\right) - j\omega C_{SB} V_B - \frac{V_B}{Z_{sh}} = 0. \tag{3.1}$$

The current-voltage response is measured twice under the same frequency and test conditions. The "air reference" measurement is performed in the absence of a sample and is represented with the parameters: $V_A = V_0$, $V_B = V_{sh} = V_1$ and $C_1 = C_G$. With the sample in place (Figure 2.9) the current-voltage response is measured a second time and the parameters: $V_A = V_0$, $V_B = V_{sh} = V_2$ and $C_2 = C_G$ are recorded. Two expressions associated with each of the measurements can be obtained

$$\begin{cases} j\omega C_1 (V_0 - V_1) = V_1 \left(j\omega C_{SB} + \frac{1}{Z_{sh}} \right) \\ j\omega C_2 (V_0 - V_2) = V_2 \left(j\omega C_{SB} + \frac{1}{Z_{sh}} \right) \end{cases}. \tag{3.2}$$

The sample dielectric permittivity, ε', and the dielectric loss factor, $\tan\delta = \varepsilon''/\varepsilon'$, are computed from (3.1) and the geometric parameters of the test cell (Figure 2.9) as:

$$\varepsilon' = \frac{\varepsilon_{\text{air}} \left(d_r \text{Re}\{V_r\} + 1 - d_r \right)}{\left(d_r \text{Re}\{V_r\} + 1 - d_r \right)^2 + \left(d_r \text{Im}\{V_r\} \right)^2} \tag{3.3}$$

$$\tan\delta = \frac{d_r \text{Im}\{V_r\}}{d_r \text{Re}\{V_r\} + 1 - d_r} \tag{3.4}$$

where $V_r = [V_1 (V_0 - V_2)] / [V_2 (V_0 - V_1)]$ and $d_r = d_1/d_2$.

Thus, to determine the complex dielectric permittivity of a sample, corresponding electrical and spatial measurements should be conducted.

3.2 Electrical Measurements: Direct Method

The experimental setup for measuring the dielectric permittivity of high voltage insulating materials is depicted in Figure 2.9. A function generator (Agilent 33120A), that was connected to the upper (non-contacting) plate, provided a testing cell with the applied AC voltage (V_0). A shunt (formed from a 33-pF capacitor), that matched the capacitance of the sample holder, was employed to convert the combined current response of the test object

into the measured voltage V_{sh}. A digital oscilloscope (Agilent DSOX2014A) was used to acquire V_0 and V_{sh}. The frequency of V_0 was swept from 10 Hz to 10 kHz. The magnitude and phase of V_0 and V_{sh} required for (3.3) and (3.4) were extracted using a Fast Fourier Transform (FFT). Automated code controlled the function generator, read the data from the oscilloscope, and performed the data processing was implemented in Matlab.

This experimental implementation did not provide access to the full range of frequencies of interest (*i.e.* $<$ 10 Hz), however, this set of experiments was undertaken to confirm consistency between results obtained in our lab and those of others in the round-robin collaboration.

3.3 Electrical Measurements: the Solartron Dielectric Spectrometer

In order to gain insight into the low frequency range (*i.e.* $<$ 10 Hz), the function generator, the oscilloscope and the shunt of the experimental setup (Figure 2.9) was replaced by a Solartron dielectric spectrometer (Solartron Analytical Modulab XM Materials Test System). The testing cell was connected to the dielectric spectrometer at points A and B (Figure 2.9). Solartron dielectric spectrometer can measure the dielectric properties of materials over a broad frequency range, from 10 μHz to 1 MHz.

The basic principle of the unit's operation is described in Section 2.8. In order to match the large impedance range required for dielectric measurements resistor R of the simplified electrical circuit (Figure 2.9) is replaced by a broadband electrometer amplifier with variable gain [47]. The measuring current range is divided into 12 stages and the lowest one is capable of measuring currents with the resolution of 0.15 fA. Moreover, embedded HV module (up to 100 V) facilitates ultra-high impedance measurements. The Solartron software controls the dielectric spectrometer and can convert measured impedance into the

complex capacitance or, knowing the geometry of sample/electrode arrangement, into the complex dielectric permittivity.

When the dielectric spectrometer is employed, the magnitude and phase of V_r required in (3.3) and (3.4) is expressed in terms of measured impedance:

$$V_r = Z_2/Z_1 \tag{3.5}$$

where Z_1 is the impedance of an empty testing cell and Z_2 is the combined impedance of testing cell and a sample.

3.4 Testing Cells

Two sample holders were employed for dielectric spectroscopy: a commercially manufactured sample holder (Solartron 12962A Sample Holder) and the holder constructed according to the recommendations from collaborating *CIGRÉ Working Group D1.59*.

The Solartron holder (Figure 3.1) consists of the fixed ("ground" electrode) and movable ("HV" electrode) electrodes. A digital micrometer is adjoined to the movable electrode to control the electrode separation, d_1. The guard ring electrode is built in the fixed electrode in order to diminish the impact of fringing electric field. Here, the guard ring electrode is grounded through the frame of the sample holder that is connected to the common ground of the Modulab XM system. Whereas the measuring electrode with a diameter of 40 mm has virtually the same ground potential since the core and femto ammeter units of the Modulab XM system are "virtual earth" devices. Therefore, the potential difference between the guard ring electrode and the measuring electrode is negligible. As a result, the electric field lines at the periphery of the measuring electrode remain parallel to the lines near the central location. Moreover, the guard ring electrode also eliminates the contribution from the surface currents that do not have the polarization or volume DC conductivity nature

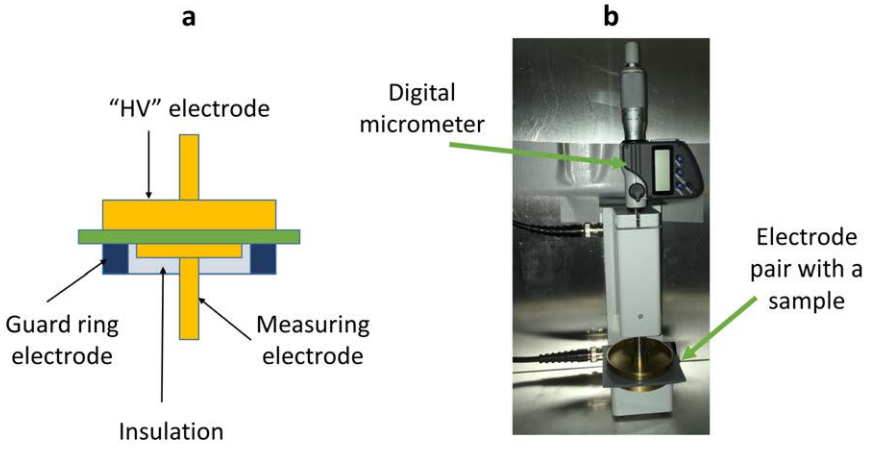

Figure 3.1. *(a) A schematic of the electrode system used in the Solartron holder. (b) A photograph of the Solartron holder placed in the grounded box.*

and are out of scope of this work.

The *CIGRÉ* sample holder is composed of two aluminium plates (diameter $D = 100$ mm) that are mounted in the frame by means of brass (upper plate) and plexiglass (lower plate) rods (Figure 3.2). The voltage is applied to the upper electrode. The frame is made up of plywood and plexiglass plates supported by two bakelite rods. The plexiglass plate is covered by aluminium foil that has a solid connection with the ground. This is done to avoid deposition of the surface charge on the plexiglass. The movable electrode is fixed on the frame using brass sleeve and a pair of screws. The separation, d_1, of the moveable top electrode relative to the fixed lower electrode was precisely measured using a set of the steel standard gauge blocks (minimum step = 0.051 mm) (Figure 3.3).

Both test cells were placed in a grounded metal box in order to minimize external interference.

A sample holder is not a perfect "participant" of measuring process due to the leakage currents that originate from the supporting materials in the frame or from the connecting

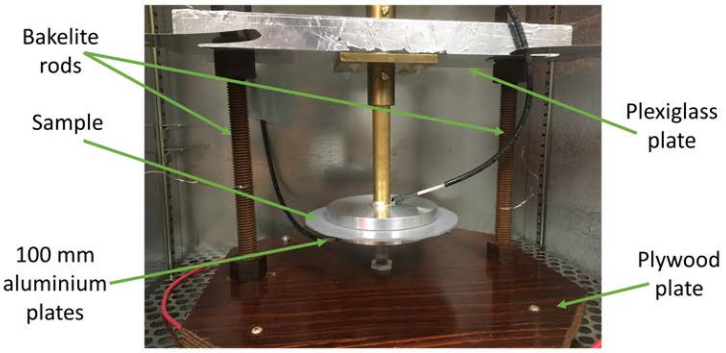

Figure 3.2. *A photograph of the CIGRÉ holder placed in the grounded box.*

Figure 3.3. *A set of the steel standard gauge blocks to determine the electrode separation of the CIGRÉ holder.*

cables. The dielectric spectrometer also contributes to unwanted measuring losses because of current losses through the amplifier. In order to quantify the measurement limit (noise floor) of the dielectric spectrometer in combination with corresponding testing cell, loss tangent (calculated by the Solartron software) studies were performed on the test cells without sample present. Figure 3.4 shows the noise floor associated with the Solartron holder, the

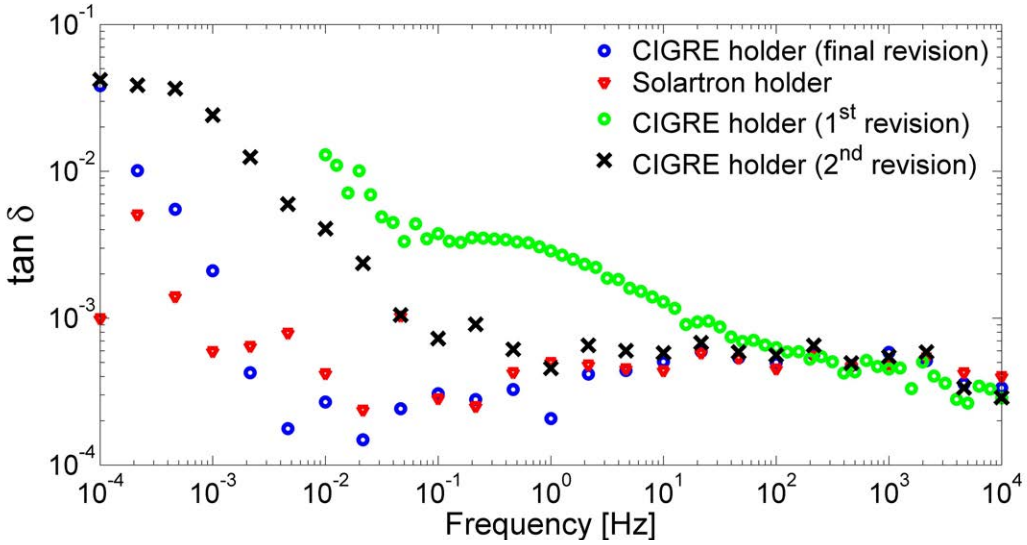

Figure 3.4. *The loss tangent measurements using the Solartron dielectric spectrometer and various sample holders demonstrate the measurement limit of the experimental setup.*

CIGRÉ holder (final design), and two prototypes of the *CIGRÉ* holder (different materials were used in the frame). It can be seen that the Solartron holder produces the least noise of the four designs. The degree of interference generated by the *CIGRÉ* holder exceeds the values of the Solartron holder and increases towards the lower frequencies. The final version of the the *CIGRÉ* holder was obtained by installing the plexiglass rod holding the lower plate instead of the brass one and replacing the top plywood plate of the frame with the one made of plexiglass. These modifications led to the decrease of the leakage currents contributed to the measured loss tangent of the empty test cell.

This noise floor is an inherent property of the experimental setup and is of the internal nature. Thus, the impedance of the empty testing cell Z_1 was obtained from its measured value reduced by the losses introduced by the sample holder (*i.e.*: only the imaginary part of measured Z_1 was used for corresponding calculations.

Figure 3.5. *The method used to measure the sample thickness.*

3.5 Sample Measurements

The sample thickness, d_2, was measured using a digital caliper and averaged over 10 readings at different locations on the sample. In order to eliminate the deformation of the sample due to the contact with the digital caliper's external jaws, the sample was housed between two sheets of acrylic to carry out the measurements of d_2 (Figure 3.5).

3.6 Geometric Correction Factor: Compensation for Fringing Effects

Distortions of the electric field lines associated with the periphery of the electrodes (fringing effect) introduce error in permittivity measurements obtained from the contact-free parallel plates [42]. Compensation of this effect could be accomplished experimentally by employing a guard electrode [48] or by using an appropriate modelling environment to calculate the edge capacitance [49]. In the present work, a finite element simulation was used to obtain a geometric correction factor (k) from the electrostatic analysis of Figure 2.9, representing

a reasonable alternative to estimating the actual edge capacitance.

A simplified finite-element model (FEM) of the sample holder (Figure 2.9) was built in *Comsol Multiphysics 5.2*. The frame was not included and the size of the grounded enclosure was decreased since the former does not modify an electric field within the area of interest and the latter does not change computed capacitance C_G. This allowed us to use a 2D axisymmetric representation. In order to calculate the capacitance of particular electrode arrangement with or without sample between electrodes, electrostatic analysis was performed. Calculation of the capacitance was based on the energy stored, for a capacitor C charged to voltage U, the energy stored can be calculated using

$$W_e = \frac{CU^2}{2}. \tag{3.6}$$

On the other hand, the same energy can be computed by integrating the electric energy density over the computational domain of the model employing

$$W_e = \int_V \omega_e dV \tag{3.7}$$

Substituting (3.5) into (3.6) yields the expression used to compute capacitance C in FEM:

$$C = \frac{2W_e}{U^2} \tag{3.8}$$

Three participating capacitances can be identified in Figure 2.9: C_{SA}, C_{SB}, and C_G. Therefore, the integral of the electric energy density is the net energy consisting of the energies stored on each participating capacitance. In order to find the required capacitance, C_G, three different formulation of boundary conditions were used:

- Grounded enclosure, $V_A = 1$ V, and $V_B = 0$,

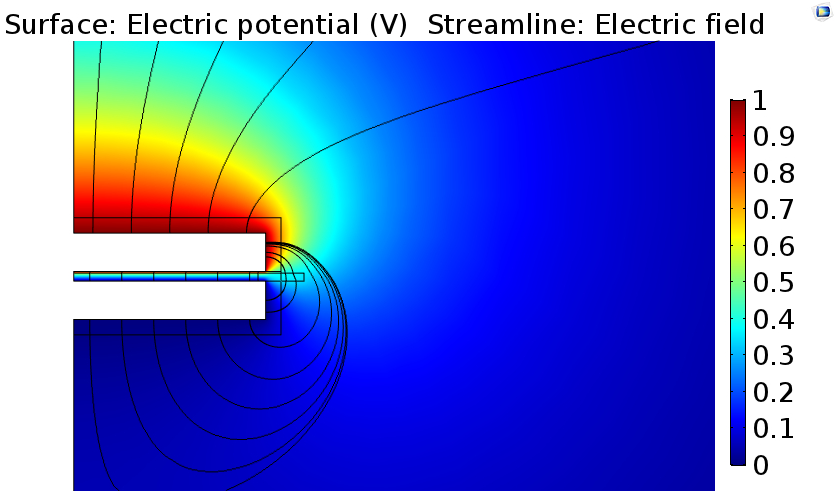

Figure 3.6. *The surface plot displaying electric potential and the electric field lines in a particular electrode/sample arrangement when the upper plate is set to 1 V.*

- Grounded enclosure, $V_A = 0$, and $V_B = 1$ V,
- Grounded enclosure, $V_A = 1$ V, and $V_B = 1$ V.

As an example, Figure 3.6 displays the electric potential distribution when $V_A = 1$ V, and $V_B = 0$ in case of one particular electrodes/sample arrangement that was under investigation in this work. Have been computed two more scenarios, finally, the system composed of three equations were constructed to determine C_{SA}, C_{SB}, and C_G:

$$\begin{cases} \frac{C_G V_A^2}{2} + \frac{C_{SA} V_A^2}{2} = W_{e1} \\ \frac{C_G V_B^2}{2} + \frac{C_{SB} V_B^2}{2} = W_{e2} \\ \frac{C_{SA} V_A^2}{2} + \frac{C_{SB} V_B^2}{2} = W_{e3} \end{cases} . \tag{3.9}$$

In order to obtain accurate result of a computer simulation, the mesh was refined until the change in the calculated C_G became less than 1 %.

The model was verified using analytical expression derived by Kirchhoff for the equal disk electrodes surrounded by an air [48]:

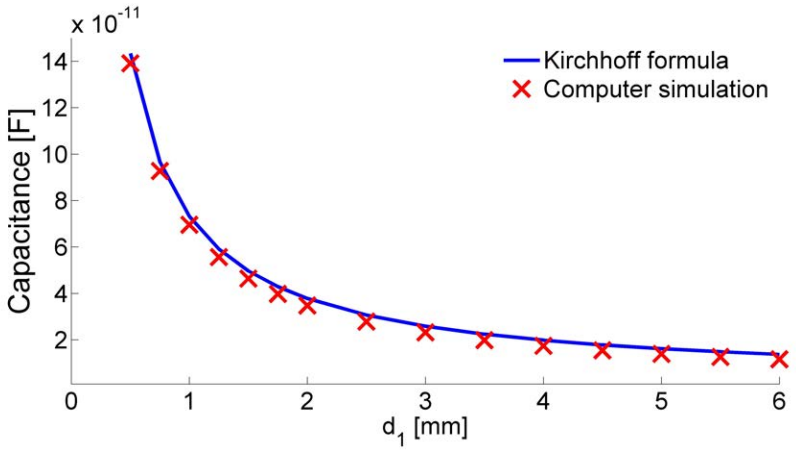

Figure 3.7. *Comparison between the Kirchhoff formula and computer simulation used for the calculation of the capacitance associated with the CIGRÉ holder without a sample.*

$$C_K = \frac{\varepsilon_0 \pi D^2}{4d_1} + \frac{\varepsilon_0 \pi D}{2}(\ln \frac{8\pi D(t+d_1)}{{d_1}^2} + \frac{t}{d_1} \ln \frac{d_1+t}{t} - 3) \tag{3.10}$$

where $t = 10.1$ mm is the thickness of electrodes. The results of computer simulation and the Kirchhoff formula are compared in Figure 3.7. The difference between two models did not exceed 0.5%.

When the method to compute capacitance using FEM was established and verified, the two capacitances, C_1 and C_2, defined above were calculated via simulation and their ratio was used to obtain a calculated permittivity ε_c for the sample by means of (3.3). A geometric correction factor was defined as $k = \varepsilon')/\varepsilon_c$. Incorporating the correction factor (k), (3.3) and (3.4) are rewritten as

$$\varepsilon' = \frac{\varepsilon_{\text{air}} k \left(d_r \text{Re}\left\{V_r\right\} + 1 - d_r\right)}{\left(d_r \text{Re}\left\{V_r\right\} + 1 - d_r\right)^2 + \left(d_r \text{Im}\left\{V_r\right\}\right)^2} \tag{3.11}$$

$$\tan\delta = \frac{d_r \text{Im}\left\{V_r\right\}}{k\left(d_r \text{Re}\left\{V_r\right\} + 1 - d_r\right\})}. \tag{3.12}$$

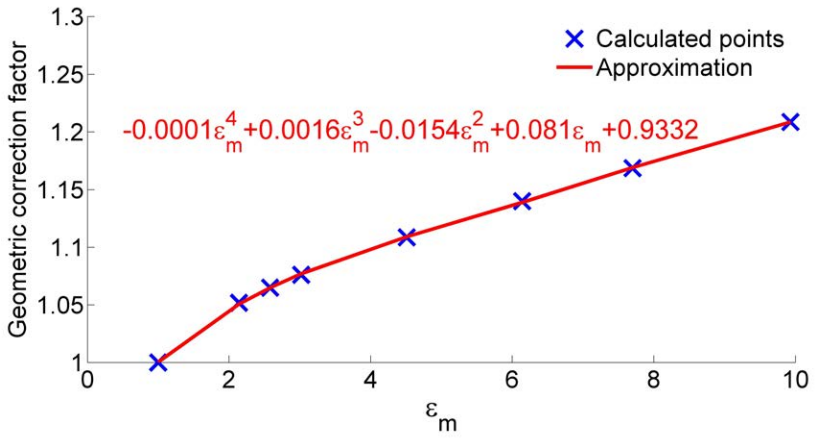

Figure 3.8. *An example of the computed geometric correction factor as a function of measured ε' for the selected electrodes/sample arrangement used in this work.*

The geometric correction factor strongly depends on the dielectric permittivity of the material, the parallel plate separation (d_1), and the sample thickness (d_2). Each electrode pair/sample arrangement investigated in this work was analyzed separately for the wide range of ε'. The set of k as a function of measured ε' was approximated by the fourth-degree polynomial using the method of least squares utilized in Matlab (Figure 3.8). Then this function was used to make correction in ε' and $\tan\delta$.

Chapter 4

Method

In this chapter, the tested polymer samples, experimental methodology, and proposed ageing procedures are discussed. The knowledge of sample composition and morphology is an important component in the analysis of dielectric response of new and aged material. Two mechanisms of ageing were studied: one associated with the uptake of water via a range of diffusion mechanisms and a second that focused on accelerated ageing as a consequence of uniform and gradient temperature environments. Finally, to quantify the accuracy of the contact-free parallel plate method to determine the complex dielectric permittivity, an original sensitivity analysis is undertaken.

4.1 Materials under Test

Test samples of liquid silicone rubber (LSR), high temperature vulcanized (HTV) silicone rubber, ethylene propylene diene monomer (EPDM) rubber, two types of epoxy cast (structural) material (W12 and W12 EST), and a fiber reinforced epoxy plastic (FRP) were studied. All the samples had a commercial origin (Lapp Insulators GmbH) and were examined in conjunction with an international collaboration coordinated by the *CIGRÉ working group D1.59*. In this section, a review of processing, physical and chemical properties and

application is introduced in order to juxtapose them with the measured dielectric response.

LSR and HTV are silicone rubbers that are widely used as a housing material for composite insulators that separate bare conductors of the power line from the tower structure. This choice is accounted for high resistance to the environmental influence and outstanding hydrophobic properties of the surface [5]. The term silicone rubber usually refers to a group of polymeric materials that have a silicon/oxygen chain as the backbone of the basic polymer [19]. In general, silicone rubber for HV outdoor insulation purposes consists of a basic polymer and various fillers, catalysts and other additives. The raw rubber used in the formulation of LSR and HTV is polydimethylsiloxane (PDMS) whose molecular structure is composed of an alternating combination of silicon and oxygen atoms as the main chain and a symmetrical arrangement of methyl groups attached to the silicon atoms as the side chains correspondingly [50]. High pressure injection moulding (up to 250 bar) with high curing temperatures (130-180 °C) is applied to obtain HTV silicone rubber insulating structures from the mixture of PDMS and aluminum trihydrate (ATH). LSR insulation is produced from pure PDMS by means of low pressure moulding (up to 10 bar) with relatively low curing temperatures (50-80 °C) [51]. The benefits of adding ATH to the silicone rubber formulation are better mechanical and thermal properties, and enhanced resistance to the tracking/erosion [52].

EPDM is a type of synthetic rubber that has a wide range of HV applications. Nowadays, the prime and most important use of EPDM as an insulating material is in the power cables and in their accessories, such as cable terminations and joints [53]. Despite of low hydrophobic recovery rate [54] in comparison with silicone rubber, EPDM is still a preferred choice for housing of composite insulators because of its cost effectiveness [55]. The popularity of EPDM is accounted for the good surface and volume resistance, good performance in the contaminated environment and high breakdown voltage [56]. From the chemical point of view EPDM originates from the copolymerization of ethylene and propylene in the

presence of certain chemical compounds. Additives such as antioxidants and antiozonants are used to achieve higher resistance to the influence of atmospheric conditions.

W12, W12 EST, and FRP are composite insulating materials containing epoxy resin as the polymeric matrix and quartz powder (W12 and W12 EST) and glass fibers (FRP) as mineral fillings. Mineral filled epoxy resins find increased application in a wide range of HV equipment where high mechanical and high electrical strength in addition to the resistance to the various atmospheric conditions is in demand, for instance, support insulation for outdoor substations, post and suspension insulators for outdoor transmission lines, medium voltage switchgears and transformer bushings [16]. The chemical cross-linking of epoxy resins in presence of filler material and different additives (e.g. hardening and accelerating agents) is performed via a catalytic mechanism or via the bridging across epoxy molecules through the epoxy or hydroxyl groups [19]. Quartz powder with special surface treatment (epoxy silanization) is used to improve long-term performance of outdoor insulating structures (W12 EST).

The dielectric response at the low frequency range is linked with the morphology of a material that is partially defined by interfaces [21, 57]. In general, interfaces can be divided into four categories [16]: microscopic, macroscopic, internal, and external. Microscopic interfaces (interphases) are formed when polymeric matrix is combined with reinforcing mineral fillers such as powder, fibres, and whiskers. Modern composite polymeric insulators consisting of a FRP rod with metal end fittings and a weather protected cover made of silicone or ethylene propylene rubber represent examples of an insulating structures with macroscopic interfaces. Internal interfaces are inherent to all real dielectric materials since it is impossible to produce an air-void-free polymeric material. External interfaces arise when solid surface encounters with a liquid or gaseous phase (*e.g.* in contact-free parallel plate method it is the interface between a sample and remaining air gap).

4.2 Measurement Technique

The dielectric response over a frequency range from 0.1 mHz to 10 kHz of aged and new samples was measured using a Solartron dielectric spectrometer (Solartron Analytical Modulab XM MTS) in combination with either the Solartron holder (12962A Sample Holder) or the *CIGRÉ* holder. The magnitude of the applied AC voltage was chosen to be 100 V to obtain higher signal-to-noise ratio. At each frequency, the data were recorded over three cycles to carry out averaging and filtering performed by Solartron software. All dielectric response tests were carried out at room temperature.

4.3 Sample Arrangement Tests

When the testing cell is represented by a lumped parallel plate capacitor, two sample arrangements are possible: one where the sample configures all space between plates (close-contact method) and a second that leaves the air gap between a sample and one of the plates (contact-free method). The contact-free sample/electrodes arrangement has several advantages (Section 2.9). In order to make a comparison between these two methods the dielectric spectroscopy measurements were carried out on HTV, LSR and EPDM samples.

The Solartron holder was chosen to perform contact-free and close-contact measurements since it is equipped with the micrometer to define electrode separation (the principal source of measurement uncertainty discussed in Section 4.6). The application of the *CIGRÉ* holder for the close-contact measurements was obstructed by the inability to match the electrode separation with a corresponding sample thickness using the available set of the steel standard gauge blocks. The complex dielectric permittivity was evaluated from the corresponding close-contact measurements by incorporating them into (3.11) and (3.12) and supposing that the electrode separation is equal to the thickness of a sample ($d_r = 1$).

Samples (three of each type of material) were cut in the form of square slabs with a

Table 4.1. *Variation of the sample thickness [mm] measured using a digital caliper and averaged over 10 readings at different locations on the sample.*

Material	#	Mean	Stand. Dev.	Max	Min
EPDM	1	2.30	0.02	2.32	2.26
	2	2.50	0.02	2.53	2.47
	3	2.53	0.02	2.56	2.51
LSR	1	1.76	0.02	1.81	1.73
	2	1.74	0.03	1.78	1.7
	3	1.76	0.02	1.79	1.72
HTV	1	2.07	0.03	2.12	2.02
	2	2.03	0.06	2.12	1.96
	3	2.02	0.06	2.12	1.92

side size of 60 mm to suit the Solartron sample holder. The sample thickness required for the calculation of complex dielectric permittivity and its variability (source of uncertainty in measurements as it will be discussed in Section) is outlined in Table 4.1. Prior to measurements all samples were cleaned with isopropyl alcohol using low-lint wipes (Kimwipes).

4.4 Water Immersion Ageing

The materials under consideration are composite polymeric insulating materials that involve more than one dielectric component. These composites have interfaces which, as discussed above, are presumed to have a key role in most/all ageing mechanisms [16]. In the case of composite insulating materials for outdoor HV application, that face a moisture attack (high relative humidity, rain, and spray), ageing may be associated with an absorption of water molecules from the air into the interfaces. Here, water modifies the physical and chemical interaction between components of a composite dielectric due to the initiation of the different hydrolysis reactions and the breaking of filler/resin bonding. This process leads to the drastic deterioration of the initial dielectric character.

The water immersion ageing procedure agreed by the participants of *CIGRÉ working*

group D1.59 was a variation of an established protocol [7, 58]. The samples were housed in a glass container and covered with deionised water for 50 days at room temperature. To examine possible reversibility of the water absorption the drying at 100 °C for 96 hours was implemented. After each possible mass changing step, the sample was weighed with a digital balance (Mettler Toledo PB303-S/Fact), which has a resolution of 0.01 g. The first steady reading was treated as an actual weight of the sample. Table 4.2 lists all steps in the water immersion ageing protocol.

Table 4.2. *Steps in the water immersion ageing procedure that has been undertaken. Upon the completion of certain steps of ageing procedure, the dielectric charter was assessed. The contact-free parallel plate method with the CIGRÉ holder was chosen to perform the dielectric spectroscopy measurements.*

#	Step	Reason
1	Cleaning with isopropyl alcohol	To remove any deposited surface charge and any contaminants
2	Weighing	To monitor the process of water absorption
3	Dielectric spectroscopy	Material characterization
4	Drying at 100°C for 6 hours	To remove moisture from specimen before the test
5	Cooling for 30 min at room temperature	All dielectric response tests were carried out at room temperature
6	Cleaning with isopropyl alcohol	To remove any deposited surface charge and any contaminants
7	Dielectric spectroscopy	Material characterization
8	Water immersion for 50 days	Ageing procedure
9	Wiping with low-lint wipes	To prepare for the weighting
10	Weighing	To monitor the process of water absorption
11	Cleaning in an ultrasonic bath with isopropyl alcohol for 5 minutes	To remove possible appearance of aquatic plants, such as algae and fungus, on the sample's surface
12	Drying in air at room temperature for 5 minutes	To prepare for the material characterization
13	Cleaning with isopropyl alcohol	To remove any deposited surface charge and any contaminants
14	Dielectric spectroscopy	Material characterization
15	Drying at 100°C for 96 hours	To check the reversibility of water absorption
16	Cooling for 30 min at room temperature	All dielectric response tests were carried out at room temperature
17	Weighing	To monitor the process of drying
18	Cleaning with isopropyl alcohol	To remove any deposited surface charge and any contaminants
19	Dielectric spectroscopy	Material characterization

One sample of each material discussed above was tested. Samples were cut in either rectangular or circular slabs that exceeded the size of the electrodes employed in CIGRE

Table 4.3. *Variation of the sample thickness measured using a digital caliper and averaged over 10 readings at different locations on the sample.*

Material	Mean	Stand. Dev.	Max	Min
EPDM	2.40	0.03	2.44	2.35
LSR	1.74	0.03	1.78	1.71
HTV	2.08	0.04	2.13	2.02
W12	4.07	0.04	4.12	4.01
W12 EST	4.07	0.03	4.12	4.03
FRP	4.14	0.03	4.19	4.09

holder ($D = 100$ mm). The contact-free electrode arrangement was employed (Figure 2.9). The thickness of the samples that is critical in the determination of the complex dielectric permittivity is summarized in Table 4.3.

4.5 Thermal Gradient and Uniform Temperature Ageing

An accelerated ageing test should mimic real service conditions but this does not always occur. For example, thermal ageing at higher uniform temperatures [6] is a widely used technique in the assessment of thermal endurance characteristics of the polymeric materials that serve as an insulation in manufacturing of power cables. However, at least from the chemical standpoint, chemical reactions occurred at higher temperatures are not equivalent to those at lower temperatures [22]. Additionally, a radially varying temperature distribution arises in the bulk of insulation of a power cable in operating conditions because of the Joule heating of the conductor on the internal side and the ambient temperature on the external side. Whilst the presence of thermal gradient is examined with the focus on the formation of a permittivity/conductivity gradient that initiates space charge accumulation in the polymeric insulation exposed to DC electric fields [59], it does not attract attention of the existing ageing protocols.

To examine the influence of thermal gradient on ageing process, we have designed and

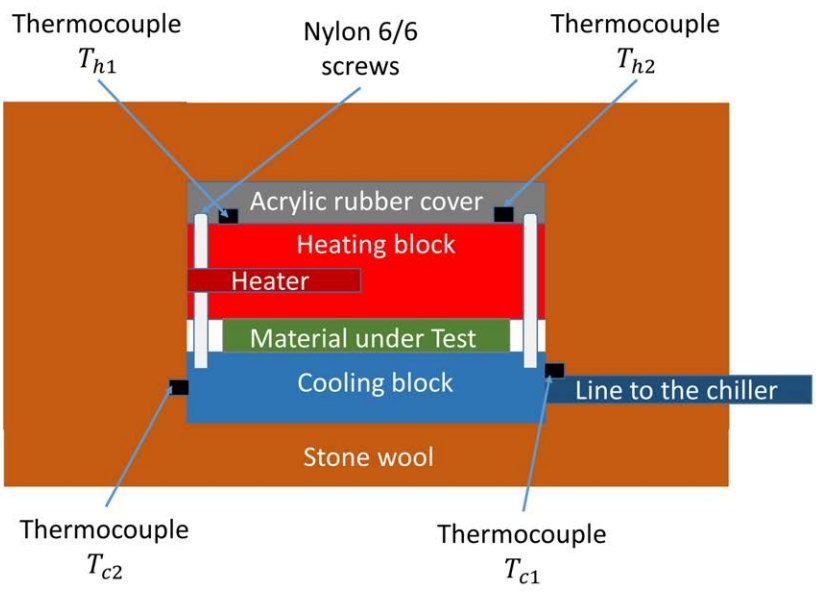

Figure 4.1. *The test unit that applies a constant thermal gradient to a sample of insulation material.*

constructed a testing module that generates a constant thermal gradient across a sample of insulation material. Figure 4.1 shows the sketch of the thermal gradient module designed in this work. In principle, the design is rather simple, it consisted of two parallel square blocks with the sample under investigation placed between them. Both blocks have a dimension of 76.2 mm by 76.2 mm but slightly different thicknesses (25.5 mm - the upper (heating) block and 21.5 mm - the lower (cooling) block). This arrangement of heating and cooling blocks was selected to mitigate the influence of convection. The blocks and a sample between them were fastened by 7 nylon 6/6 screws equidistantly located at the edge of the blocks.

The upper block machined from a sheet of aluminum represented the high temperature edge of the thermal gradient. A 20V, 100 W heater (Omega Engineering) fitted inside of this block was used to raise its temperature. In order to adjust the temperature of the heating block a variable autotransformer was used as a voltage source for the heater. Two

K-type thermocouples were installed at different locations on the top of the heating block to control the temperature, T_{h1} and T_{h2}. A Fluke 116 multimeter was used to read the temperature. The heater was about 25 mm long and was placed asymmetrically in the heating block. Thus, we have defined the temperature of the heating block as an average of T_{h1} and T_{h2}.

The (lower) cooling block was a commercial liquid heat exchanger (Custom Thermoelectric) that was connected to the recirculated chiller (Neslab Thermo Scientific M33 Merlin) with a coolant made of 50/50 mixture of distilled water and ethylene glycol to reduce the freezing point. Two K-type thermocouple was mounted on the side of the cooling block to monitor the temperature (T_{c1} and T_{c2}) of the cold edge of a temperature drop during operation. The temperature of the cooling block was chosen to be an average of T_{c1} and T_{c2} to take into account the variation of temperature within the block (T_{c1} thermocouple is located close to the input/output connections of the liquid heat exchanger and T_{c2} thermocouple is placed on the opposite side).

The coolant temperature at the output of the recirculating chiller (T_{ch}) and a room temperature (T_r) were also monitored to control the influence of the environment on the experiment. The entire test module was covered with stone wool material and placed inside a thermal insulating enclosure to stabilize the temperature by minimizing thermal interferences from the surrounding environment. A thermal conductive grease (Omegatherm 201) was used to improve thermal contact between arising interfaces: the heater, thermocouples, and aluminum blocks.

Some alternatives to our design exist: the application of two Peltier modules [60] could create the temperature gradient. The drawback of this structure is low cooling capability. In [59], two liquid heat exchangers were used to generate a thermal gradient. This design requires two separate pumps that makes it more complex. Authors of [61] employed a similar concept that we have used but their design is only applicable to thin film samples

placed on a glass substrate with the thickness of 0.5 mm. In contrast, our module can apply the thermal gradient to samples of macroscopic thickness, such as HV insulating samples, without any support.

The impact of ageing in thermal gradient environment is compared to ageing in a uniform temperature environment using EPDM rubber material that finds application in the insulation of power cables and their accessories. The EPDM rubber samples were cut into plate shaped pieces of dimension 60 mm×60 mm (to fit the Solartron holder). The samples were cleaned with isopropyl alcohol to remove any contaminants. The uniform temperature ageing was conducted using a laboratory oven. Both accelerated ageing procedures lasted for 600 hours.

The common reference point to perform a comparison was selected: a temperature of uniform ageing (T_u) had to be equal to the temperature of the high temperature edge of the thermal gradient. In our procedure this temperature was 100 °C as it was used in the protocol of the uniform temperature ageing of EPDM samples during 600 hours suggested by Ehsani *et al.* [62]. The assessment of ageing was carried out using dielectric spectroscopy measurements over the frequency range 0.1 mHz - 10 kHz utilizing the close-contact parallel plate method and the Solartron holder. The choice of close-contact arrangement is a forced step since a material has changed its shape after the ageing procedure and was no longer suitable for a contact-free arrangement. The mass and thickness of the samples were also monitored to evaluate the effect of ageing.

4.6 Sensitivity Analysis

Whilst "contact-free parallel plate measurement technique" to measure the complex dielectric permittivity of a sample has generated considerable interest [1, 8], few researches have addressed the question of the sensitivity of the measurement method. In this section, a comprehensive sensitivity analysis will be performed for the "contact-free parallel plate

measurement technique" implemented in Figure 2.9.

The total uncertainty associated with the determination of ε' and $\tan\delta$ can be derived by analyzing the uncertainties introducing by corresponding terms within (3.11) and (3.12) [63]. In order to quantify these, the partial derivative of the function ε' (or $\tan\delta$) with respect to each of the direct measurement terms (d_r, V_r) and each of the calculated parameters (ε_{air} and k) was examined. The resulting uncertainty in ε' is expressed as

$$\Delta\varepsilon' = \sqrt{\left(\frac{\partial\varepsilon'}{\partial d_r}\Delta d_r\right)^2 + \left(\frac{\partial\varepsilon'}{\partial V_r}\Delta V_r\right)^2 + \left(\frac{\partial\varepsilon'}{\partial\varepsilon_{\text{air}}}\Delta\varepsilon_{\text{air}}\right)^2 + \left(\frac{\partial\varepsilon'}{\partial k}\Delta k\right)^2} \tag{4.1}$$

where $\left(\frac{\partial\varepsilon'}{\partial d_r}\Delta d_r\right)^2$ reflects the contribution from uncertainties in the spatial measurement variables (d_1 and d_2); $\left(\frac{\partial\varepsilon'}{\partial V_r}\Delta V_r\right)^2$ represents uncertainty in the electrical measurements due to electrical noise; $\left(\frac{\partial\varepsilon'}{\partial\varepsilon_{\text{air}}}\Delta\varepsilon_{\text{air}}\right)^2$ represents error introduced by setting $\varepsilon_{\text{air}} = 1$; and $\left(\frac{\partial\varepsilon'}{\partial k}\Delta k\right)^2$ is the uncertainty in the estimated geometric correction factor. For $\tan\delta$, the only contributing terms are those associated with the spatial measurement, the electrical noise, and the estimated geometric correction factor:

$$\Delta\tan\delta = \sqrt{\left(\frac{\partial\tan\delta}{\partial d_r}\Delta d_r\right)^2 + \left(\frac{\partial\tan\delta}{\partial V_r}\Delta V_r\right)^2 + \left(\frac{\partial\tan\delta}{\partial k}\Delta k\right)^2}. \tag{4.2}$$

Each uncertainty contribution in (4.1) and (4.2) requires a separate consideration.

The uncertainty in spatial measurement (d_r) rests on two uncertainty terms: one associated with the electrode separation (Δd_1) and a second linked with the thickness of the sample (Δd_2). The partial derivatives of ε' and $\tan\delta$ with respect to d_1 are employed to derive the expression for the respective contributions to the relative uncertainty in ε' and $\tan\delta$:

$$\begin{aligned}\frac{|\Delta\varepsilon'|_{d_1}}{\varepsilon'} &= \left|\frac{\varepsilon'\left(\tan^2\delta-1\right)\left(\varepsilon_{\text{air}}-\varepsilon'\left(\tan^2\delta+1\right)\right)}{\varepsilon_{\text{air}}}-\frac{2\tan^2\delta}{\tan^2\delta+1}\right|\frac{\Delta d_1}{d_1}\\ &\approx \left|\varepsilon'^2-\varepsilon'\right|\frac{\Delta d_1}{d_1}\end{aligned}, \tag{4.3}$$

$$\begin{aligned}\frac{|\Delta\tan\delta|_{d_1}}{\tan\delta} &= \left|\frac{\varepsilon_{\text{air}}-\varepsilon'\left(\varepsilon_{\text{air}}-\varepsilon'\left(\tan^2\delta+1\right)\right)\left(\tan^2\delta+1\right)}{\varepsilon_{\text{air}}}\right|\frac{\Delta d_1}{d_1}\\ &\approx \left|\varepsilon'^2-\varepsilon'+1\right|\frac{\Delta d_1}{d_1}\end{aligned}, \tag{4.4}$$

Similarly, the relative uncertainty in ε' and $\tan\delta$ due to the uncertainty in the measuring of d_2 is defined as

$$\begin{aligned}\frac{|\Delta\varepsilon'|_{d_2}}{\varepsilon'} &= \left|\frac{\varepsilon'\left(\tan^2\delta-1\right)\left(\varepsilon_{\text{air}}-\varepsilon'\left(\tan^2\delta+1\right)\right)}{\varepsilon_{\text{air}}}-\frac{2\tan^2\delta}{\tan^2\delta+1}\right|\frac{\Delta d_2}{d_2}\\ &\approx \left|\varepsilon'^2-\varepsilon'\right|\frac{\Delta d_2}{d_2}\end{aligned}, \tag{4.5}$$

$$\begin{aligned}\frac{|\Delta\tan\delta|_{d_2}}{\tan\delta} &= \left|\frac{\varepsilon_{\text{air}}-\varepsilon'\left(\varepsilon_{\text{air}}-\varepsilon'\left(\tan^2\delta+1\right)\right)\left(\tan^2\delta+1\right)}{\varepsilon_{\text{air}}}\right|\frac{\Delta d_2}{d_2}\\ &\approx \left|\varepsilon'^2-\varepsilon'+1\right|\frac{\Delta d_2}{d_2}\end{aligned}. \tag{4.6}$$

The approximation expressions in (4.3),(4.4),(4.5), and (4.6) are derived assuming that $\tan^2\delta \longrightarrow 0$ for typical HV polymeric materials ($\tan\delta < 1$) and $\varepsilon_{\text{air}} = 1$. The relative uncertainty in ε' and $\tan\delta$ are monotonically increasing functions of ε' and decreasing functions of d_1 and d_2.

The uncertainty of the electrode separation (Δd_1) was chosen as a difference between two separate techniques to determine d_1, one where d_1 was measured using the set of the

standard gauge blocks and a second associated with current-voltage response measurements with the sample inserted between the electrodes as discussed in Section 3.1. To determine the electrode separation from the current-voltage response, two measurements were conducted while the movable top electrode was fixed. First, the current-voltage response of the capacitance formed by the given air gap (d_1) was measured. Next, a metal shim (with thickness g and the same diameter as the electrodes) was placed on the bottom electrode and the current-voltage response of the capacitance generated by a decreased air gap ($d_1 - g$) was measured. The current-voltage response obtained from the first scenario could be treated as the "reference" measurement, while the second scenario imitated the "sample" measurement. The initial electrode separation (d_1') was evaluated using a ratio of the aforementioned measurements, corresponding geometric correction factors and a thickness of inserted metal shim. Finally, the accuracy of measured electrode separation (Δd_1) was computed as:

$$\Delta d_1 = \left| d_1' - d_1 \right| = \left| \frac{g}{1 - \frac{k_1}{k_0 \mathrm{Re}\{V_r\}}} - d_1 \right|, \tag{4.7}$$

where k_0 and k_1 are geometric correction factors for d_1 and $d_1 - g$, respectively. An average value for Δd_1= 0.07 mm (standard deviation 0.05 and maximum 0.2 mm) was obtained from 15 independent measurements using this approach with the *CIGRÉ* holder. The level of uncertainty in $Re\{V_r\}$ does not modify significantly Δd_1 as it will be shown further.

The uncertainty in d_2 (Δd_2) depends on the variability of the thickness of the material under the consideration. The maxima of Δd_1 and Δd_2 were chosen to represent the upper bound of uncertainty due to the spatial measurements.

Analogously, the of sensitivity of ε' and $\tan\delta$ to the uncertainty in V_r is calculated through the corresponding derivatives with respect to $\mathrm{Re}\{V_r\}$ and $\mathrm{Im}\{V_r\}$ because both magnitude and angle of V_0 and V_{sh} are affected by the electrical noise:

$$\begin{aligned}\frac{|\Delta\varepsilon'|_{V_r}}{\varepsilon'} &= \frac{d_r\varepsilon'}{\varepsilon_{\text{air}}}\sqrt{\left[\left(\tan^2\delta-1\right)\Delta\text{Re}\left\{V_r\right\}\right]^2+\left(2\tan\delta\text{Im}\left\{V_r\right\}\right)^2} \\ &\approx d_r\varepsilon'\Delta\text{Re}\left\{V_r\right\}\end{aligned}, \tag{4.8}$$

$$\begin{aligned}\frac{|\Delta\tan\delta|_{V_r}}{\tan\delta} &= d_r\left(\tan^2\delta+1\right)\frac{\varepsilon'}{\varepsilon_{\text{air}}}\sqrt{\left(\Delta\text{Re}\left\{V_r\right\}\right)^2+\left(\Delta\text{Im}\left\{V_r\right\}/\tan\delta\right)^2} \\ &\approx d_r\varepsilon'\frac{\Delta\text{Im}\left\{V_r\right\}}{\tan\delta}.\end{aligned} \tag{4.9}$$

The approximations in (4.8) and (4.9) were attained supposing that $\tan^2\delta \longrightarrow 0$ for typical insulating material ($\tan\delta < 1$) and $\varepsilon_{\text{air}} = 1$. It can be noticed that the relative uncertainty in both ε' and $\tan\delta$ increases linearly with ε' and can be reduced choosing $d_r \longrightarrow 1$ (in general, $d_r > 0$ by the definition). The factors $\Delta\text{Re}\left\{V_r\right\}$ and $\Delta\text{Im}\left\{V_r\right\}$ mostly define the uncertainty in $\frac{|\Delta\varepsilon'|_{V_r}}{\varepsilon'}$ and $\frac{|\Delta\tan\delta|_{V_r}}{\tan\delta}$ respectively. The parameters of uncertainty, $\Delta\text{Re}\left\{V_r\right\}$ and $\Delta\text{Im}\left\{V_r\right\}$, can be found by using a current-voltage response procedure with and without sample on the the unchanged electrode separation. The first measurement served as the "reference" measurement, while the second, replicate, measurement is used in stead of the "sample" measurement. Assuming the physical parameters of the apparatus remained the same during two tests, the deviation of measured $Re\left\{V_r\right\}$ from 1 and $\text{Im}\left\{V_r\right\}$ from 0 gave an estimation of $\Delta\text{Re}\left\{V_r\right\}$ and $\Delta\text{Im}\left\{V_r\right\}$ for the whole range of frequencies (1 Hz to 10 kHz was considered for this study). For the experimental setup shown in Figure 2.8 with the Solartron Analytical Modulab XM MTS (Materials Test System) connected at the points A and B the measured results of $\Delta\text{Re}\left\{V_r\right\}$ and $\Delta\text{Im}\left\{V_r\right\}$ for 5 replicate measurements are shown in Table 4.4.

The maxima of $\Delta\text{Re}\left\{V_r\right\}$ and $\Delta\text{Im}\left\{V_r\right\}$ were chosen to represent the upper bound of uncertainty due to electrical noise.

Another component of uncertainty in *varepsilon\prime* arises from the assumption $\varepsilon_{\text{air}} = 1$ that was estimated using [64]:

Table 4.4. *Measured results of $\Delta Re\{V_r\}$ and $\Delta Im\{V_r\}$ obtained using the Solartron instrument.*

	Number of replicate measurements	Average	Standard deviation	Maximum
$\Delta\mathrm{Re}\{V_r\}$	5	1.1×10^{-4}	9.3×10^{-5}	6×10^{-4}
$\Delta\mathrm{Im}\{V_r\}$	5	1.8×10^{-5}	1.8×10^{-5}	0.9×10^{-4}

$$\Delta\varepsilon_{\mathrm{air}} = \varepsilon_{\mathrm{air}} - 1 = (1.58\frac{P_d}{T} + 1.34\frac{P_r}{T} + 7600\frac{P_r}{T^2})\times10^{-6}, \tag{4.10}$$

where P_d is the local pressure of dry air, P_r is the ambient partial pressure of water vapour, and T is the temperature (in K). The partial derivative of ε' with respect to $\varepsilon_{\mathrm{air}}$ expresses required uncertainty evaluating at $\varepsilon_{\mathrm{air}} = 1$:

$$\frac{\partial\varepsilon'}{\partial\varepsilon_{\mathrm{air}}}\Delta\varepsilon_{\mathrm{air}} = \frac{\varepsilon'}{1}\Delta\varepsilon_{\mathrm{air}} \tag{4.11}$$

in which the relative humidity (P_r/P_d) has the strongest impact on $\Delta\varepsilon_{\mathrm{air}}$. Relative humidity values within 0-100% yield to a range of $\Delta\varepsilon_{\mathrm{air}}$ values from 5.5×10^{-3} to 8×10^{-4}. Thus, the largest uncertainty due to the assumption of $\varepsilon_{\mathrm{air}} = 1$ in the air reference calculations can be estimated as $10^{-3}\varepsilon'$.

Finally, the calculation of the geometric correction factor (k) was performed assuming that electrodes are parallel. If electrodes are not perfectly parallel then the uncertainty in k arises. In order to quantify the lack of parallelism in the electrodes an angle (α) was introduced: the angle between the inner surface of the top electrode and a true parallel of the fixed lower electrode (Figure 2.8).

The variation of the geometric correction factor, Δk, due to the appearance of a tilt angle of α was numerically obtained using finite element method. Both $\frac{|\Delta\varepsilon'|_k}{\varepsilon'}$ and $\frac{|\Delta\tan\delta|_k}{\tan\delta}$ are equal to $\Delta k/k$.

The contributions from the the four key sources of uncertainty in the measured quantities ε' and $\tan\delta$ was implemented for the results of the experiments discussed in the next

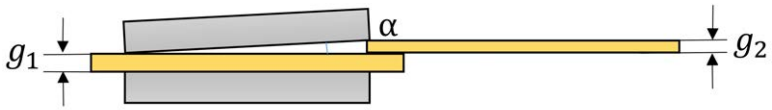

Figure 4.2. *Sketch of the electrode arrangement that defines the electrode tilt angle α (g_1 and g_2 are thicknesses of the standard gauge blocks used).*

Chapter.

4.7 Assessment of the Dielectric Spectra

To implement the analysis of the dielectric spectra reported in Section 2.7, the complex dielectric permittivity is converted to the complex electric susceptibility employing

$$\chi = \chi' - j\chi'' = \varepsilon - \varepsilon_\infty, \tag{4.12}$$

where ε_∞ is associated with the high-frequency contribution to the polarization but is beyond the range of frequencies under consideration. For most samples, the real part of the electric susceptibility was not considered at frequencies above 100 Hz since the subtraction of ε_∞ from ε leads to the relatively small values of χ'. Thus, a comparison between the real and imaginary parts of the complex electric susceptibility in this part of spectra will not be conducted and certain information regarding the polarization mechanisms at this part of spectra will be lost.

In the figures of electric susceptibility illustrated in this work, the markers correspond to the average values and the lines of best fit are shown for each segment as solid lines. The lines of best fit represent the power-law behavior ($\sim \omega^n$) of the dielectric response. The slopes of the fitting lines ($\lg \chi' / \lg \omega$ or $\lg \chi'' / \lg \omega$) and the frequency of a transition between two distinguishable slopes (f_c) are identified.

A linear regression model (the method of the least squares as implemented in *Matlab*)

was employed to determine the slopes and corresponding transition frequencies. The coefficient of determination, R^2, was used to assess the linear regression and to detect the transition frequency (f_c). Figure 5.1 gives an example of the application of such approach for χ''. Here red and blue crosses represent R^2 of the linear approximations from this marker to 10^4 Hz (red cross) and from 10^{-4} Hz to this marker (blue cross). To quantify the transition, $R^2 = 0.98$ was chosen to distinguish the regions with different slopes, the frequency of a transition between two distinguishable slopes (f_c) corresponds to the frequency (from the data points) located between the transition points. In this example the transition frequency is 4 mHz. It is assumed that two slopes are not distinguishable if the absolute difference is less than 0.1 that is a mathematical choice in this work. When several segments are determined; the subscript is used to denote different slopes. The absence of the subscript means that only one slope was detected.

The method to analyze the dielectric response employed in this work is a simplified mathematical apparatus that is able to extract/define the dominant polarization mechanisms (if it exists). More sophisticated approach considers the individual mathematical models for each polarization mechanism and applies the nonlinear least-square fitting procedure to approximate the dielectric response [8]. Then the results of the fitting are used to evaluate the material degradation.

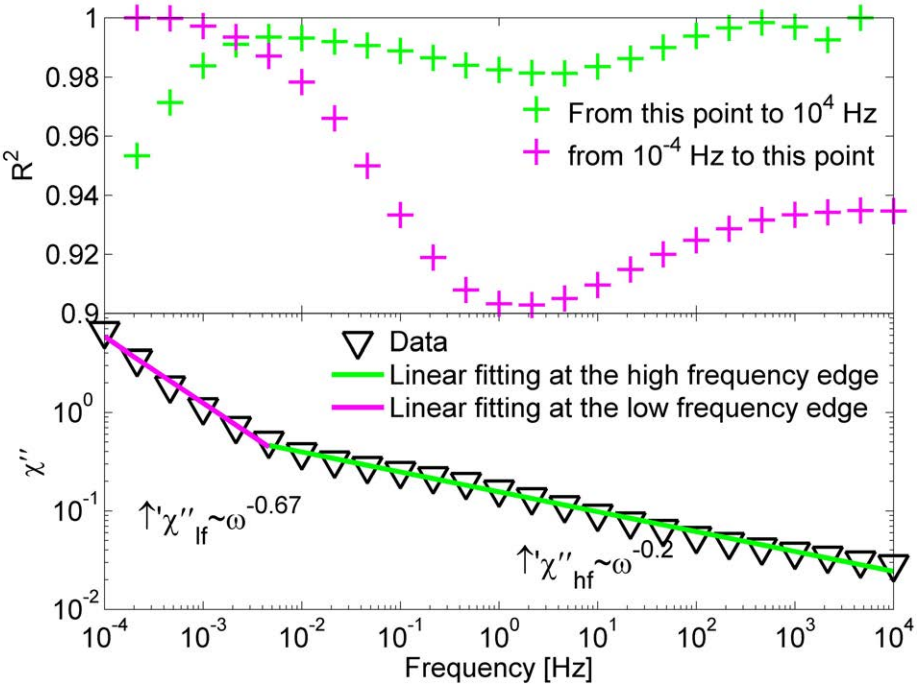

Figure 4.3. *Application of the linear regression model to determine the slopes and transition frequency.*

Chapter 5

Results and Discussion

In this chapter results from three case studies will be presented and discussed. The chapter begins by examining the sensitivity of the contact-free parallel plate method and establishes corresponding uncertainties in the measured values. Throughout this chapter each experimental set will contain the summary subsection that generalizes the trends attributed to the polymeric material under consideration in the particular experimental conditions. For the reason of space and the readability of the work,not all data/analysis are presented in the Chapter. The reader may find the results of certain measurements and post-processing in the Appendices B, C and D.

5.1 Application of Sensitivity Analysis

In this Section the sensitivity analysis of the measured ε' and $\tan\delta$ is performed according to the protocol developed in Section 4.6. The contributions from uncertainty in the electrical measurements, from uncertainty as result of setting $\varepsilon_{\text{air}} = 1$, from uncertainty associated with geometric correction factor are common for all measured samples. Within the measured ε' (2-5) and $\tan\delta$ (10^{-3}-10^{-1}) corresponding calculated uncertainties are summarized in Table 5.1.

Table 5.1. *Comparison of calculated relative uncertainties in* ε' *and* $\tan\delta$.

	$\frac{\lvert\Delta\{\cdots\}\rvert_{V_r}}{\{\cdots\}}$	$\frac{\lvert\Delta\{\cdots\}\rvert_{\varepsilon_{\text{air}}}}{\{\cdots\}}$	$\frac{\lvert\Delta\{\cdots\}\rvert_{k}}{\{\cdots\}}$
$\{\varepsilon'\} = 2\text{-}5$	0.004	0.001	0.1-0.3
$\{\tan\delta\} = 10^{-3}\text{-}10^{-1}$	0.2-0.6	–	0.1-0.3

Table 5.2. *Comparison of calculated relative uncertainties in* ε' *and* $\tan\delta$ *due to the spatial measurements.*

	d_1	Δd_1	$\frac{\lvert\Delta\varepsilon'\rvert_{d_1}}{\varepsilon'}$	$\frac{\lvert\Delta\varepsilon'\rvert_{d_2}}{\varepsilon'}$	$\frac{\lvert\Delta\tan\delta\rvert_{d_1}}{\tan\delta}$	$\frac{\lvert\Delta\tan\delta\rvert_{d_2}}{\tan\delta}$
EPDM	2.9	0.2	0.14-1.4	0.07-0.75	0.2-1.47	0.11-0.8
LSR	2.13	0.2	0.19-1.88	0.04-0.36	0.3-2.0	0.06-0.48
HTV	2.13	0.2	0.15-1.57	0.05-0.47	0.23-1.68	0.067-0.5
W12/W12 EST	4.5	0.2	0.08-0.91	0.02-0.24	0.13-0.95	0.04-0.26
FRP	4.6	0.2	0.09-0.87	0.02-0.24	0.13-0.93	0.04-0.26

An uncertainty in the spatial measurements depends on the the thickness variation of a particular sample (Table 4.3) and the uncertainty of the measured electrode separation. Table 5.2 presents calculated contributions to uncertainty due to the spatial measurements for the unaged samples used for water immersion ageing procedure. The comparison of Table 5.1 and Table 5.2 identifies that that the measurement accuracies of d_1 and d_2 are the critical parameters defining the accuracy of ε' and $\tan\delta$. The accuracy of the electrical measurements employed Solartron Analytical Modulab XM MTS is assumed to be acceptable (Table 5.1) otherwise a similar scrutiny is required.

5.2 Close-Contact and Contact-Free Arrangements

This section presents the experimental results of dielectric spectroscopy measurements by means of close-contact (both electrodes in full contact with the sample) and contact-free (lower electrode in contact with the sample, an air gap of known thickness between the sample and the upper electrode) parallel plate techniques (Figure 2.9). The Solartron

holder was used as the testing cell. Three specimens of each polymeric insulating material (EPDM, LSR, and HTV) were tested. The frequency-dependence of the complex dielectric permittivity, $\varepsilon = \varepsilon' - j\varepsilon''$, the complex electric susceptibility, $\chi = \chi' - j\chi''$, and the loss tangent, $\tan\delta$, were chosen to illustrate the dielectric response. For these log-log plots of the complex dielectric permittivity, a solid line represents average value of three measurements and the uncertainty bars correspond to the minimum and maximum values.

5.2.1 EPDM

The real and imaginary parts of complex dielectric permittivity and loss tangent of EPDM rubber over the measured frequency range using close-contact and contact-free parallel plate techniques are given in log-log representation in Figure 5.1. Dielectric responses obtained via the contact-free and close-contact techniques behave similarly: both are characterized by a substantial dispersion of either real or imaginary components of complex dielectric permittivity. However, the absolute values are slightly different: the highest observed values are for the close-contact technique. The values of ε' at higher frequencies, ε_∞, obtained using close-contact and contact-free parallel plate techniques are 3.3 and 3.5 respectively. It is assumed that all low-frequency polarization mechanisms (Section 2.7) are ceased at 10^4 Hz. Therefore, the slight difference is accounted for the inaccuracy of the measuring method (Section 4.6).

Converting the complex dielectric permittivity to the electric susceptibility indicates that the dielectric responses in Figure 5.2 are characterized by two clearly separate processes. the principal feature of the LFD (low frequency dispersion, Section 2.7) process is suggested by the parallelism of the curves representing $\chi = \chi'$ and χ''. In contrast, in frequency range from 10^{-4} Hz to 10^{-2} Hz corresponding slopes of $\chi = \chi'$ and χ'' are not parallel and only the slopes of χ' coincides for both measuring techniques. The close-contact technique introduces DC conductivity to the losses. Thus, the slopes of χ'' in the given frequency

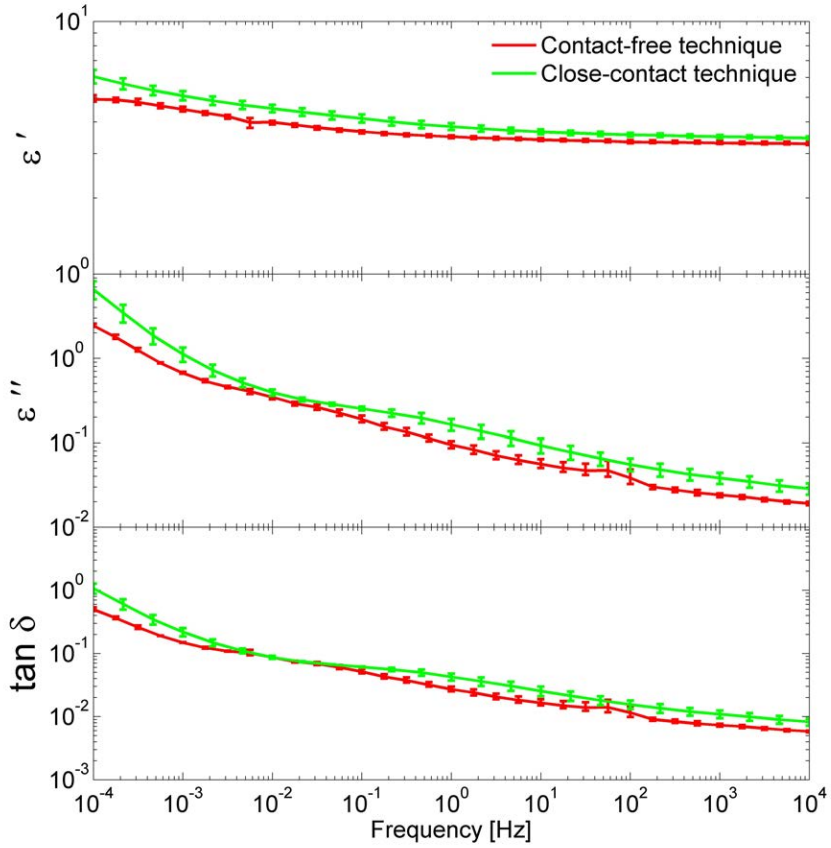

Figure 5.1. *Log-log plot of the real and imaginary parts of the complex dielectric permittivity and the loss tangent of EPDM measured by means of close-contact and contact-free parallel plate technique employing the Solartron holder.*

range obtained using the contact-free and close-contact techniques are different. The DC conduction mechanism is not the only dominant loss mechanism here since the slope is not proportional to -1 (Section 2.7). The reason of the change in the slope at 10^{-2} Hz in case of the contact-free technique is unclear but may be associated with presence of the additives in the formulation of EPDM [56] that modify the dielectric response.

The parallelism of lines approximating χ' (Figure 5.2) measured using close-contact and contact-free techniques indicates the similar polarization mechanisms and, thus, the contri-

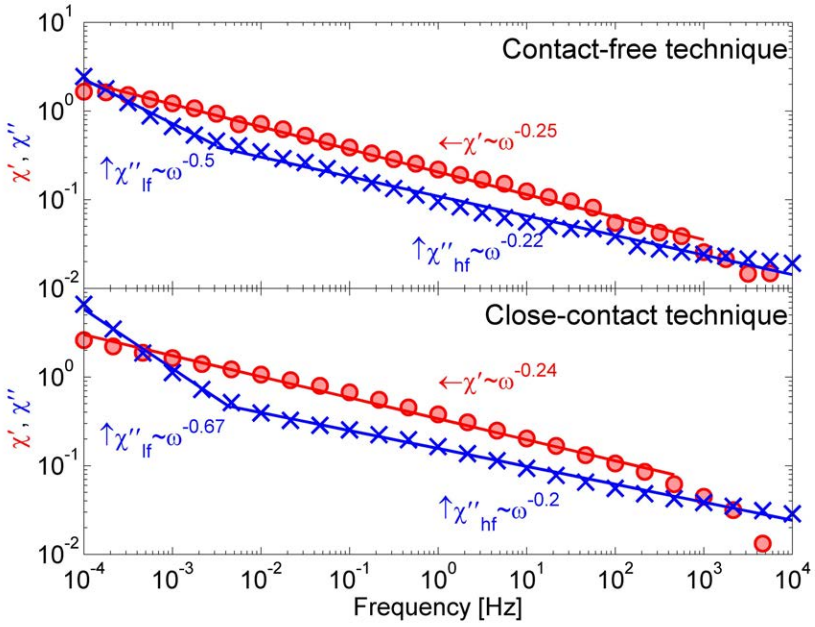

Figure 5.2. *The electric susceptibility of EPDM rubber measured by means of the close-contact and contact-free parallel plate technique employing the Solartron holder (the red colour corresponds to the real part of the electric susceptibility and the blue colour corresponds to the imaginary part of the electric susceptibility).*

bution of a macroscopic Maxwell-Wagner polarization, that occurs at the interface between the sample and remaining air in case of contact-free technique, to the total polarization is negligible.

The presence of LFD processes suggests that unaged EPDM is not an ideally homogeneous media. It contains some "defects" that attract low-mobility charge carriers, whether electronic or ionic, contributing to the total polarization.

5.2.2 LSR and HTV

The dielectric responses of LSR and HTV rubbers obtained using the close-contact and the contact-free parallel plate techniques are similar to the EPDM rubber. Corresponding

figures can be found in the Appendix B.

5.2.3 Summary and Comparison

The results show negligible with experimental accuracy difference between the close-contact and the contact-free measurements of the complex dielectric permittivity except the low-frequency range where arising DC conductivity contributes to ε'' in case of close-contact technique. The real and imaginary parts of the complex dielectric permittivity and loss tangent of these polymeric materials increase at lower frequencies since space charge polarization and interfacial polarization mechanisms are activated at lower frequencies (Section 2.6). The variation observed is consistent with the results of other collaborators in the *CIGRÉ working group D1.59* [65].

Having the dielectric response in the form of the real and imaginary parts of the electric susceptibility of the materials under test enables us to study not the particular value but the dynamic of the dispersion examining corresponding slopes of χ' and χ''. The analysis did not identify any significant difference between χ' and χ'' obtained using two measuring technique except the low frequency range where DC conductivity contributes to χ'' measured employing close-contact method. We may conclude that the contribution from the air/sample interface (contact-free method) to the net polarization is negligible. It also appears that pure Debye behaviour (Section 2.7) does not provide a complete description for the spectra obtained from these polymeric samples. However, a fractional power law with certain contributions from LFD (Section 2.7) appears to provide a complete description of the spectra.

5.3 Water Immersion Ageing

Absorption of water in the polymeric insulating material in combination with the electrical stress under the operation can lead to the deterioration of dielectric character. Therefore,

Table 5.3. *The key steps in the water immersion ageing procedure.*

#	Step	Name of the dielectric spectroscopy test performed after this step
1	Unaged sample	S1
4	Drying at 100°C for 6 hours	S2
8	Water immersion for 50 days	S3
15	Drying at 100°C for 96 hours	S4

the study of the penetration of water in the dielectric structure deserves special consideration. This section deals with the results of water immersion tests performed according to the testing scheme reported in Section 4.4. The whole water immersion ageing procedure may be divided into two significant stages: ageing due to the immersion in distilled water and following recovery in air at 100 °C. The key steps of this procedure are reflected in Table 5.3 and they will be used for further discussion. To examine the variation of the dielectric spectra of the aged samples, the replicate measurements were carried out after three weeks storing at ambient conditions. This test will be denoted as "S4 (3 weeks)".

The dielectric spectroscopy measurements for this analysis were carried out by means of the contact-free parallel plate technique. The *CIGRÉ* holder was used as a testing cell. One specimen of each polymeric insulating material: EPDM, LSR, HTV, W12, W12 WST, FRP was tested. The graphs of the complex dielectric permittivity, $\varepsilon = \varepsilon' - j\varepsilon''$, the complex electric susceptibility, $\chi = \chi' - j\chi''$, and loss tangent, $\tan\delta$, versus frequency were chosen to show the dielectric response.

The variation of the sample mass during the test was defined as

$$\triangle m = \frac{m_s - m_0}{m_0}, \tag{5.1}$$

Table 5.4. *The steps in the heat treatment protocol.*

#	Step	Name of the dielectric spectroscopy test performed after this step
1	Unaged sample	D1
2	Drying at 100°C for 6 hours	D2
3	Drying at 100°C for 96 hours	D3

where m_s denotes the absolute mass of the sample after certain step of the water immersion ageing procedure and m_0 is the initial weight of the sample before the commencement of the ageing/immersion protocol. The value of $\triangle m$ taken in conjunction with a particular susceptibility response measurement can be found in the right top corner of the susceptibility plot. The raw weight measurements can be located in Appendix C.

To asses the influence of only drying on the dielectric properties of the polymeric materials, independent spectroscopic measurements of samples exposed only to the heat treatment steps of the water immersion ageing procedure(Table 5.3). Table 5.4 summarizes and denotes the steps when the dielectric response was measured.

Measurements of W12, W12 WST, and FRP samples were performed before the upgrade of the Solartron firmware (Appendix A) and, as a result, are not accurate in the frequency range from 10^{-4} to 10^{-3} Hz.

5.3.1 EPDM

Figure 5.3 shows the change in the dielectric response of EPDM material in terms of ε', ε'', and $\tan\delta$ from the "unaged" state to the "aged" state caused by the water uptake ageing procedure and subsequent drying. A comparison between the plots of the "Unaged" and "After water immersion for 50 days" indicates a slight increase in all parameters of dielectric response compared to the range of estimated uncertainty in ε', 0.21-2.15, and $\tan\delta$, 0.3-2.27,

for unaged EPDM sample (Table 5.2). In contrast, a drying after the water immersion led to a major decrease in all dielectric quantities.

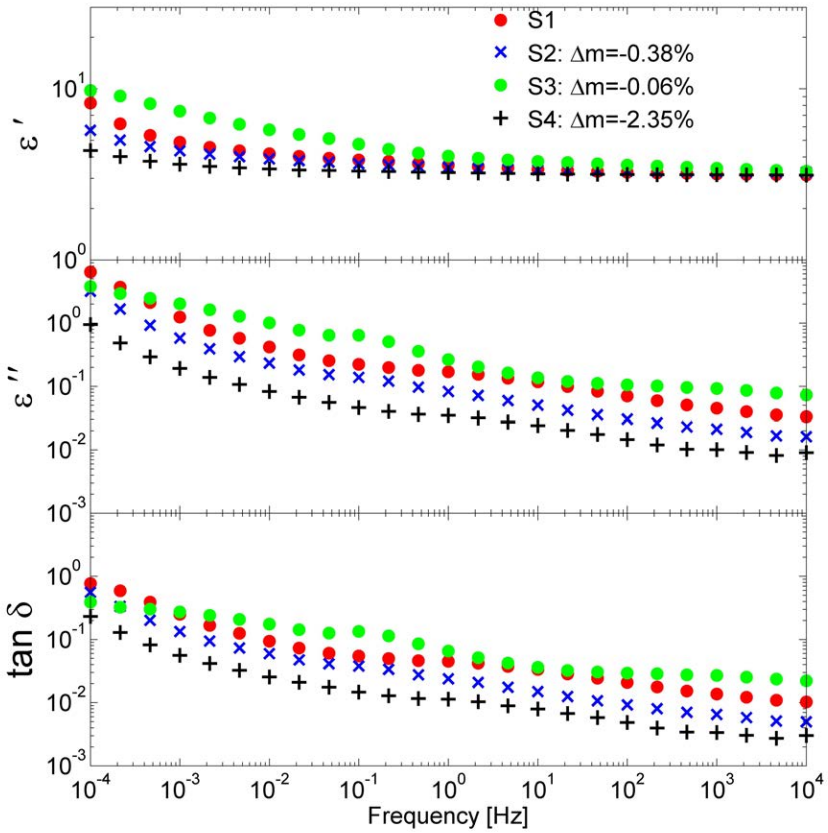

Figure 5.3. *The log-log plot of the real and imaginary parts of the complex dielectric permittivity and loss tangent of EPDM measured by means of the contact-free parallel plate technique employing the CIGRÉ holder during the water immersion ageing procedure (Table 5.3). The mass change associated with the step of the protocol is provided.*

The graph of the electric susceptibility (Figure 5.4) illustrates that the single slope of χ' appears unchanged during the ageing procedure. This means that the water uptake has shifted the profile of χ' of unaged sample towards the higher frequency. The number of distinguishable slopes of χ'' remained the same during the ageing procedure but the slopes and the transition frequency, at which the change from one slope to another occurs, has

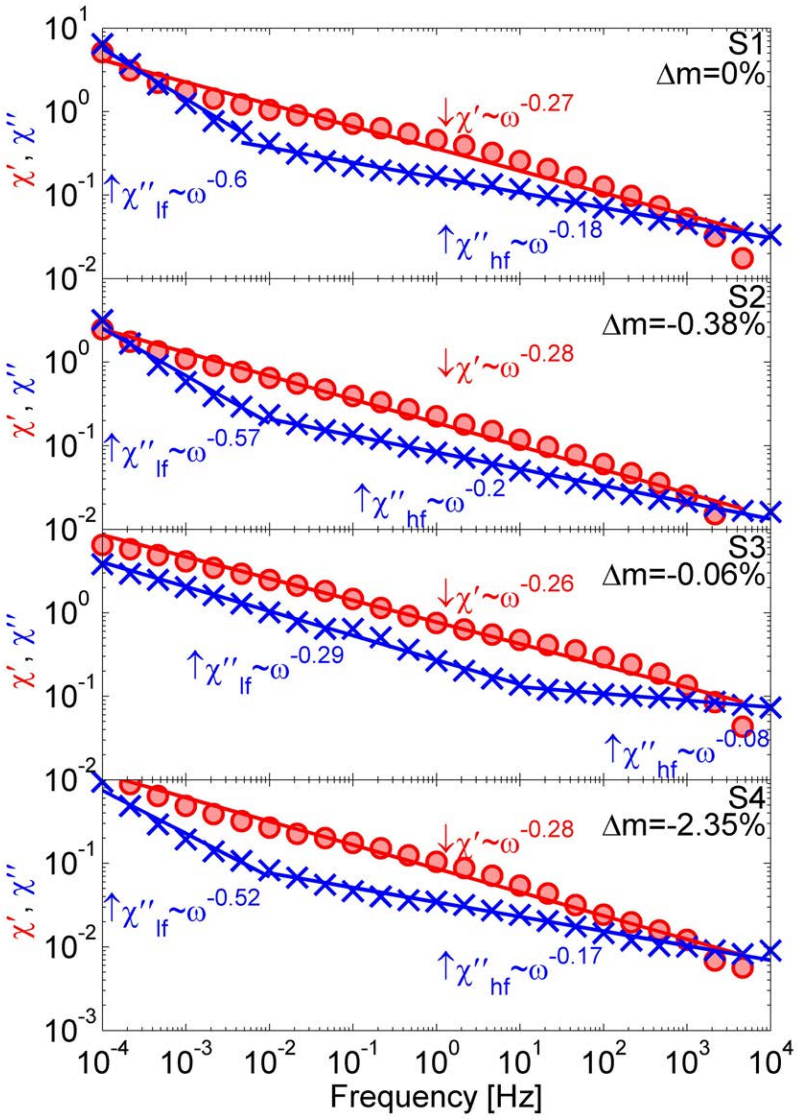

Figure 5.4. *The log-log plot of the electric susceptibility (red - χ' and blue - χ'') of EPDM measured by means of the contact-free parallel plate technique employing the CIGRÉ holder during the water immersion ageing (Table 5.3). The mass change associated with the step of the protocol is provided.*

changed after the water immersion and returned to original values after drying.

The weight of the EPDM sample initially decreased by 0.38 % after drying for 6 hours,

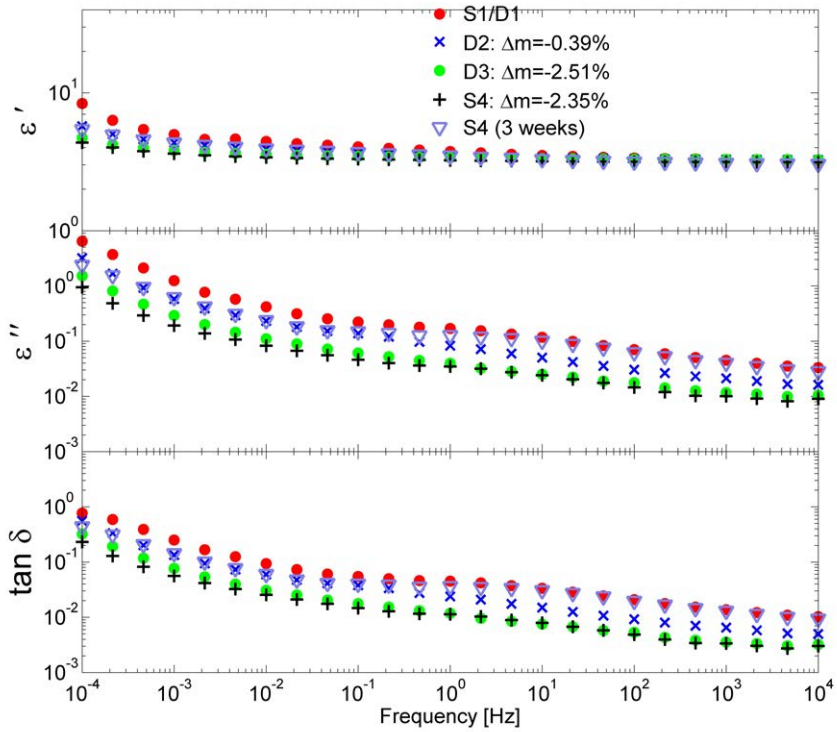

Figure 5.5. *Log-log plot of the real and imaginary parts of the complex dielectric permittivity and the loss tangent of the EPDM samples (after the whole water immersion ageing procedure, Table 5.3, and after just its drying part, Table 5.4) measured by means of the contact-free parallel plate technique employing the CIGRÉ holder*

then it almost recovered to the original value (in fact, 0.06 % less than original mass) after 50 days in distilled water. Furthermore, after 96 hours of drying in air at 100°C the sample lost 2.35 % of its original mass. It can be reasonably assumed that the weight loss following the 96 hours of drying at 100 °C was due to evaporation of water that had been taken up by the EPDM sample during immersion. To examine this hypothesis, a new EPDM sample tested according to the protocol described in Table 5.4. The comparison of the dielectric responses after the whole water immersion ageing procedure (step *S4* in Table 5.3), after only heat treatment (steps *D1-D3* in Table 5.4) and after the storing of the water immersion aged sample in the ambient conditions for three weeks (step *S4* (3 weeks)) is performed in

Figure 5.5. The heat treatment protocol (Table 5.4) and the whole water immersion ageing protocol (Table 5.3) led to the same (compared to the degree of uncertainty in the contact-free parallel plate method, Table 5.2) dielectric response of EPDM. After the both protocols the sample lost the same portion of its mass: 2.35 % in case of the water immersion ageing procedure and 2.51 % in case of the heat treatment protocol respectively. Therefore, the post-immersion drying resulted in the loss of the mass not associated with the evaporation of the absorbed water. The replicate measurement of the aged sample revealed that the dielectric response have not been stabilized and 96 hours drying step in the protocol (step *S4* in Table 5.3) did not remove the moisture accumulated in the sample.

5.3.2 LSR

The frequency responses of the LSR sample during the water immersion ageing procedure are shown in Figure 5.6 and in Appendix D. All parameters of the dielectric response increased after the water immersion but the post-immersion drying returned the dielectric response to its original values except for the frequency range from 10^{-4} to 10^{-3} Hz. The increase of the dielectric response after the water uptake is considered to be significant based on the comparison with the range of estimated uncertainty in ε', 0.23-2.24, and $\tan\delta$, 0.36-2.48, for unaged LSR sample (Table 5.2). On the other hand, the dielectric parameters after the post-immersion drying need to be interpreted with caution since the changes are within the experimental uncertainty.

First, after the pre-immersion drying the mass of the sample reduced by 0.14 %, then it decreased by extra 0.11 % after immersion. Finally, the post-immersion drying in air at 100 °C led to the mass less than the original value by 1.24 %. The origin of this transformation was checked using only the result of only heat treatment protocol (Table 5.4. The dielectric response (Figure 5.7) did not exhibit the difference (less significant than the experimental error, Table 5.2) between the samples aged in different environments. Although the weight

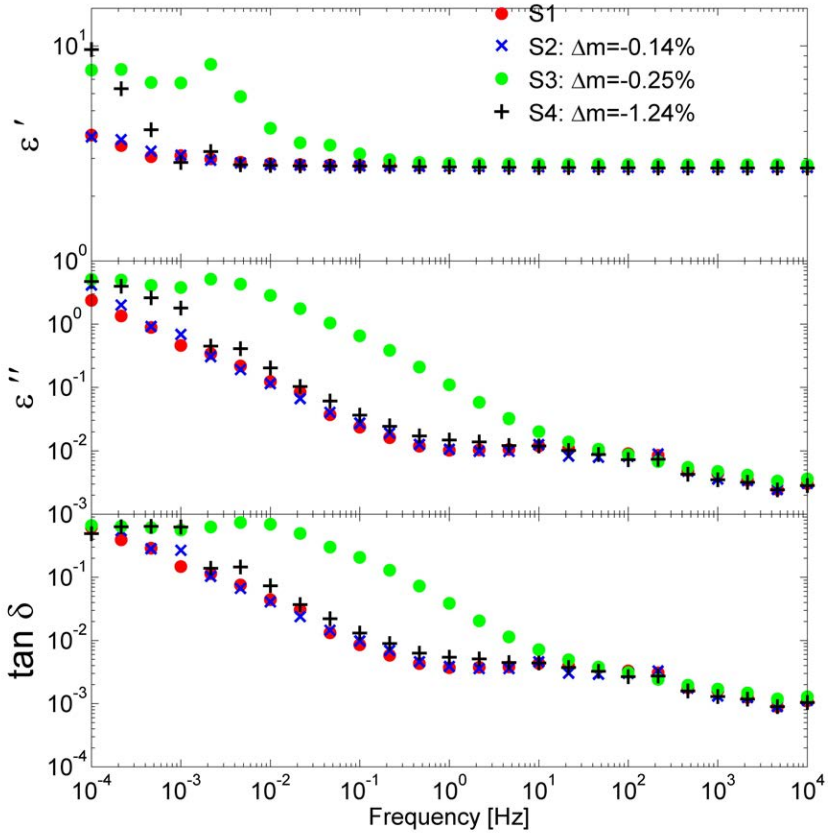

Figure 5.6. *The log-log plot of the real and imaginary parts of the complex dielectric permittivity and the loss tangent of LSR measured by means of the contact-free parallel plate technique employing the CIGRÉ holder during the water immersion ageing procedure (Table 5.3). The mass change associated with the step of the protocol is provided.*

of the sample exposed to the heat treatment protocol (Table 5.4) was reduced by 0.58 % that was less than in case the immersion protocol (Table 5.3). Hence, the post-immersion drying indeed led to the evaporation of water from the sample. It is important to note that a replicate measurement (three weeks after) of the aged sample (Table 5.3) showed slightly different dielectric response compared to one conducted earlier. However, the difference is within the experimental error.

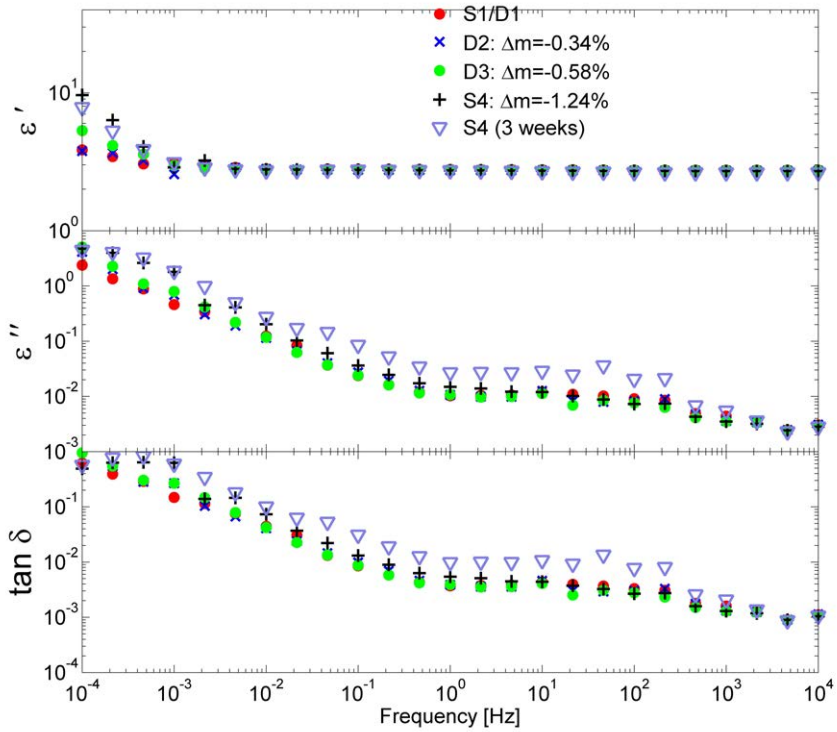

Figure 5.7. *Log-log plot of the real and imaginary parts of the complex dielectric permittivity and the loss tangent of the LSR samples (after the whole water immersion ageing procedure, Table 5.3, and after just its drying part, Table 5.4) measured by means of the contact-free parallel plate technique employing the CIGRÉ holder*

5.3.3 HTV

The frequency response characteristics of the HTV rubber sample obtained during the combined water immersion ageing procedure are given in Figure 5.8 (the plot of the electric susceptibility can be find in the Appendix D). The dielectric parameters of HTV rubber were affected by the absorbed water: there is a rise of all dielectric parapeters over the measured frequency range. While the post-immersion drying facilitated the restoration of the dielectric spectra to the unaged state over the frequency range from 1 Hz to 10^4 Hz, the dielectric response over the frequency range from 10^{-4} Hz to 1 Hz did not coincide with

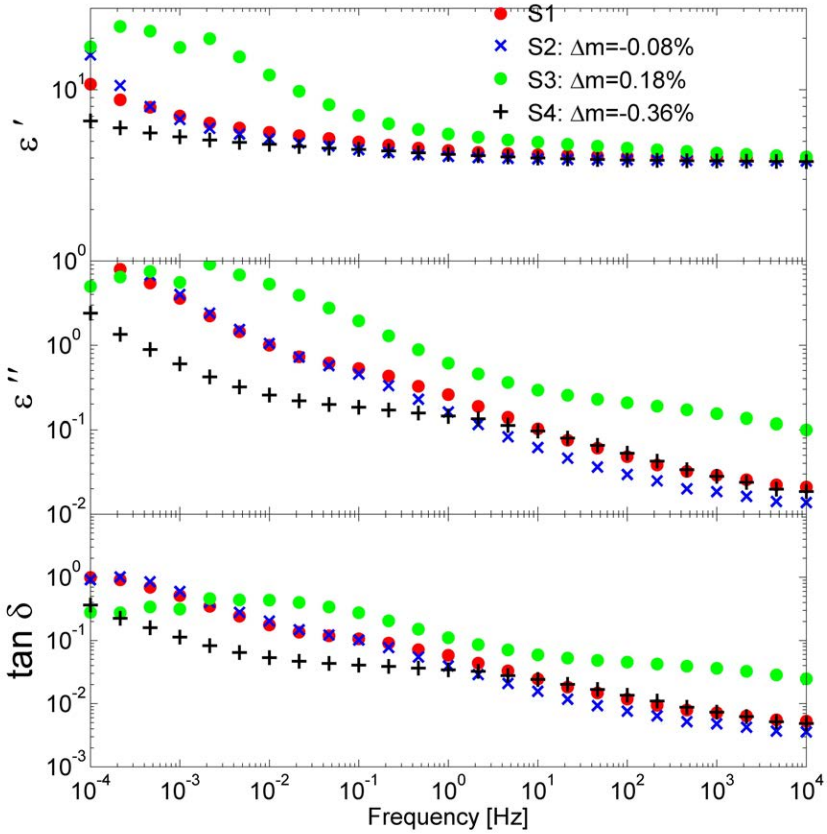

Figure 5.8. *The log-log plot of the real and imaginary parts of the complex dielectric permittivity and the loss tangent of HTV measured by means of the contact-free parallel plate technique employing the CIGRÉ holder during the water immersion ageing procedure (Table 5.3). The mass change associated with the step of the protocol is provided.*

one before the ageing.

The mass of the HTV sample initially reduced by 0.08 % after the pre-immersion drying, then it increased by 0.18 % after immersion and decreased again by 0.36 % after the post-immersion drying. As in the earlier discussion, the origin of the mass change after immersion is uncertain. It may be associated either with the evaporation of the absorbed moisture or solely with the drying effect on the HTV material. The HTV sample after the

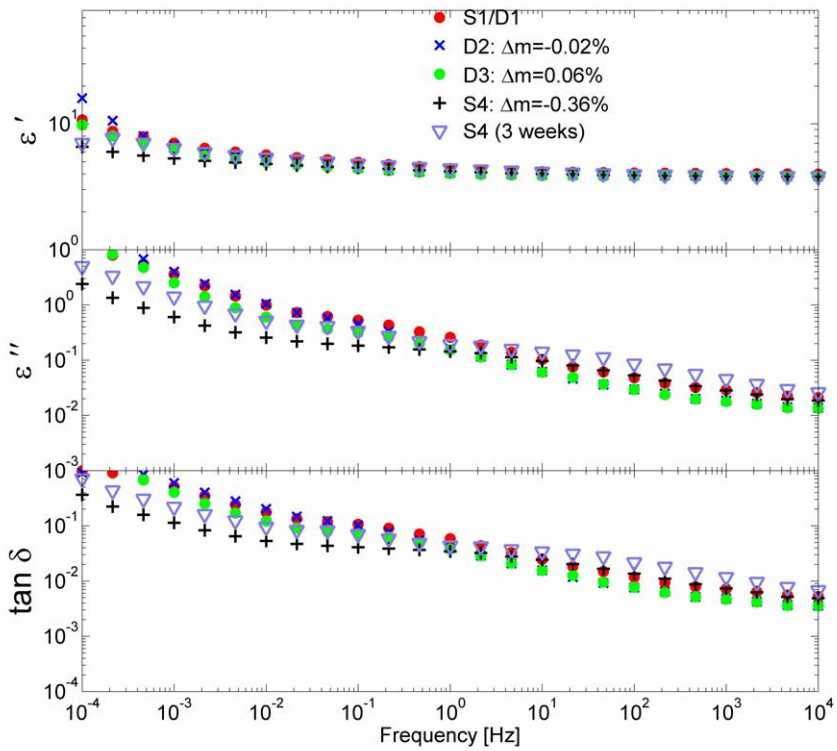

Figure 5.9. *Log-log plot of the real and imaginary parts of the complex dielectric permittivity and loss tangent of the HTV samples (after the whole water immersion ageing procedure, Table 5.3, and after just its drying part, Table 5.4) measured by means of the contact-free parallel plate technique employing the CIGRÉ holder*

only heat treatment (Table 5.4) did not display the transformation of the spectra and the weight remained the same (Figure 5.9). In contrast, the water uptake by the HTV sample has changed its dielectric spectra that did not return to the original view even after drying and kept changing after storing at the ambient conditions.

5.3.4 W12

The dielectric response and corresponding mass transformation of the W12 sample during the immersion are summarized in Figure 5.10 (the plot of the electric susceptibility can be find in the Appendix D). The water uptake led to the increase of dielectric parameters and

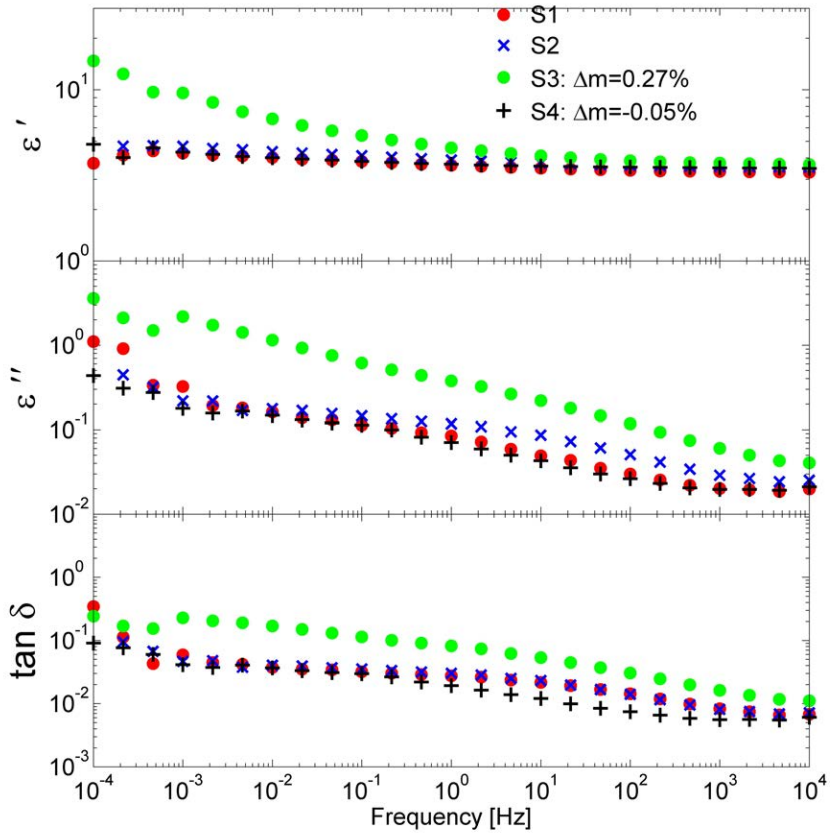

Figure 5.10. *The log-log plot of the real and imaginary parts of the complex dielectric permittivity and the loss tangent of W12 measured by means of the contact-free parallel plate technique employing the CIGRÉ holder during the water immersion ageing procedure (Table 5.3). The mass change associated with the step of the protocol is provided.*

the weigh gain by 0.27 %. A drying performed afterwards facilitated the recovery of the original spectra and returned the weight of the sample to its initial value.

5.3.5 W12 EST

The dielectric parameters of the W12 EST sample during the water immersion ageing procedure are shown in Figure 5.11 (the plot of the electric susceptibility can be find in

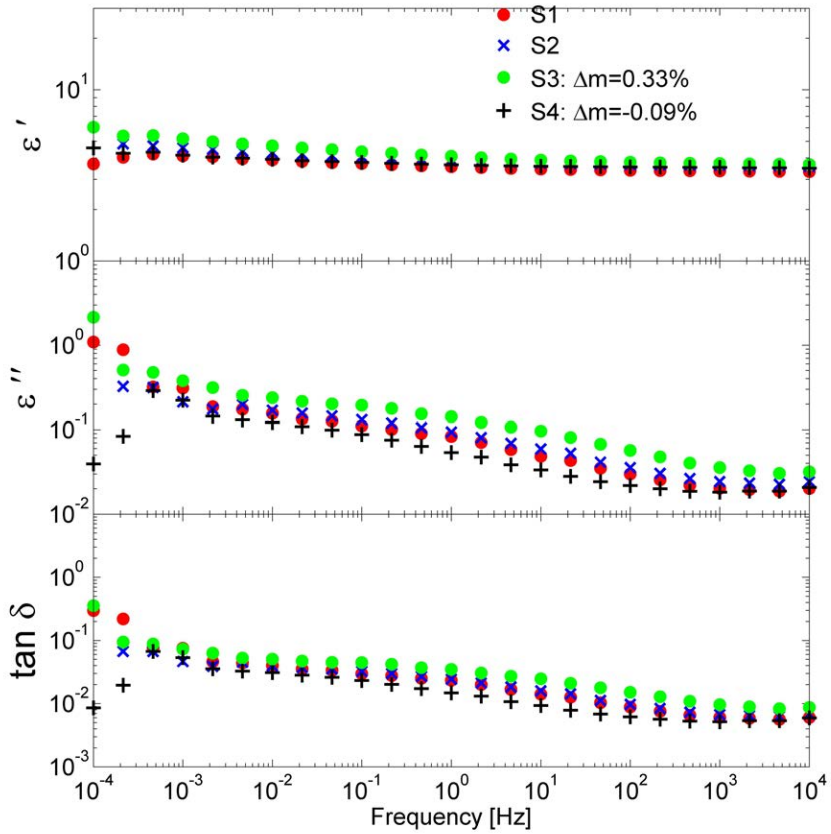

Figure 5.11. *The log-log plot of the real and imaginary parts of the complex dielectric permittivity and the loss tangent of W12 EST measured by means of the contact-free parallel plate technique employing the CIGRÉ holder during the water immersion ageing procedure (Table 5.3). The mass change associated with the step of the protocol is provided.*

the Appendix D). The dielectric spectra remained unchanged and the weight of the sample rose by 0.33 % after the water uptake. The post-immersion drying led to the decrease of the weight and it appeared to be 0.09 % less the original value.

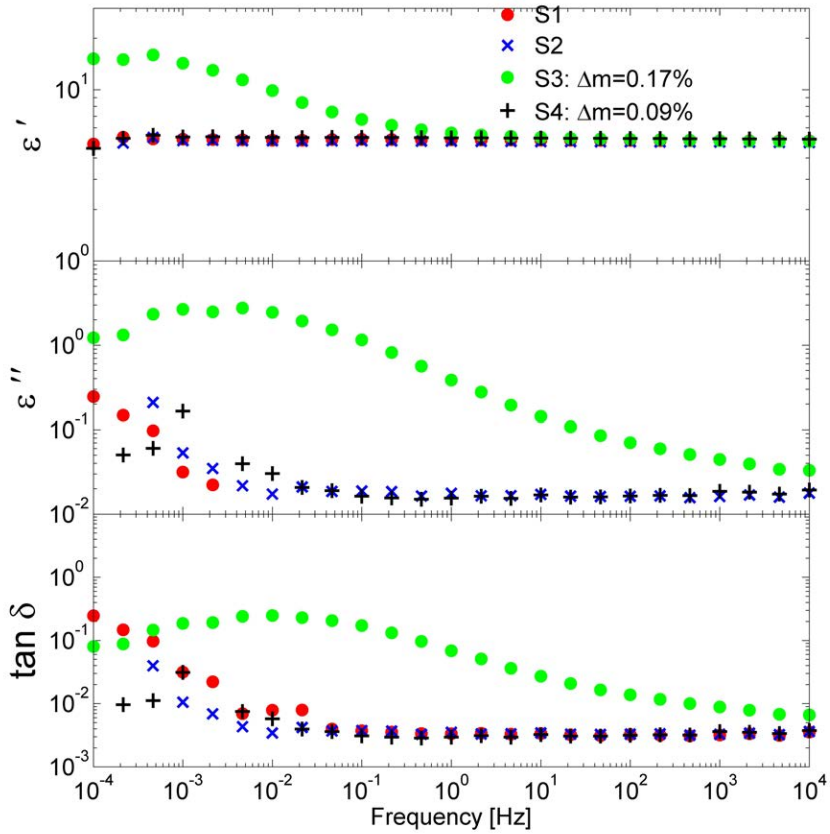

Figure 5.12. *The log-log plot of the real and imaginary parts of the complex dielectric permittivity and the loss tangent of FRP measured by means of the contact-free parallel plate technique employing the CIGRÉ holder during the water immersion ageing procedure (Table 5.3). The mass change associated with the step of the protocol is provided.*

5.3.6 FRP

The dielectric response of the FRP sample during the immersion is illustrated in Figure 5.12 (the plot of the electric susceptibility can be find in the Appendix D). The water uptake led to the increase of dielectric parameters and the weight gain (by 0.17 %). The post-immersion drying led to the recovery of the initial spectra.

After the initial drying for 6 hours at 100 °C the surface of FRP appeared to be covered

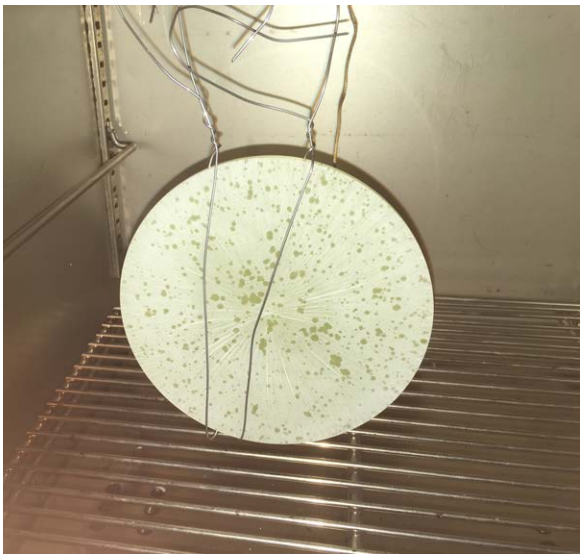

Figure 5.13. *The FRP sample after 6 hours drying at 100 °C.*

with spots (Figure 5.13). The change of colour is not a unique feature of the FRP sample and is a well-known marker indicating that chemical reactions have taken place inside the polymeric material [13] leading to the degraded performance.

5.3.7 Summary of the Water Immersion Ageing Procedure

The dielectric response of polymeric materials of different compositions reveals that all materials exhibit common elements and features after the water immersion ageing procedure. First, the dielectric spectra, both ε' and ε'', is affected by the absorbed moisture or by diffusion of the material into the water [16]. The influence can be strong (the changes are more than the level of uncertainty of the contact-free parallel plate method estimated in Table 5.2) like in case of LSR, HTV, W12, and FRP or weak (the changes are less than the level of uncertainty of the contact-free parallel plate method illustrated in Table 5.2) like in case of EPDM and W12 EST. Second, ε' at the high frequency edge of the considered frequency window (10^4 Hz) did not change (within the experimental uncertainty)

for all polymeric materials under investigation after any stage of water immersion ageing procedure, either actual immersion or following drying. This finding also supports the idea of the measurement at one particular frequency [11]. In contrast, ε'' at 10^4 Hz for certain polymeric materials increased (compared to the uncertainty range) after the water uptake since the increase in conductivity can be attributed to the absorption of humidity [66].

Possessing an extremely hydrophobic surface [16], the dielectric spectra of the LSR material has changed significantly (compared to the uncertainty range) after the water uptake (Figure 5.6). The possible explanation of such transformations is the interaction of water with the low molecular weight (LMW) fluid that is part of silicone rubber. LMW is built of PDMS having different chain lengths and structures. LSR material usually contains about 5% LMW [16]. Permanent hydrophobicity of LSR is provided by constant transfer of LMW out of the bulk of silicone to its surface. However, the transfer will be interrupted if the surface has a continuously wet pollution layer [16]. At the same time water may penetrate in the sample and initiate the dissolution of the low molecular weight fluid from the rubber bulk to the surrounding water [67]. This can be seen from the results of ageing: the sample past the immersion test (Table 5.3) has lost twice more of its weight compared to the sample past only heat treatment (Table 5.4). Considering the fact that after the immersion the sample also lost its weight, the LMW/water substitution may be accepted as the consistent hypothesis.

The effect of the moisture uptake on the EPDM rubber is less intensive (within the experimental error) compared to the LSR material (Figure 5.3). The reason for this is the absence of fillers and negligible amount of LMW [16]. The weight loss after the heat treatment was not attributed to the water absorption since almost the same weight loss was measured only after drying of a new EPDM sample. The loss of mass after the uniform temperature ageing may be linked with the evaporation of oil used as a plasticizer in the formulation of EPDM [68]. This suggestion also correlates with the finding that a dielectric

spectra of the sample after the whole water immersion ageing procedure and one of the sample exposed only to drying (Figure 5.5) are almost identical. Although the consequence of water absorption was not pronounced, the effect of humidity on EPDM resin is very significant. Figure 5.5 shows some results for various hydrations. It can be seen that there is a clear trend of increasing ε'' with humidity albeit the actual hydration levels were not identified.

Being composite insulating materials, W12, W12 EST and FRP, are susceptible to ageing due to the water absorption [16]. The ageing occurs in the region between glass particles (fibres) and the polymer host matrix (epoxy resin in case of W12, W12 EST and FRP). It is also believed that the influence of the water uptake on the neat epoxy resin (diffusible hydrophobic low molecular weight almost does not exist) is negligible in comparison with its influence on the interphase region. The growth of ε'' (Figure 5.10 and Figure 5.12 is associated with the increase of free charge carriers due to the ion exchange between water and the impurities in industrial quartz powder or fibre glass [69] that takes place at the interface. Moreover, the penetration of water into the glass material is also possible [69]. This process leads to the formation of the gel phase, the early stage of the hydrolysis or silica corrosion process, and results in the development of the nanocracks and the loss of internal adhesion [70]. The latter intensifies the space-charge polarization formed at the defects that manifests as the increase of ε' (Figure 5.10 and Figure 5.12). In contrast, W12 EST epoxy composite showed the resistance to water attack: the dielectric spectra almost remained unchanged after 50-days water immersion as can be seen from Figure 5.11. This significant improvement is possible because of the special filler surface treatments that enhance the chemical and physical bonding strength in the interphase [71]. Apart from transformation of the dielectric response, the water uptake is also confirmed by the weight gain. The subsequent heat treatment of the epoxy composite samples facilitated the recovery of the dielectric spectra to the original shape.

HTV rubber is another example of the composite material that is sensitive to the water uptake (Figure 5.8). Its filler, ATH, is a non-reinforcing filler that is poorly attached to the resin [14]. As a result, in the presence of water a strong hydrolysis results in the generation of free charge carriers and the degradation of the interface. The former increases ε'' and the latter amplifies ε' by means of Maxwell-Wagner interfacial polarization (Section 2.7). Additionally, observed variation in the mass is completely associated with the water uptake and its influence on polymer.

The analysis of slopes revealed that pure Debye relaxation was hardly identified even after the water uptake. In contrast, the low-frequency dispersion polarization mechanism manifested in EPDM, LSR, W12 and FRP after the water immersion ageing. This process can be considered to be mainly caused by the ions formed in the bulk of dielectric due to the interaction with water.

The observed results bring into the question the protocol established by the *CIGRÉ Working Group D1.59*. First, prior to the water immersion the samples were dried in a oven only for 6 hours. According to our results, it is not enough to completely remove the moisture from the sample. It is reasonable to introduce additional condition to stop the initial drying: the absence of significant weight change. Second, the appearance of spots on the FRP material after 6 hours of drying raises concerns regarding the choice of heat treatment temperature. It should also depend on the type of the material. Finally, we should define our requirements to the heat treatment after the water uptake and the to the protocol for the comparison of the recovered spectra with the unaged one since we have observed that the dielectric spectra of aged samples still changes even three weeks after the completion of testing.

Table 5.5. *Relative change in the weight and thickness of aged under two different thermal environments samples relatively to its unaged values.*

	Room Temperature	Coolant temperature	T_{h1}	T_{h2}	T_{c1}	T_{c2}	ΔT
Mean	23.4	-11.5	100.4	94.4	-10.1	-7.1	105.8
St. dev.	0.6	0.5	3.3	3.2	0.6	0.8	3.22
Max	24.6	-10	105	100	-8.1	-4.9	110.9
Min	22.2	-13	92	85	-11.7	-8.6	96

5.4 Thermal Gradient Ageing

The comparison between the uniform temperature aged sample, thermal gradient aged sample and unaged sample is presented in this section.

The uniform temperature ageing was organized using a laboratory oven. The average temperature inside the oven, obtained from readings performed once a day during 25 days (600 hours), was about 99.4 °C with the standard deviation of 2.7 °C.

The ageing in the thermal gradient environment was performed by means of the thermal gradient ageing module. The average temperatures at the heating and cooling blocks, obtained monitoring temperature sensors twice a day during 25 days (600 hours) ageing procedure, are summarized in Table 5.5. The average value for the temperature drop across the 2.3 mm thick sample, which was defined as $\Delta T = 0.5(T_{h1} + T_{h2}) - 0.5(T_{c1} + T_{c2})$, was about 106 °C.

After thermal gradient ageing, the sample demonstrated a visible change of shape (Figure 5.14). The convex face of the sample corresponds to the hot side of the thermal gradient module. In contrast, the sample aged at the uniform temperature did not deform (shape remained the same).

The real and imaginary parts of the complex dielectric permittivity and the loss tangent of aged under two different thermal environments and new EPDM samples over the frequency range from 10^{-4} to 10^{4} Hz are depicted using log-log representation in Figure

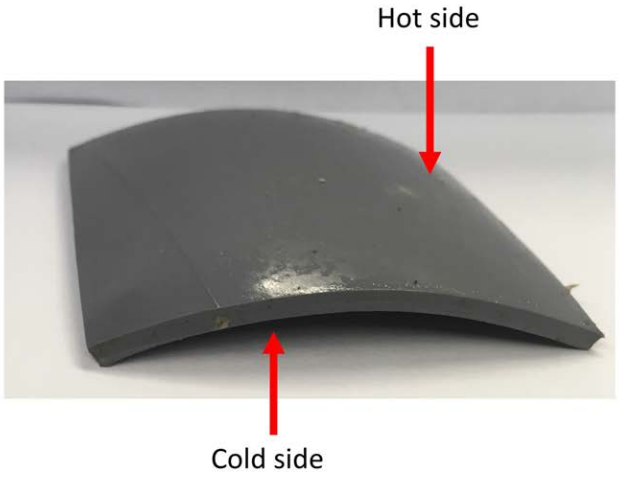

Figure 5.14. *Deformation of EPDM sample after 25 days thermal gradient ageing.*

5.15. After ageing in both environments, ε', ε'', and $\tan\delta$ decreased: this can be treated as a temporary improvement. The reason for this reduction is a moisture loss and possible activation of a cross-linking [72].

The analysis of corresponding slopes of χ' and χ'' did not identify any significant differences between aged in thermal gradient environment and unaged samples (Figure 5.16). In contrast, χ'' of the uniform temperature aged sample is described by three power laws. The transition to the prevalence of the DC conductivity (the slope is equal to -1) shifted from 10^{-2} Hz to 10^{-3}. The uniform temperature ageing also resulted in the appearance of the parallelism between the slopes of χ' and χ'' over the frequency range from 10^{-3} Hz to 10^{2} Hz. This process is associated with a polarization arising from the migration via the hopping process (LFD polarization process) between trapping spots [36]. Therefore, the uniform ageing has resulted in the formation of additional trapping spots since after ageing the LFD polarization process became dominant over the frequency range from 10^{-3} to 10^{2} Hz. These trapping spots are the evidence of cirtain changes in the material.

To attribute the decrease in ε', ε'', and $\tan\delta$ after either uniform temperature or ther-

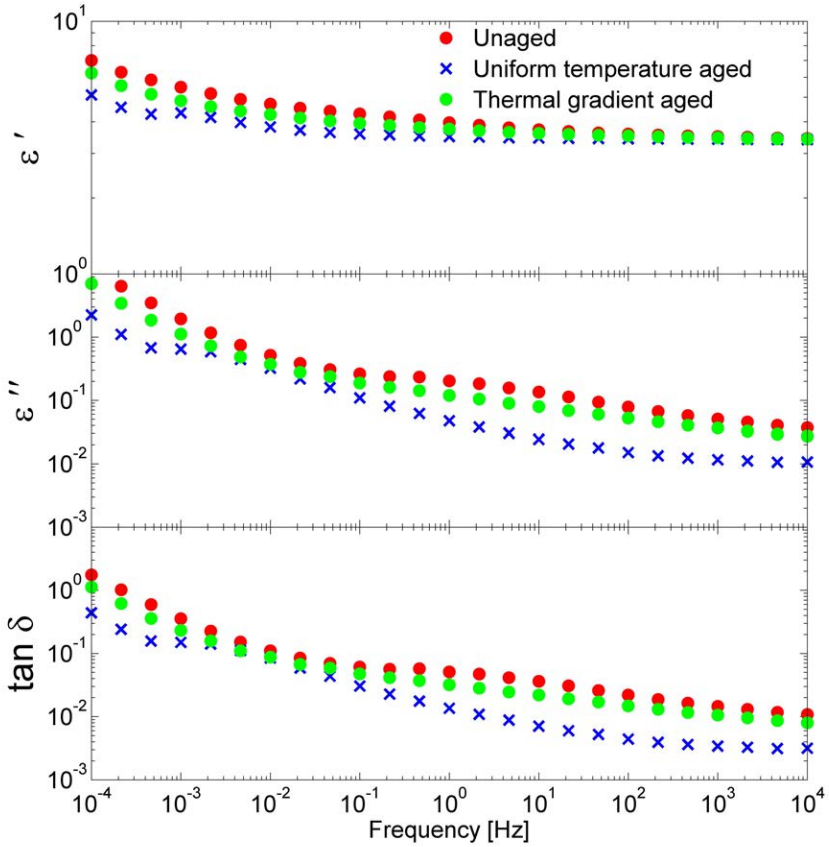

Figure 5.15. *The log-log plot of the complex dielectric permittivity and the loss tangent of aged under two different thermal environments and new EPDM samples.*

mal gradient temperature ageing to the evaporation of moisture, the replicate dielectric spectroscopy measurements of aged samples were performed after 2 months storing in the ambient conditions (Figure 5.17). The real and imaginary part of the complex dielectric permittivity and the loss tangent of the stored in ambient conditions samples increased and returned to the unaged values. However, the difference, that may be associated with the experimental error, is still pronounced over the frequency range from 10^{-4} Hz to 10^{-2} Hz and could be associated with the thermal ageing. The replicate weighting of the aged samples revealed 0.1 % mass increase of the uniform temperature aged sample (relatively to

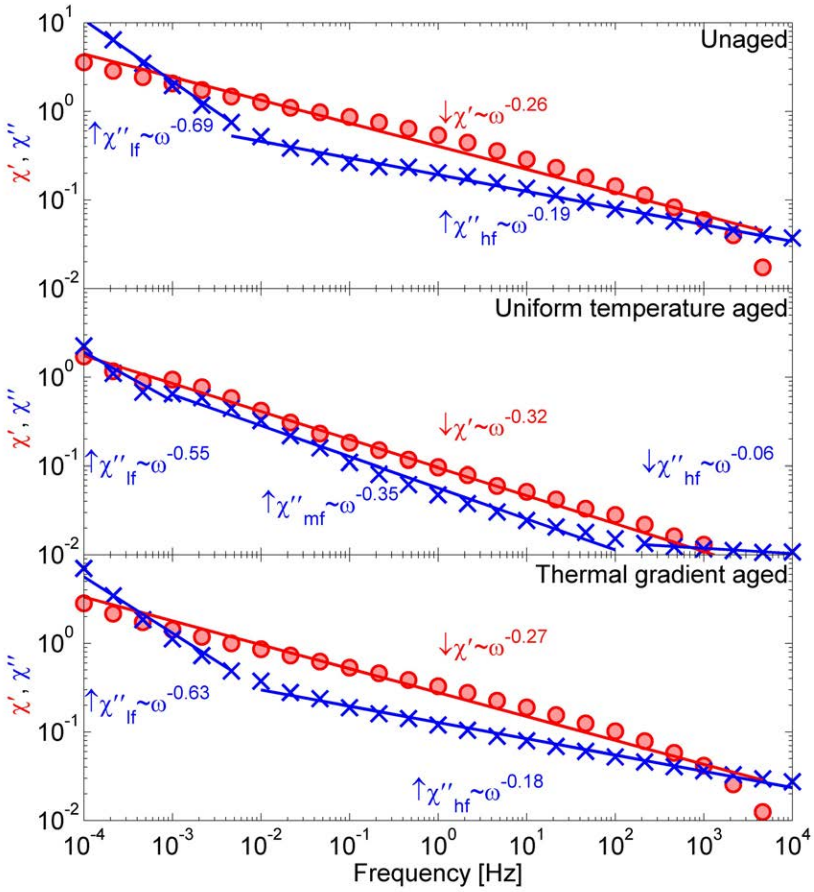

Figure 5.16. *The log-log plot of the complex electric susceptibility of aged under two different thermal environments and new EPDM samples.*

immediately after the ageing) and 0.3 % mass decrease of the thermal gradient aged sample (relatively to immediately after the ageing). Therefore, both ageing environments at tested temperatures and exposure times influence the moisture content in EPDM sample.

The mass and thickness of the samples were also recorded before and after the ageing. Table 5.6 shows the relative changes in mass and thickness of the aged samples relatively to its unaged values. After thermal gradient ageing the mass and the thickness have been slightly changed. However, the increment of the thickness was less than the relative variation

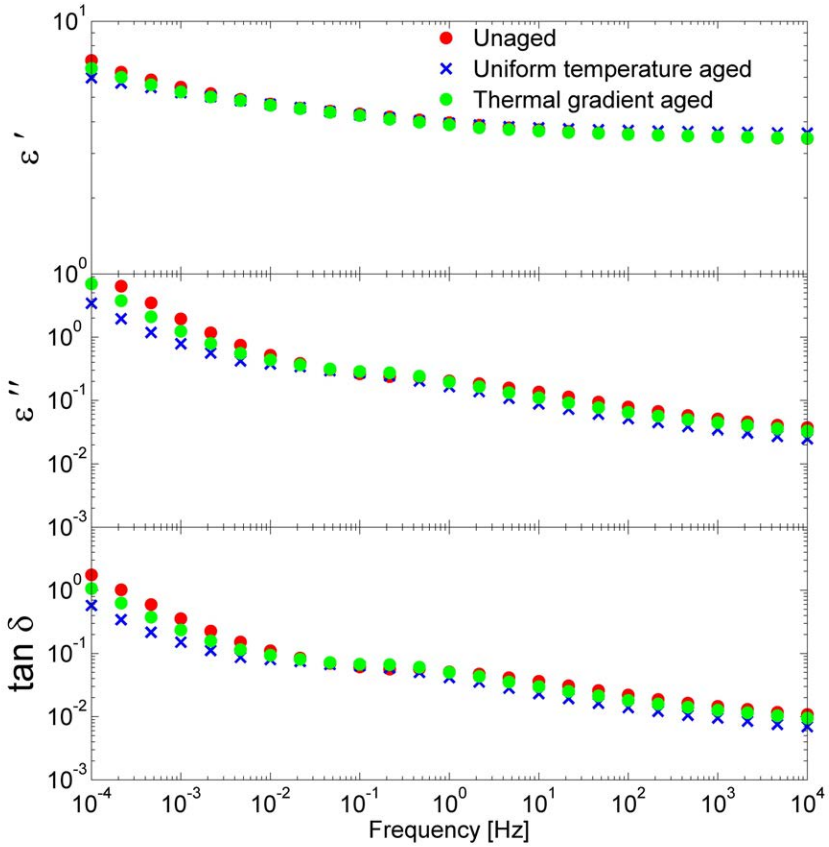

Figure 5.17. *The log-log plot of the complex dielectric permittivity and loss tangent of aged under two different thermal environments and new EPDM samples after 2 months storing under ambient conditions.*

of the thickness measured at different points of the unaged sample. Thus, it is likely that the thickness of the thermal gradient aged sample remained the same during testing. In contrast, the uniform aged sample lost 4 % of its mass and shrank across the thickness (longitudinal dimension). We were unable to investigate the correlation between the change in the longitudinal and transverse dimensions of the sample since transverse dimensions were not measured with required accuracy. The pronounced loss of mass after the uniform temperature ageing may be accounted for the evaporation of oil used as a plasticizer in the

Table 5.6. *Variation of the thickness and the mass of the EPDM sample after the ageing in two different thermal environments.*

	Relative change in the weight	Relative change in the thickness	Relative variation of the thickness
Thermal gradient aged sample	-0.8	-1.1	1.5
Uniform temperature aged sample	-4.5	-4.1	1.41

formulation of EPDM [68].

Our investigation so far revealed that both ageing environments impact the moisture content in the sample, that can restore (according to the measured dielectric spectra) after certain time keeping the aged sample at ambient conditions. Both ageing environments cause physical ageing of the material: deformation of the shape in case of thermal gradient ageing and weight loss and shrinkage in case of uniform ageing. Nonetheless, dielectric spectroscopy measurements did not reveal strong evidence of ageing after both thermal ageing techniques. Thus, at least at this point the comparison between two ageing environments is obstructed. Further data collection/investigation is required to determine exactly how two ageing environments are different.

Chapter 6

Conclusion

6.1 Dielectric spectroscopy characterization

The evolution of the standardized protocol, proposed by the *CIGRÉ Working Group D1.59*, for the dielectric spectroscopy characterization of HV insulating polymeric materials has been completed in this thesis. To assess the testing protocol, six types of polymeric insulating materials have been tested before and after water immersion ageing. We have proposed certain refinements to the this methodology and address some of its drawbacks. The analysis of the ageing due to the water uptake was also performed.

The dielectric spectroscopy routine tests favours the contact-free sample/electrode arrangement over the close-contact arrangement since, as discussed earlier, this arrangement avoids the issues of the sample deformation, vanishes the contribution from the DC conductivity and minimizes the impact of the contact resistance. The comparison of these two techniques were performed in this work by measuring LSR, HTV and EPDM rubber materials. The dielectric spectra, both ε' and ε'', was slightly larger when the close-contact arrangement was employed. If the increase in ε'' may be accounted for the DC conductivity, the reason of the increase in ε' is unclear. The analysis of slopes of χ' did not reveal the

difference. Another disadvantage of the contact-free method that we have tracked is the requirement of the flatness of the sample that sometimes is not the case after the ageing (Figure 5.14). Moreover, it is common practice to examine the complex dielectric permittivity as a function of temperature; at this conditions the remaining gap between the sample and the top electrode will be altered due to the thermal expansion (*e.g*, the EPDM sample will increase in thickness by ~ 0.03 mm at 70°C). This will lead to the error in the contact-free calculation as all spatial measurements are determined at room temperature.

A sensitivity analysis of the "contact-free method" considered the four key sources of uncertainty in the measurement of ε' and $\tan\delta$. The proposed methodology of the sensitivity estimation was tested using using an experimental set-up described in Figure 2.8 and the samples under the test. The measurement accuracies of the electrode separation and sample thickness mainly dominate the experimental uncertainties for the whole testing system. For the measurements performed in this work, these uncertainties reached the orders of the measured values of ε' and $\tan\delta$. These observations are confirmed by our collaborators within the round robin measurements [73].

The water uptake by polymeric insulating materials as an accelerating ageing technique was examined to assess the protocol for the dielectric spectroscopy characterization. The study showed that the water immersion ageing modifies the dielectric properties of the polymers under investigation. The scope for inference is limited by the lack of facile approach for corroborating/independently testing the phenomena involved (hydrolysis, delamination of the interfaces, diffusion of the material). Materials that did not contain fillers showed less significant increase in the dielectric parameters after the water uptake. Silicone rubbers are more susceptible to ageing due to the water uptake since their dielectric spectra has not recovered after the subsequent drying. The dielectric response revealed that a surface treatment of the filler enhances the resistance to the water immersion ageing. Moreover, the proposed ageing protocol is not ideal since it did not properly asses the impact of the

pre-immersion and post-immersion heat treatments. All these aspects should be taken into account in the further refinements of the dielectric spectroscopy assessment protocol.

6.2 Thermal gradient ageing

An apparatus for undertaking thermal gradient ageing studies of the polymeric materials has been designed and tested. The module applied a 105 °C temperature drop across the EPDM sample (with 2.3 mm thickness) that was stable during 25 days testing period. It allowed to pump the heat through the sample while keeping the temperature of the cold side of the thermal gradient at about -8°C and the temperature of the hot side of the thermal gradient at about 98°C respectively. However, the comparison based on the dielectric spectroscopy measurements between the sample aged in the uniform temperature environment and one aged in the presence of thermal gradient for 25 days did not indicate significant difference.

6.3 Future work

With the thermal gradient ageing module settled, future work should be concentrated on the analysis of the thermal gradient ageing. It is recommended that further research should be undertaken in the following directions:

- The development of the operational modes of the thermal gradient ageing module that will lead to the appearance of the ageing that can be detected by the dielectric spectroscopy measurements. This can be realized employing either larger temperature gradient across the sample or longer durations of the test.

- The investigation of other polymeric materials used in the insulation of HV elements, *e.g.* XLPE, that also experiences thermal gradient in the service and possesses enough accumulated experimental data on its performance after the uniform temperature

ageing to facilitate possible comparison. Besides, the current scrutiny of the XLPE material in the context of nanodielectrics [21] should address the presence of thermal gradient since the behavior of nanoparticles at this conditions may impact the physical and chemical properties of the whole material.

- The dielectric spectroscopy is a macroscopic electrical probing that does not locate and distinguish the ageing markers across the sample. It is expected that in the presence of the thermal gradient the distribution of the ageing artifacts will vary throughout the sample.To obtain a complete overview and to correlate degradation processes with the changes of physical/chemical properties across the the sample, it is desirable to use other ageing diagnostic techniques. The application of the space charge measurements [30] will allow to examine these transformations across the sample. Space charge dynamics properties in the bulk of the sample may reveal the differences between the samples aged in the thermal gradient and uniform temperature environments.

References

[1] X. Xu, T. Bengtsson, J. Blennow, and S. M. Gubanski, "Enhanced accuracy in dielectric response material characterization by air reference method," *IEEE Transactions on Dielectrics and Electrical Insulation*, vol. 20, no. 3, pp. 913–921, June 2013.

[2] L. Dissado and J. Fothergill, *Electrical degradation and breakdown in polymers.* Peter Peregrinus Ltd, 1992.

[3] J. S. T. Looms, *Insulators for high voltages.* The Institution of Engineering and Technology, 1987.

[4] J. Fothergill, "Ageing, space charge and nanodielectrics: Ten things we don't know about dielectrics," in *Proceedings of 2007 IEEE International Conference on Solid Dielectrics*, July 2007, pp. 1–10.

[5] S. Gubanski, "Modern outdoor insulation concerns and challenges," *IEEE Electrical Insulation Magazine*, vol. 21, no. 6, pp. 5–11, Nov. 2005.

[6] IEC, "IEC60216-1 electrical insulating materials thermal endurance properties. part 1: Ageing procedures and evaluation of test results," *IEC*, 2013.

[7] IEC, "IEC TR 62039-2007 selection guide for polymeric materials for outdoor use under hv stress," *IEC*, 2007.

[8] C. Yuan, C. Xie, L. Li, X. Xu, S. M. Gubanski, and Z. He, "Dielectric response characterization of in-service aged sheds of (u) hvdc silicone rubber composite insulators," *IEEE Transactions on Dielectrics and Electrical Insulation*, vol. 23, no. 3, pp. 1418–1425, June 2016.

[9] P. Werelius, P. Tharning, R. Eriksson, B. Holmgren, and U. Gafvert, "Dielectric spectroscopy for diagnosis of water tree deterioration in xlpe cables," *IEEE Transactions on Dielectrics and Electrical Insulation*, vol. 8, no. 1, pp. 27–42, March 2001.

[10] R. Liao, J. Hao, G. Chen, and L. Yang, "Quantitative analysis of ageing condition of oil-paper insulation by frequency domain spectroscopy," *IEEE Transactions on Dielectrics and Electrical Insulation*, vol. 19, no. 3, pp. 821–830, June 2012.

[11] W. Zaengl, "Dielectric spectroscopy in time and frequency domain for hv power equipment, part i: theoretical considerations," *IEEE Electrical Insulation Magazine*, vol. 19, no. 5, pp. 5–19, Sept.-Oct. 2003.

[12] W. S. Zaengl, "Applications of dielectric spectroscopy in time and frequency domain for hv power equipment," *IEEE Electrical Insulation Magazine*, vol. 19, no. 6, pp. 13–22, Nov.-Dec. 2003.

[13] T. Liu, J. Fothergill, S. Dodd, L. Dissado, U. H. Nilsson, M. Fu, and F. Perrot, "Dielectric spectroscopy study of thermally-aged extruded model power cables," in *Proceedings of the 10th IEEE International Conference on Solid Dielectrics*, July 2010.

[14] J. M. Seifert and H. C. Karner, "Dielectric diagnostic of moisture induced degradation processes in mineral reinforced high-voltage composite insulation," in *Proceedings of Conference on Electrical Insulation and Dielectric Phenomena (1996)*, Oct. 1996, pp. 825–828.

[15] J. Seifert, *Methods for dielectric characterisation of polymeric insulating materials for outdoor applications.* CIGRÉ, 2014.

[16] H. Janssen, J. M. Seifert, and H. C. Karner, "Interfacial phenomena in composite high voltage insulation," *IEEE Transactions on Dielectrics and Electrical Insulation*, vol. 6, no. 5, pp. 651–659, Oct. 1999.

[17] K. Mathes, "A brief history of development in electrical insulation," in *Proceedings of the 20th Electrical Electronics Insulation Conference*, Oct. 1991, pp. 147–150.

[18] G. C. Stone, I. Culbert, E. A. Boulter, and H. Dhirani, *Electrical Insulation for Rotating Machines: Design, Evaluation, Aging, Testing, and Repair.* John Wiley & Sons, Inc., 2003.

[19] R. Arora and W. Mosch, *High Voltage and Electrical Insulation Engineering.* Wiley-IEEE Press, 2011.

[20] T. Blythe and D. Bloor, *Electrical properties of polymers.* Cambridge University Press, 2005.

[21] J. K. Nelson, *Dielectric polymer nanocomposites.* Springer Science+Business Media, 2010.

[22] J. Verdu, *Oxidative ageing of polymers.* John Wiley & Sons, Inc., 2012.

[23] L. C. E. Struik, "Modeling power transformers to support the interpretation of frequency-response analysis," *Polymer Engineering and Science*, vol. 17, no. 3, pp. 165–173, March 1977.

[24] B. H. Chudnovsky, *Electrical Power Transmission and Distribution: Aging and Life Extension Techniques.* CRC Press, 2012.

[25] J. Densley, "Ageing mechanisms and diagnostics for power cables - an overview," *IEEE Electrical Insulation Magazine*, vol. 31, no. 1, pp. 14–22, Jan.-Feb. 2001.

[26] ASTM, "Standard test method for dielectric breakdown voltage and dielectric strength of solid electrical insulating materials at commercial power frequencies," *ASTM D149 - 09(2013)*, 2013.

[27] ASTM, "Standard test method for dielectric breakdown voltage and dielectric strength of solid electrical insulating materials using impulse waves," *ASTM D3426 - 97(2012)*, 2012.

[28] T. Brgger, "A new test method for assessing the impact of thermal cycling on hydrogenerator stator insulation," in *2010 Annual Report Conference on Electrical Insulation and Dielectic Phenomena*, Oct. 2010.

[29] E. Steennis and F. Kreuger, "Water treeing in polyethylene cables," *IEEE Transactions on Electrical Insulation*, vol. 25, no. 5, pp. 989–1028, Oct. 1990.

[30] G. Mazzanti, G. Montanari, and F. Palmieri, "Quantities extracted from space-charge measurements as markers for insulation aging," *IEEE Transactions on Dielectrics and Electrical Insulation*, vol. 10, no. 2, pp. 198–203, April 2003.

[31] W. Song, W. Shen, G. Zhang, B. Song, Y. Lang, G. Su, H. Mu, and J. Deng, "Aging characterization of high temperature vulcanized silicone rubber housing material used for outdoor insulation," *IEEE Transactions on Dielectrics and Electrical Insulation*, vol. 22, no. 5, pp. 961–969, Apr. 2015.

[32] S. O. Kasap, *Principles of Electronic Materials and Devices*. McGraw-Hill, 2006.

[33] E.Kuffel, W. S. Zaengl, and J.Kuffel, *High voltage engineering fundamentals*. Newnes, 2000.

[34] A. K. Jonscher, *Dielectric relaxation in solids*. Chelsea Dielectrics Press, 1983.

[35] R. Coelho, *Physics of dielectrics for the Engineer*. Elsevier scientific publishing company, 1979.

[36] A. K. Jonscher, "Dielectric relaxation in solids," *Journal of Physics D: Applied Physics*, vol. 32, no. 14, pp. 57–69, Feb. 1999.

[37] L. A. Dissado and R. M. Hill, "Anomalous low-frequency dispersion. near direct current conductivity in disordered low-dimensional materials," *Journal of the Chemical Society, Faraday Transactions 2: Molecular and Chemical Physics*, vol. 80, no. 3, pp. 57–69, 1999.

[38] R. Keam and W. Holmes, "Uncertainty analysis of measurement of complex dielectric permittivity using microstrip transmission line," in *Proceedings of 1995 SBMO/IEEE MTT-S International Microwave and Optoelectronics Conference*, July 1995, pp. 137–142.

[39] A. Nikolson and G. Ross, "Measurement of the intrinsic properties of materials by time-domain techniques," *IEEE Transactions on Instrumentation and Measurement*, vol. 19, no. 4, pp. 377–382, Nov. 1970.

[40] E. Tanabe and W. Joines, "A nondestructive method for measuring the complex permittivity of dielectric materials at microwave frequencies using an open transmission line resonator," *IEEE Transactions on Instrumentation and Measurement*, vol. 25, no. 3, pp. 222–226, Nov. 1976.

[41] R. A. Waldron, "Perturbation theory of resonant cavities," *Proceedings of the IEE - Part C: Monographs*, vol. 107, no. 12, pp. 272–274, Sep. 1960.

[42] E. Hoch, "Electrode effects in the measurement of power factor dielectric constant of sheet insulating materials," *The Bell System Technical Journal*, vol. 5, no. 4, pp. 555–572, June 1926.

[43] J. C. Fothergill, S. J. Dodd, L. A. Dissado, T. Liu, and U. H. Nilsson, "The measurement of very low conductivity and dielectric loss in xlpe cables: a possible method to detect degradation due to thermal aging," *IEEE Transactions on Dielectrics and Electrical Insulation*, vol. 18, no. 5, pp. 1544–1553, Oct. 2011.

[44] J. C.Anderson, *Dielectrics*. Chapman and Hall LTD, 1964.

[45] F. Kremer and A. Schnhals, *Broadband Dielectric Spectroscopy*. Springer-Verlag Berlin Heidelberg, 2012.

[46] A. Campbell, "On the electric inductive capacities of dry paper and of solid cellulose," *Proceedings of the Royal Society of London*, vol. 78, pp. 196–211, June 1906.

[47] S. Analytical, *Solartron Analytical Modulab XM Materials Test System. User guide.*

[48] A. Scott and H. Curtis, "Edge correction in the determination of dielectric constant," *Journal of Research of the National Bureau of Standards*, vol. 22, no. 6, pp. 747–775, 1939.

[49] D. E. Wooley, "Edge correction in calculation of dielectric constant," *Journal of testing and evaluation*, vol. 39, no. 2, pp. 140–149, August 2011.

[50] K. K. Sadasivuni, K. Kumar, D. Ponnamma, J. Cabibihan, and A. AlMaadeed, *Flexible and stretchable electronic composites. Electronic applications of polydimethylsiloxane and its composites*. Springer International Publishing Switzerland, 2016.

[51] A. P. T. AB, *Silicone rubber. Product information.* ABB Power Technologies AB, 2005.

[52] L. H. Meyer, E. A. Cherney, and S. H. Jayaram, "The role of inorganic fillers in silicone rubber for outdoor insulation alumina tri-hydrate or silica," *IEEE Electrical Insulation Magazine*, vol. 20, no. 4, pp. 13–21, August 2004.

[53] W. A. Thue, *Electrical Power Cable Engineering.* CRC Press, 2012.

[54] A. E. Vlastos and S. M. Gubanski, "Surface structural changes of naturally aged silicone and epdm composite insulators," *IEEE Transactions on Power Delivery*, vol. 6, no. 2, pp. 888–900, Apr. 1991.

[55] Y. Kurata, K. Takano, K. Sakuraba, and M. Hayashi, "Evaluation of epdm rubber for high voltage insulator," in *Proceedings of 1995 Conference on Electrical Insulation and Dielectric Phenomena*, Oct. 1995, pp. 471–474.

[56] A. A. Athawale and A. M. Joshi, *Flexible and stretchable electronic composites. Electronic applications of ethylene propylene diene monomer rubber and its composites.* Springer International Publishing Switzerland, 2016.

[57] C. Zhang and G. C. Stevens, "The dielectric response of polar and non-polar nanodielectrics," *IEEE Transactions on Dielectrics and Electrical Insulation*, vol. 15, no. 2, pp. 606–617, Apr. 2008.

[58] CIGRÉ, "Interfacial phenomena affecting electrical insulating properties in composites, working group 15.10," *Electra*, no. 202, 2002.

[59] K. R. Bambery, R. J. Fleming, and J. T. Holboll, "Space charge profiles in low density polyethylene samples containing a permittivity/conductivity gradient," *Journal of Physics D: Applied Physics*, vol. 34, no. 20, pp. 3071–3077, Oct. 2001.

[60] J. Zhang, J. A. Gifford, G. J. Zhao, D. R. Kim, C. N. Snider, N. Vargas, and T. Y. Chen, "Control of thermal gradient using thermoelectric coolers for study of thermal effects," *Journal of Applied Physics*, vol. 117, no. 17, p. 17C508, March 2015.

[61] C. J. Metting, J. K. Bunn, J. Fadimba, E. Underwood, Y. Zhu, G. Koley, T. Crawford, and J. Hattrick-Simpers, "Note: A simple thermal gradient annealing unit for the treatment of thin films," *Review of Scientific Instruments*, vol. 84, no. 3, p. 036111, March 2013.

[62] M. Ehsani, H. Borsi, E. Gockenbach, J. Morshedian, G. Bakhshandeh, and A. Shayegani, "Effect of aging on dielectric behavior of outdoor polymeric insulators," in *Proceedings of the 2004 IEEE International Conference on Solid Dielectrics*, vol. 1, July 2004, pp. 312–315.

[63] A. V. Vykhodtsev, B. Kordi, and D. R. Oliver, "Sensitivity analysis of a parallel-plate method for measuring the dielectric permittivity of high-voltage insulating materials," *High Voltage IET*, vol. 2, no. 3, pp. 200–204, Sep. 2017.

[64] B. R. Bean and E. F. Dutton, *Radio Meteorology.* National Bureau of Standards, 1966.

[65] X. Xu and S. M. Gubanski, "Contact-free dielectric response measurement CIGRÉ WG D1.59," March 2017.

[66] R. Kochetov, I. A. Tsekmes, P. H. F. Morshuis, J. J. Smit, A. J. Wanner, F. Wiesbrock, and W. Kern, "Effect of water absorption on dielectric spectrum of nanocomposites," in *Proceedings of 2016 IEEE Electrical Insulation Conference*, June 2016, pp. 579–582.

[67] T. Tokoro, Y. Katayama, and M. K. . R. Hackam, "Aging and recovery of htv silicone and epdm rubbers due to continuous wetting," in *Proceedings of 2001 International Symposium on Electrical Insulating Materials (ISEIM 2001)*, Nov. 2001, pp. 51–54.

[68] D. Bouguedad, A. Mekhaldi, A. Boubakeour, and O. Jbara, "Thermal ageing effects on the properties of ethylene-propvlene-diene monomer (epdm)," *IEEE Transactions on Dielectrics and Electrical Insulation*, vol. 33, no. 4, pp. 303–313, 2008.

[69] C. Schrijver, A. Herden, and H. C. Krner, "A chemical approach to the dielectric aging of fibre-reinforced polymer (frp) insulators," *International Transactions on Electrical Energy Systems*, vol. 7, no. 2, pp. 99–105, April 1997.

[70] B. M. J. Smets, "On the mechanism of the corrosion of glass by water," *Philips technical review*, vol. 42, no. 2, pp. 59–64, Aug. 1985.

[71] K. Y. Lau, A. S. Vaughan, G. Chen, L. Hosier, and A. F. Holt, "On the dielectric response of silica-based polyethylene nanocomposites," *Journal of Physics D: Applied Physics*, vol. 46, no. 9, p. 095303, Feb. 2013.

[72] D. Bouguedad, O. Jbara, S. Rondot, A. Mekhaldi, and A. Hadjadj, "Investigation of accelerated thermal aging of epdm polymer by electric tests in air and by means of a sem technique in high vacuum," *IEEE Transactions on Dielectrics and Electrical Insulation*, vol. 19, no. 3, pp. 981–989, June 2012.

[73] S. Kornhuber, "Contact-free dielectric response measurement CIGRÉ WG D1.59," November 2017.

Appendix A

Comments on the Solartron Dielectric Spectrometer

Appendix A contains the observations obtained during the measurements using the Solartron Dielectric Spectrometer. At one stage of our studies we faced a measuring problem: the jump-wise behavior of the measured capacitance. It correlated with the moment of switching to more sensitive current range (Figure A.1).

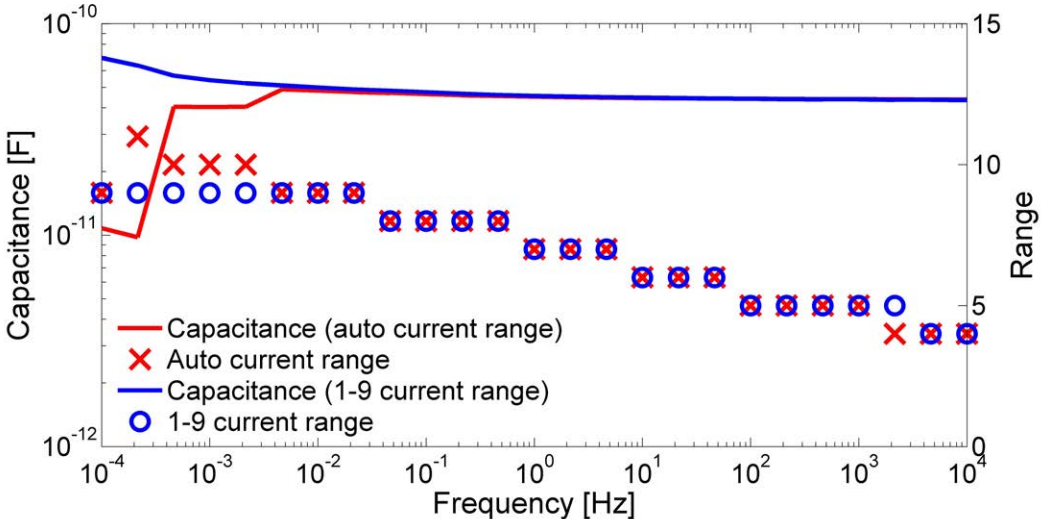

Figure A.1. *The combined capacitance of the CIGRÉ holder and a polymeric sample measured with the auto current range and with the limited current range.*

After a rigorous analysis, two possible sources were detected: one associated with an abnormal noise in the half-period of the sinusoid in the measured current (Figure A.2 a)

and a second linked with the oscillations after the switching to more sensitive current range (Figure A.2 b). An abnormal noise was inherent to both sample holders and, therefore, was considered as an internal malfunction of the Solartron dielectric spectrometer. Whilst oscillations after the switching to more sensitive current range mostly appeared when the *CIGRÉ* holder was used. We believe that the reason for these oscillation is the reaction of femto electrometer amplifier to "high" currents and stronger interference generated by the CIGRE holder in combination with a sample. The temporary solution was to limit the diapason of current change from 1 (100 mA -range) to 9 (3 nA-range with maximum resolution of 0.15 pA). Such action improved the stability of the measurements (Figure **??**) but it rose the concern regarding the data in the frequency range from 10^{-4} Hz to 10^{-3} Hz when a less accurate current range was employed.

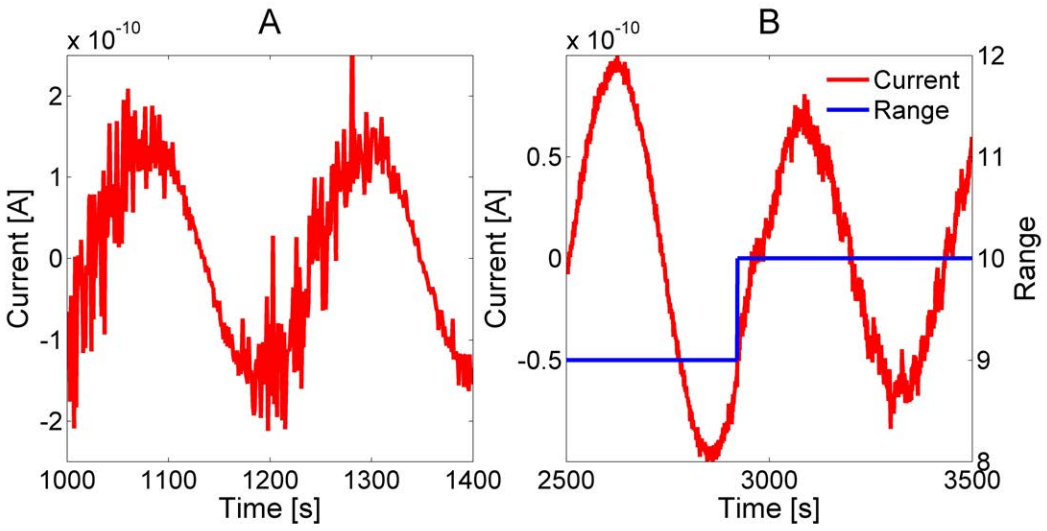

Figure A.2. *The current response of the CIGRÉ holder and a polymeric sample demonstrating two artefacts that impacts the measurements:(a) - an abnormal noise in the half-period of the sinusoid;(b)- oscillations after the switching to more sensitive current range.*

The problem associated with an abnormal noise in the half-period of the sinusoid was solved by installing a new firmware that was developed by the Solartron production team after our request. The upgraded system was tested using 10 nF capacitor from the installation kit of Solartron Materials Test System. The results of 10 nF capacitor measurements before and after the upgrade of the firmware are compared in Figure A.3).

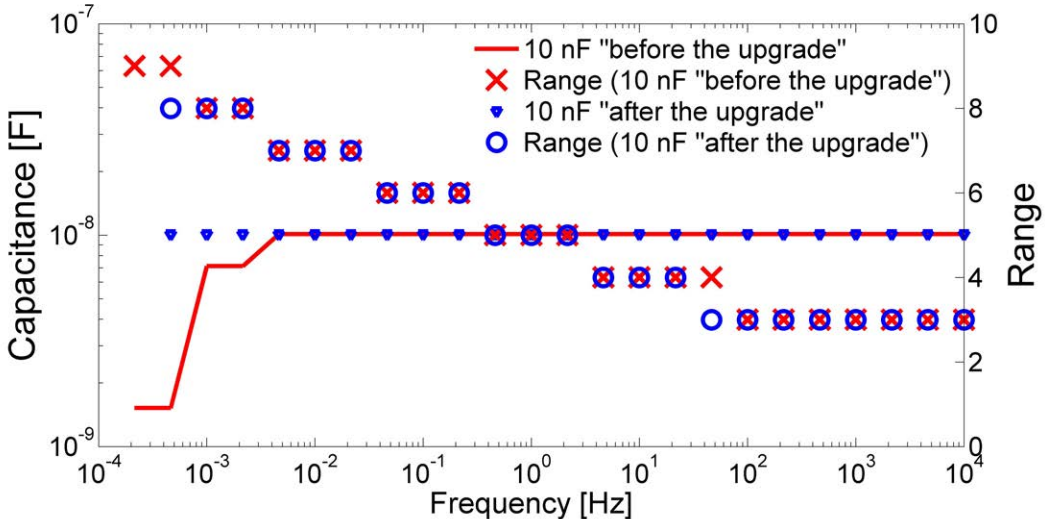

Figure A.3. *Measurements with 10 nF capacitor from the installation kit of the Solartron Materials Test System before and after the upgrade of the firmware.*

Appendix B

Sample/Electrode Arrangements

Appendix B contains figures displaying the dielectric response of the LSR and HTV samples measured by means of the close-contact and contact-free parallel plate techniques using the Solartron holder.

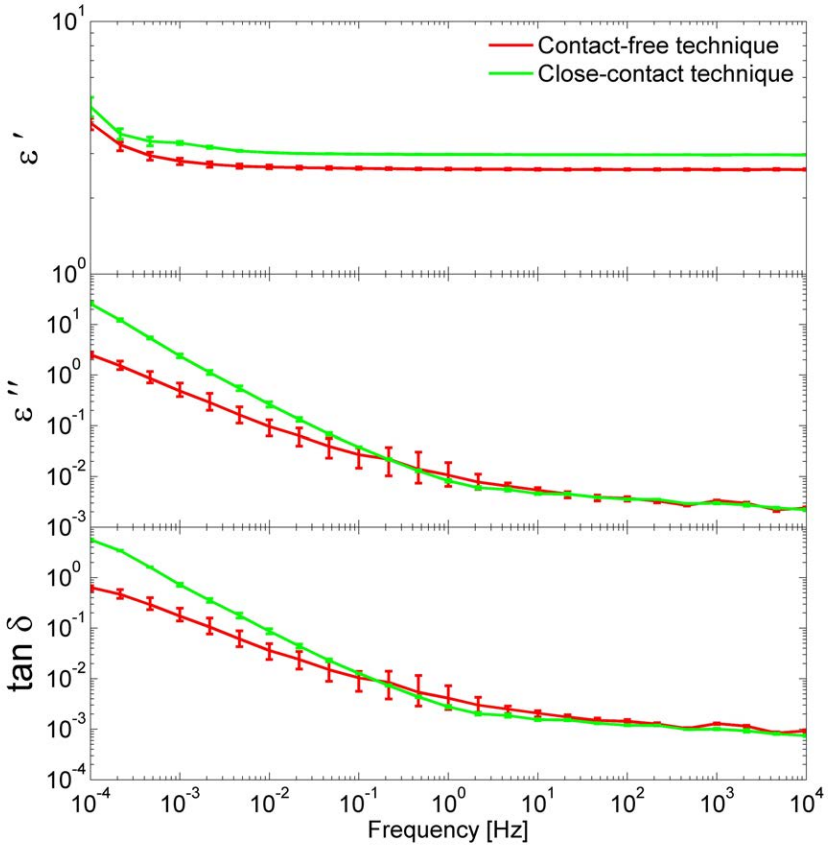

Figure B.1. *The Log-log plot of the real and imaginary parts of the complex dielectric permittivity and the loss tangent of LSR measured by means of the close-contact and contact-free parallel plate techniques employing the Solartron holder.*

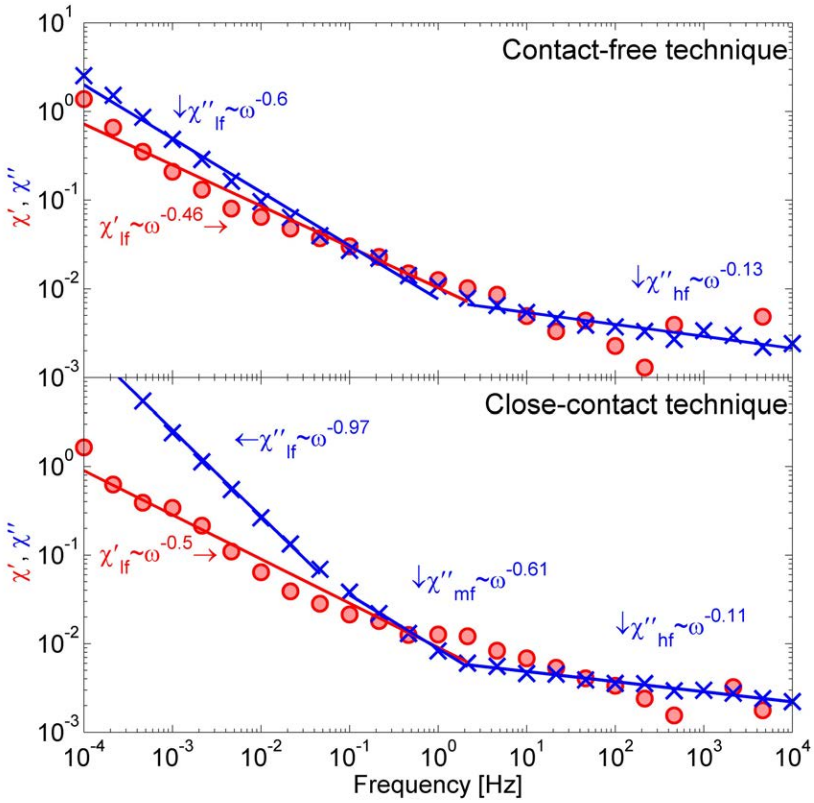

Figure B.2. *The electric susceptibility of LSR rubber measured by means of the close-contact and contact-free parallel plate technique employing the Solartron holder (the red colour corresponds to the real part of the electric susceptibility and the blue colour corresponds to the imaginary part of the electric susceptibility).*

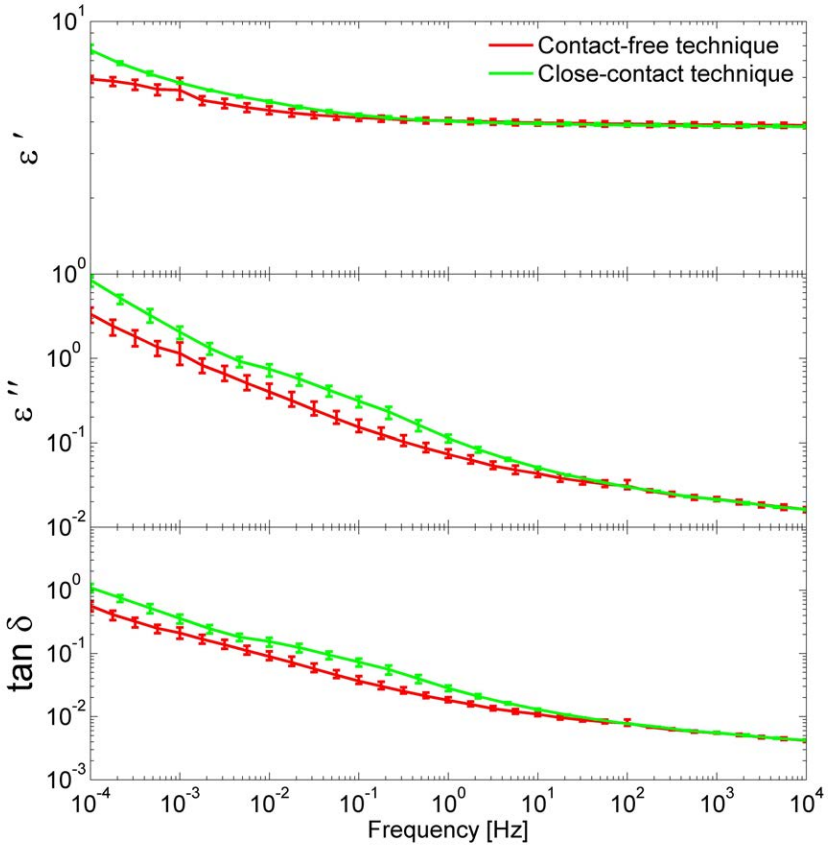

Figure B.3. *The log-log plot of real and imaginary parts of the complex dielectric permittivity and the loss tangent of HTV measured by means of the close-contact and contact-free parallel plate techniques employing the Solartron holder.*

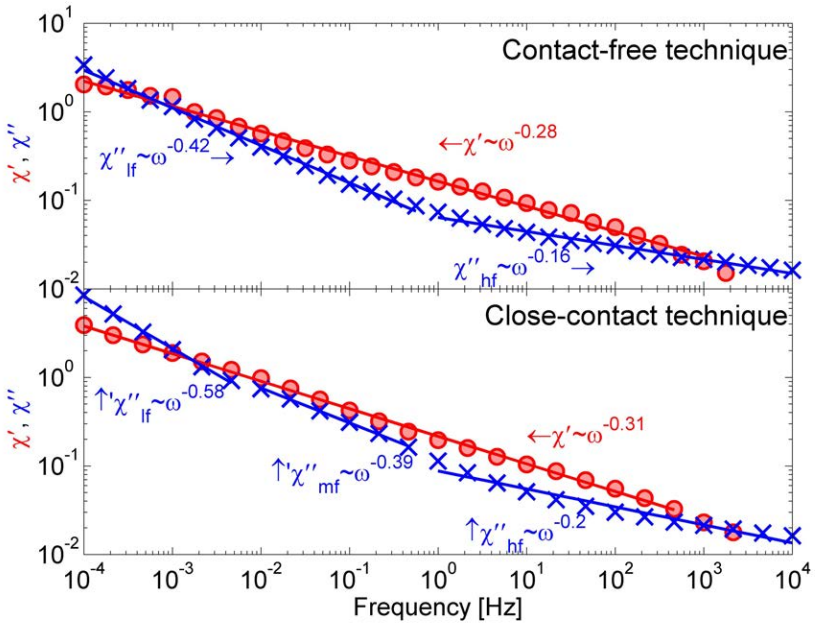

Figure B.4. *The electric susceptibility of HTV measured by means of the close-contact and contact-free parallel plate technique employing the Solartron holder (the red colour corresponds to the real part of the electric susceptibility and the blue colour corresponds to the imaginary part of the electric susceptibility).*

Appendix C

Weight Measurements

Appendix C contains the mass measurements of the polymeric samples during the water immersion ageing procedure (Table C.1) and the heat treatment (Table C.2).

Table C.1. *The evolution of the sample weight during the water immersion ageing procedure (Table 5.3) in [g].*

Material	S1	S2	S3	S4
EPDM	52.537	52.335	52.507	51.302
LSR	34.925	34.876	34.836	34.808
HTV	59.658	59.621	59.763	59.368
W12	168.715	-	169.174	168.618
W12 EST	170.434	-	171	170.274
FRP	121.027	-	121.239	121.139

Table C.2. *The evolution of the sample weight during the heat treatment procedure (Table 5.4) in [g].*

Material	D1	D2	D3
EPDM	51.864	51.66	50.556
LSR	34.994	34.873	34.758
HTV	60.24	60.227	60.28

Appendix D

Water Immersion Ageing

Appendix D contains figures displaying the electric susceptibility of LSR, HTV, W12 W12 EST, and FRP measured by means of the contact-free parallel plate technique using the *CIGRÉ* holder during the water immersion ageing.

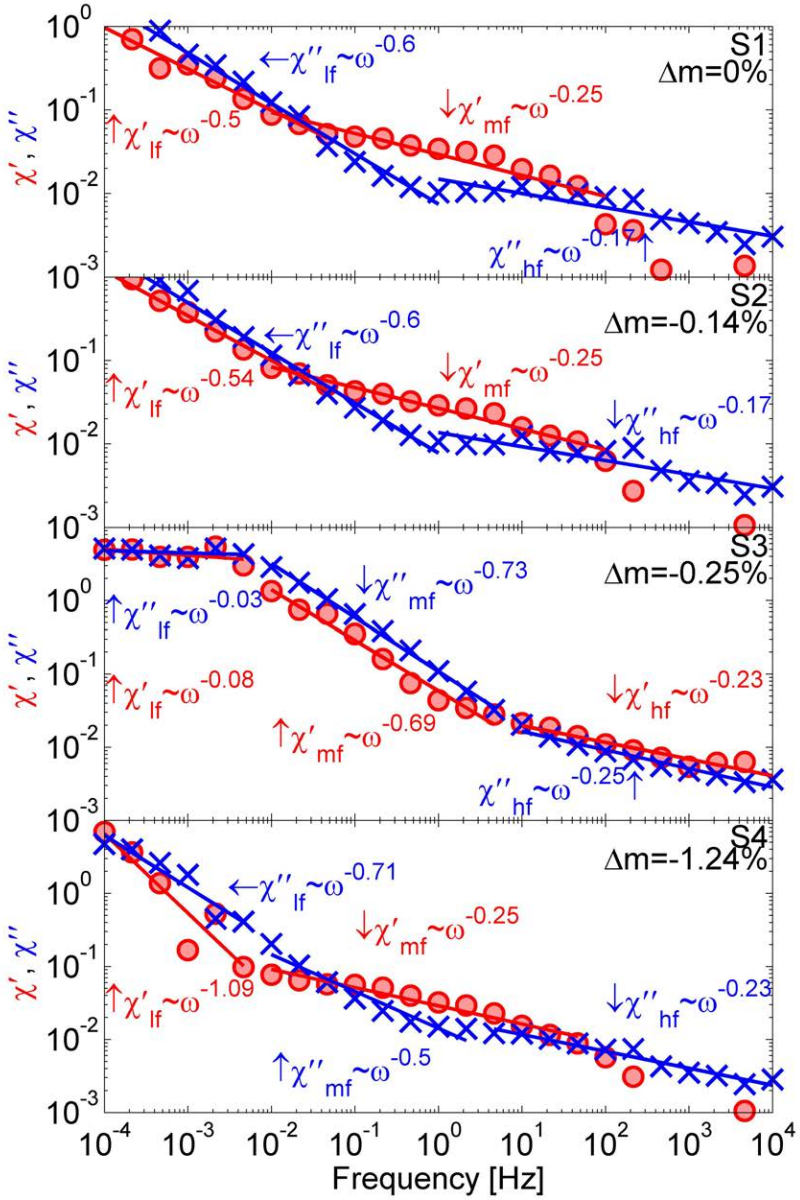

Figure D.1. *The log-log plot of the electric susceptibility (red - χ' and blue - χ'') of LSR measured by means of the contact-free parallel plate technique employing the CIGRÉ holder during the water immersion ageing (Table 5.3). The mass change associated with the step of the protocol is provided.*

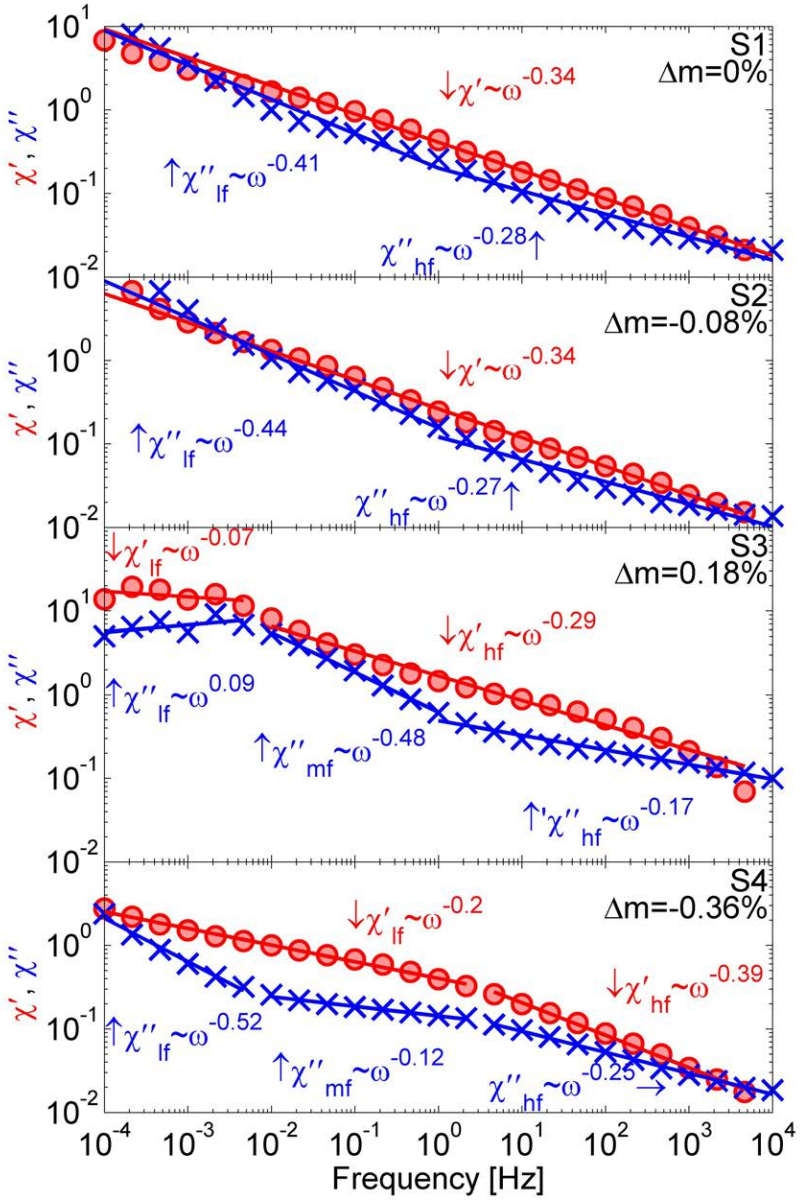

Figure D.2. *The log-log plot of the electric susceptibility (red - χ' and blue - χ'') of HTV measured by means of the contact-free parallel plate technique employing the CIGRÉ holder during the water immersion ageing (Table 5.3). The mass change associated with the step of the protocol is provided.*

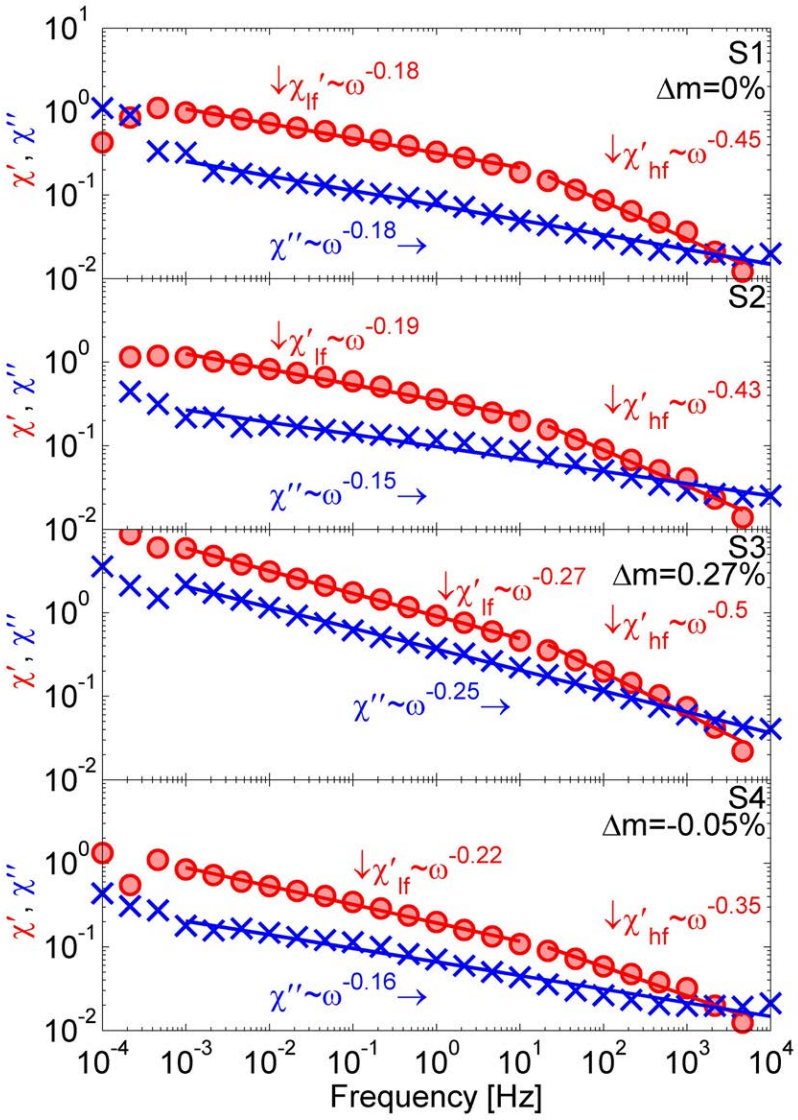

Figure D.3. *The log-log plot of the electric susceptibility (red - χ' and blue - χ'') of W12 measured by means of the contact-free parallel plate technique employing the CIGRÉ holder during the water immersion ageing (Table 5.3). The mass change associated with the step of the protocol is provided.*

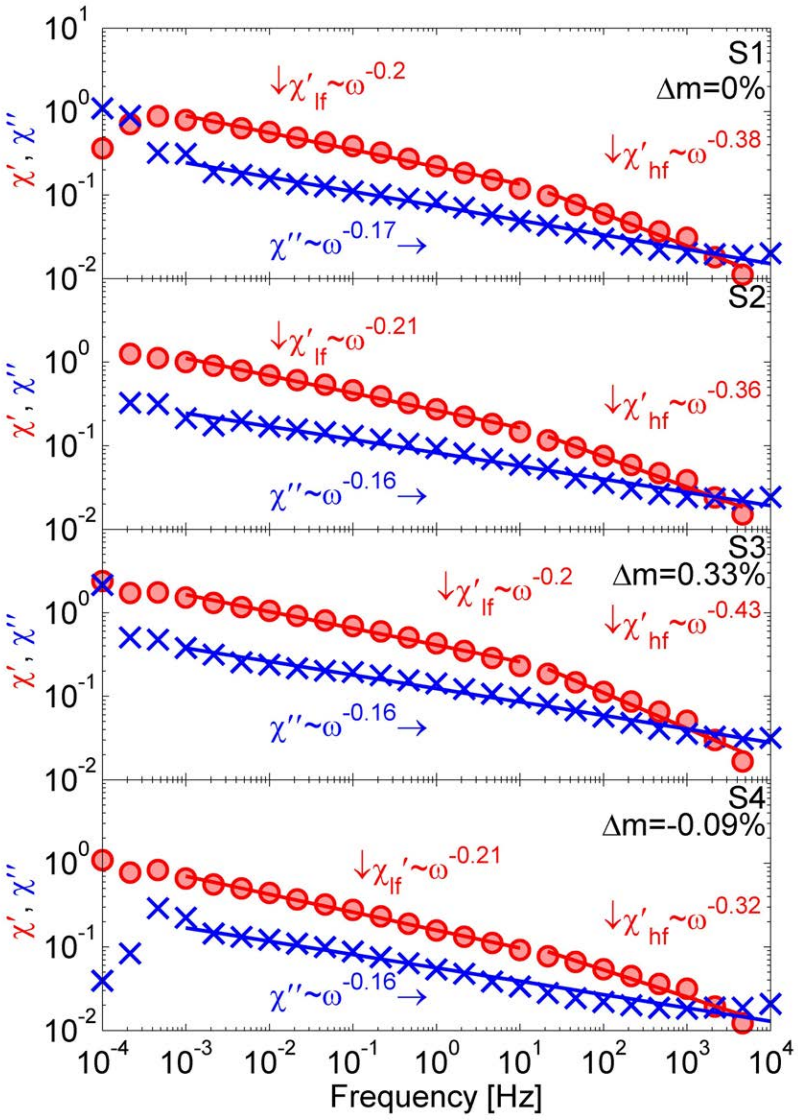

Figure D.4. *The log-log plot of the electric susceptibility (red - χ' and blue - χ'') of W12 EST measured by means of the contact-free parallel plate technique employing the CIGRÉ holder during the water immersion ageing (Table 5.3). The mass change associated with the step of the protocol is provided.*

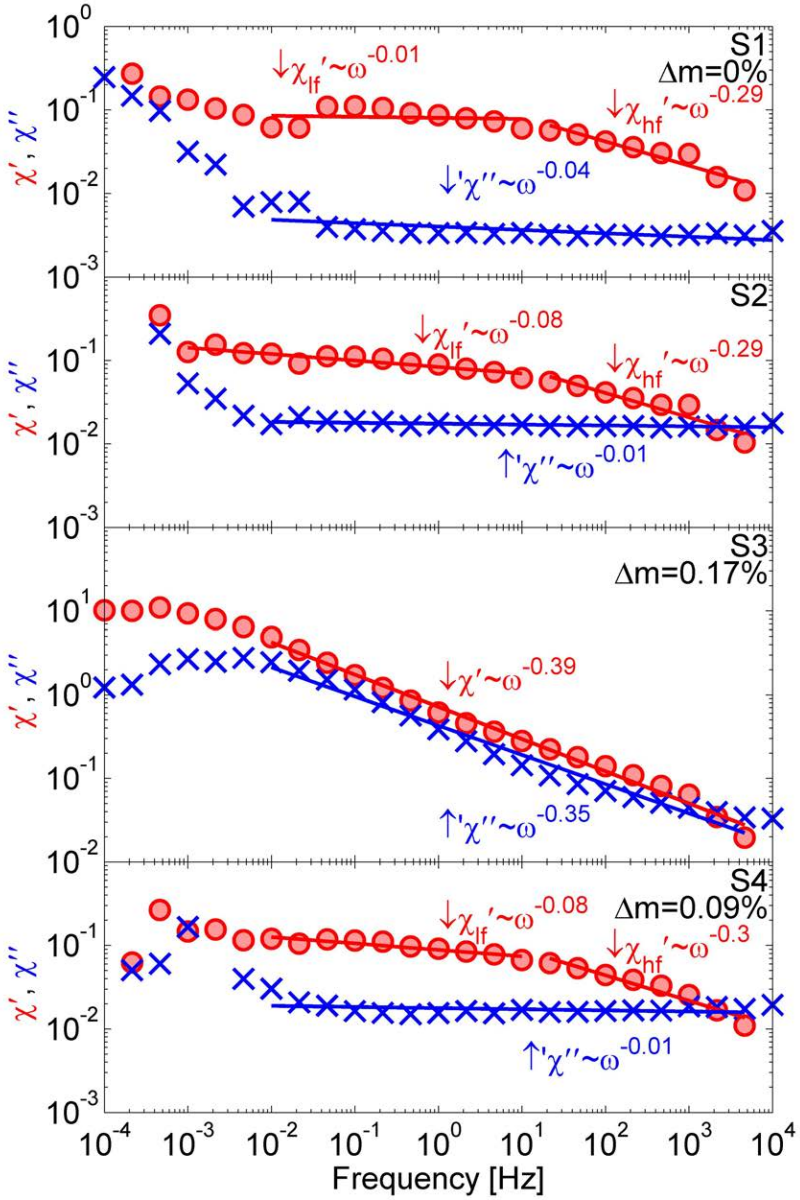

Figure D.5. *The log-log plot of the electric susceptibility (red - χ' and blue - χ'') of FRP measured by means of the contact-free parallel plate technique employing the CIGRÉ holder during the water immersion ageing (Table 5.3). The mass change associated with the step of the protocol is provided.*